



VCU

Virginia Commonwealth University
VCU Scholars Compass

Theses and Dissertations


Graduate School

2019

Adhesion at Solid/Liquid Interfaces

Neda Ojaghlou
Virginia Commonwealth University

Follow this and additional works at: <https://scholarscompass.vcu.edu/etd>

 Part of the [Computational Engineering Commons](#), [Fluid Dynamics Commons](#), [Physical Chemistry Commons](#), and the [Statistical, Nonlinear, and Soft Matter Physics Commons](#)

© The Author

Downloaded from

<https://scholarscompass.vcu.edu/etd/6079>

This Dissertation is brought to you for free and open access by the Graduate School at VCU Scholars Compass. It has been accepted for inclusion in Theses and Dissertations by an authorized administrator of VCU Scholars Compass. For more information, please contact libcompass@vcu.edu.

Adhesion at Solid/Liquid Interfaces

A dissertation submitted in partial fulfillment of the requirements for the degree of

Doctor of Philosophy at Virginia Commonwealth University

by

Neda Ojaghlo

M.S. Physics, University of Zanjan

Directors: Drs. Dusan Bratko, Alenka Luzar

Professors, Department of Chemistry

Virginia Commonwealth University

Richmond, Virginia

December 2019

Copyright © 2019 Neda Ojaghlou

All Rights Reserved

Dedication

I am dedicating this thesis to three beloved people who have meant and continue to mean so much to me.

I dedicate this work to my mother and father, Razieh and Amir Mahdi, whose love for me knew no bounds and, who taught me the value of hard work.

I would like to express my gratitude and dedicate this work to my husband, Mahdi, whose love made it possible for me to finish this thesis successfully.

I could not have come this far without their unconditional support.

Acknowledgement

I wish to express my sincere thanks to Prof. Alenka Luzar, my advisor, for her continuous support, valuable guidance and encouragement throughout the course of my research. Although she is no longer of this world, her memories continue to influence my life.

I would like to extend my feeling of gratitude to Professor Dusan Bratko, my advisor, for the patient guidance, encouragement, and advice he has provided throughout my time in the lab. I would not have been able to finish this work without his support and unfailing faith in me.

I wish to thank the members of my dissertation committee professors Hooman Tafreshi, Reza Mohammadi, Hani El-Kaderi, and Ka Un Lao. They kindly gave their time to provide me valued remarks toward improving my work.

I sincerely thank professors Hooman Tafreshi and Mathieu Salanne for lending me their skills and intuition to my scientific presentation. These brilliant friends and colleagues inspired me over the many years: Serban Zamfir, Jyoti Roy Choudhuri, and Shadrak Jabes. Also, Virginia Commonwealth University, and National science Foundation are appreciated for their support during my graduate school years.

I will always be grateful to my family for their love, patience, guidance, and inspiration. Without every single one of you, it would not have happened that I wrote a dissertation today. Some special words of gratitude go to my friends in Richmond who have been like my family and inspired me over the many years.

Table of Contents

Adhesion at Solid/Liquid Interfaces.....	i
Table of Contents	1
List of Figures.....	4
List of Tables	11
Abstract.....	12
Chapter 1: Introduction	14
1.1 Basic surface thermodynamics	15
1.2 Droplet detachment from a fiber.....	21
1.3 Adhesion on conducting surface.....	23
1.3.1 Water adhesion on conducting graphene	24
Chapter 2: Water adhesion on hydrophilic surfaces.....	29
2.1 Droplet detachment from a fiber.....	29
2.2 Methodology	30
2.2.1 Force fields.....	30
2.2.2 Simulation details.....	33
2.3 Results and discussions.....	38

2.3.1 Droplet equilibrium shape on a fiber	38
2.3.2 Droplet behavior in the presence of an external force	40
2.3.3 Effect of droplet volume on the minimum detachment force	44
2.3.4 Minimum detachment force for different fiber radii.....	45
2.3.5 Effect of adhesion strength on the minimum detachment force	46
2.4 Residual of the droplet on a fiber.....	48
2.5 Conclusion	62
2.6 Pathway of droplet removal from a hydrophilic surface	64
2.6.1 Methodology	66
2.6.2 Simulation details.....	66
2.6.3 Results and discussion	68
2.6.4 Conclusion	79
Chapter 3: Water adhesion on conducting graphene.....	80
3.1.1 Models and methods	81
3.2 Results and discussions.....	85
3.2.1 Graphene/water density profiles	89
3.2.2 Contact angles.....	92
3.2.3 Dipolar correlations across graphene.....	94
3.2.4 Non-polar liquid.....	102

3.3 Conclusion	104
Chapter 4: Summary and outlook.....	106
References.....	108
Appendices.....	120
Appendix 1.....	120
Appendix 2.	121
Appendix 3.	122
Appendix 4.....	123
Vita	124

List of Figures

Figure 1: Image of water droplets supported on (a) hydrophilic, and (b) hydrophobic surfaces.	15
Figure 2: Schematic of a liquid drop showing the quantities in the Young equation.	16
Figure 3: The three different possible wetting states according to Young's equation.	18
Figure 4: Schematic and macroscopic drops from experiment representing barrel and clamshell shapes of a water droplet on a fiber.	22
Figure 5: Experimental measurement of the water contact angle on a single graphene sheet almost completely suspended on air or supported by water, by varying the fraction of solid area of the support.	26
Figure 6: MD simulation of water contact angle on a single graphene sheet almost completely suspended on and supported by water.	27
Figure 7: SPC/E water model	31
Figure 8: Equilibrium barrel shape of a 2000 molecules atomistic droplet on a fiber with $r_f = 6.4 \text{ \AA}$	31
Figure 9: Equilibrium barrel shape of atomistic droplet on a fiber with $r_f = 12.8 \text{ \AA}$	33
Figure 10: Snapshots from a MD trajectory during the droplet detachment from a fiber for the atomistic model with $V_r = 500$ and fiber radius $r_f = 6.4 \text{ \AA}$. (1-a): d gradually until the drop is about to detach from the fiber. (1-b): snapshots showing the evolution of droplet	

shape at constant force, $F = 0.0058 \text{ kJ mol}^{-1} \text{ \AA}^{-1}$, exerted on the droplet during the simulation..... 36

Figure 11: Snapshots from a MD trajectory during the droplet detachment from a fiber for the coarse-grained model with $V_r = 500$ and fiber radius $r_f = 12.8 \text{ \AA}$ 37

Figure 12: Morphology diagram of atomistic droplets deposited on a smooth fiber with fiber radius, $r_f = 6.4 \text{ \AA}$, at varied reduced volumes and water-fiber interactions. Green triangles denote the states where simulated droplets were consistently of stable barrel shape. Red squares show when the clamshell shape was stable. The number of water molecules corresponding to the given range of V varies from 2000-17000. The threshold value of carbon-water interaction strength $\epsilon_{co} = 0.6 \text{ kJ mol}^{-1}$ corresponds to water-substrate contact angle 33° , which can result in bistability in macroscopic systems. 39

Figure 13: Snapshots from MD trajectories of the droplet detachment from fiber for the atomistic model and $V_r = 750$ (6×10^3 water molecules). Figures a-c illustrate the droplet evolution at different external forces, $F = 0.0041, 0.0058, \text{ or } 0.41 \text{ kJ mol}^{-1} \text{ \AA}^{-1}$ applied to the droplet in the direction perpendicular to the fiber. The atomistic droplet consists of 6000 SPC/E water molecules on the fiber with a radius $r_f = 6.4 \text{ \AA}$. Figure d presents snapshots from an MD trajectory of the droplet detachment from a fiber for a coarse-grained model at $V_r = 750$. The force exerted on the droplet was $F = 0.0016 \text{ kJ mol}^{-1} \text{ \AA}^{-1}$. The droplet consists of 52428 mW water molecules and the fiber radius is 12.8 \AA . Figure e, side view (bottom) and front view (top) snapshots from MD trajectories of the droplet detachment from fiber for the atomistic model with $V_r = 750$ and $F = 0.016 \text{ kJ mol}^{-1} \text{ \AA}^{-1}$ a the force strength that maximizes the average residue on the fiber at given V_r 42

Figure 14: Snapshots from MD trajectories of the droplet detachment from a fiber for the atomistic model. Figures a-b show that the breakup happens at different distances from the fiber and different times for two different atomistic simulations with $V_r = 500$. The droplet consists of 4000 SPC/E water molecules and the fiber radius is 6.4 Å. The force is $F=0.0125 \text{ kJ mol}^{-1} \text{ \AA}^{-1}$. Figures c-e show the formation of a satellite droplet following the detachment of the drop from the fiber under the force $F=0.0292 \text{ kJ mol}^{-1} \text{ \AA}^{-1}$ for the atomistic water model and $V_r = 2000$. The droplet contains 17000 SPC/E water molecules and the fiber radius $r_f = 6.4 \text{ \AA}$ 43

Figure 15: The minimum force required to detach the droplet from a fiber at different reduced volumes. Top: the black curve describes simulation results of the atomistic model with the fiber radius 6.4 Å. The red curve was produced by scaling the result for $V_r = 250$ in proportion to $V_r^{-2/3}$. Middle, black circles: atomistic simulations with the fiber radius $r_f = 6.4 \text{ \AA}$; orange triangles: CG system and fiber radius 12.8 Å, rescaled to $r_f = 6.4 \text{ \AA}$; blue diamonds and green squares: data from the Finite Element simulations with two different fiber radii 5 μm and 107.5 μm¹⁶ rescaled to $r_f = 6.4 \text{ \AA}$. The latter two curves correspond to a bigger contact angle of water on the fiber $\theta \sim 50^\circ$.¹⁶ Bottom: results for fiber-water interaction strengths $\varepsilon_{co} = 0.62 \text{ kJmol}^{-1}$ and $\varepsilon_{co} = 0.56 \text{ kJmol}^{-1}$. Contact angles of atomistic water on flat surface with the same interactions are $\approx 30^\circ$ and 50° , respectively. The pink “x” and crayon triangles represent the force required to detach a droplet from a fiber with radius 6.4 Å, for an atomistic model system with different water-fiber interactions. The remaining three sets of data (violet, green, and blue) correspond to macroscopic systems with $r_f = 107.5 \text{ \AA} \mu\text{m}$, rescaled to $r_f = 6.4 \text{ \AA}$. The violet stars describe experimental points¹⁶ and the blue square and green diamonds are from Finite Element simulations with contact angles 30° , 50° , respectively.¹⁶ Error bars are of the same size as the symbols. 47

Figure 16: Morphology diagram of nano-sized droplets on a fiber with radius , $r_f = 6.4 \text{ \AA}$ and $\varepsilon_{co} = 0.6639 \text{ kJ mol}^{-1}$, as a function of applied force F and reduced volume of the drop, V_r . The red color indicates the minimum force of detachment and green color indicates the threshold force above which no residue of the droplet remains on the fiber. The number of water molecules varies from 2000 to 17000. The inset shows the probability P_{residue} of observing a residue on the fiber vs reduced volumes when applying the minimum detachment force..... 50

Figure 17: Time correlation function, R(t), of the height of the center of mass of droplet on fiber for an atomistic system with reduced volume $V_r = 2000$ and fiber radius, $r_f = 6.4 \text{ \AA}$. At time close to 1ns, R(t) crosses to the negative value due to inertia. The inset figure shows the detachment time of the droplet as a function of applied force..... 52

Figure 18: Symbols: MD detachment times of water droplets from the fiber of radius 6.4 \AA as functions of the relative excess of applied forces of strengths well above the minimal detachment force F_{min} (Figure 15a) for the atomistic model of water. Scaling of the form $t_d \propto (F / F_{\text{min}} - 1)^{(2/3)}$ is indicated for all droplet volumes above the smallest size ($V_r \sim 250$) where only approximate compliance is observed. Lines are fitted to the MD data using the fixed slope -2/3. 53

Figure 19: Percentage of the residue of a droplet remaining on the fiber, $r_f = 6.4 \text{ \AA}$ or 12.8 \AA , obtained by applying a minimum detachment force..... 54

Figure 20: (a) Percentage of the residue of a droplet remaining on the fiber, $r_f = 6.4 \text{ \AA}$, obtained by applying a range of forces. The curves start at the minimum force of detachment. Error bars are estimated from multiple simulations for respective forces with each system statistically independent from others. (b) Percentage of the residue of the droplet on the fiber versus the detachment time. 56

Figure 21: The average number of water molecules remaining on the fiber versus the total number of water molecules at detachment forces producing the maximal residue. The symbols denote the maximum residue on the fiber with radius 6.4 Å at the time of detachment obtained from atomistic MD simulations. The dashed line indicates the fitting function $N_r \propto N_{tot}^{2/3}$ that is predicted by observing that the maximum residue corresponds to the double-cone pinch-off form of the detaching droplet. 58

Figure 22: Snapshots of MD trajectories of the droplet at the time of detachment from the fiber for the atomistic model with fiber radius, $r_f = 6.4 \text{ \AA}$, when the residue is maximized. The droplet sizes vary from 4000, 8000, 10000, 17000 SPC/E water molecules..... 59

Figure 23: The force producing the biggest average residue, F_{max} on the fiber as a function of the reduced volume. The dashed curve indicates the fitting function $V_r^{2/3}$. The droplet sizes in atomistic simulations vary from 2000 to 17 000 SPC/E water molecules..... 61

Figure 24: Snapshot of an equilibrium shape of aqueous droplet atop a model graphene surface. 67

Figure 25: Snapshots from MD trajectories of the droplet detachment from surface for the atomistic model at external forces $F = 0.062 \text{ or } 0.25 \text{ kJ mol}^{-1} \text{ \AA}^{-1}$ for a drop comprised of 4000 SPC/E water molecules on graphene surface..... 69

Figure 26: Minimum force required to detach the droplet from a surface for different droplet sizes. 70

Figure 27: Minimum force required to detach the droplet with 4000 water molecules from a surface for different water-carbon, ϵ_{co} , interactions..... 72

Figure 28: Minimum force required to detach the droplet with 4000 water molecules from a surface for different contact angles reveal a linear increase with the liquid/solid adhesion strength $\propto 1 + \cos\theta$ 73

Figure 29: Average residue of a droplet remaining on the surface, (the number of retained water molecules, (N_r), to the total number of molecules in the droplet, (N_{tot}), obtained by applying a range of forces. The lines start at the minimum force of detachment. 76

Figure 30: Detachment time of the droplet as a function of applied force. The red and blue lines are guide lines to the simulated data. 77

Figure 31: Contact area of droplet on the surface the moment before the detachment vs different forces 78

Figure 32: Snapshots of spreading of the semi-infinite hemi-cylindrical water droplet atop insulator without (a-b) or with a layer of water (c) placed below the sheet. The system containing a 6.4×10^3 molecule drop and 5.6×10^3 atom graphene sheet is periodically replicated in lateral directions. (d) A snapshot of a cylindrical water droplet atop graphene sheet in CPMD (See Methods section). 86

Figure 33: Density profiles of water in the central region of a cylindrical droplet base on the suspended or supported insulator and graphene sheets (modeled by CPMD) with $\epsilon_{co} = 0.3913 \text{ kJ mol}^{-1}$. Black curve: simulation result for the droplet density as function of the height z on the suspended insulator. Red: droplet on the insulator supported by an aqueous layer. Green: droplet on the suspended graphene. Blue: droplet on supported graphene. The densities are normalized by the density inside the bulk portion of the droplet. 90

Figure 34: Density profile of water on both side of the insulator surface for $\epsilon_{co} = 0.1951$ or $0.5208 \text{ kJ mol}^{-1}$. The plot shows each profile in relation to the z -dimension of the system box. The insulator sheet is placed at $z = 20\text{\AA}$ 91

Figure 35: Contact angle vs time for a cylindrical water droplet on the suspended insulator and graphene sheets (left), suspended or water-supported graphene sheets (right), and

supported insulator and supported graphene (bottom) for carbon-water interaction strengths $\varepsilon_{co} = 0.3913 \text{ kJ mol}^{-1}$ 93

Figure 36: Dipole angle probability distributions $P(\cos \varphi)$ for water molecules in the solid/water contact layer of the cylindrical nanodroplet on different surfaces $\varepsilon_{co} = 0.3013 \text{ kJ mol}^{-1}$, $\sigma_{co} = 3.19 \text{ \AA}$. Black line: suspended insulator. Red: water-supported insulator. Green color: suspended graphene, blue color: water-supported graphene. 96

Figure 37: Dipole-dipole correlation functions measuring orientational correlations between water molecules in the hydration layers of a cylindrical droplet atop the insulator sheet (left: a,c,e) or conducting graphene (right: b,d,f), and liquid water below the sheet for different values of ε_{co} 98

Figure 38: Favored configurations for a pair of water molecules interacting across the graphene sheet. Insulator sheet (left), conducting graphene (right), and liquid water below the sheet for different values of $\varepsilon_{co} = 0.3913 \text{ kJ mol}^{-1}$, $\sigma_{co} = 3.19 \text{ \AA}$ 99

Figure 39: Snapshots of spreading of the semi-infinite hemi-cylindrical CH_2I_2 droplet atop insulator with a layer of diiodomethane of thickness 13.1 \AA placed below the sheet. ... 103

List of Tables

Table 1: Contact angle θ of a cylindrical droplet on the suspended and supported graphene for different values of ε_{co} . θ_c refers to measurements to measurements without a water layer underneath the surface and θ_w correspond to a layer of water placed underneath graphene..... 89

Table 2: Average dipole moments and mean squared fluctuations of dipole components (x, y, or z) of water molecules in the first hydration layers of an insulating (a) and conducting (b) model graphene sheets wetted by an aqueous drop on the top side and supported by an aqueous slab on the bottom, all for three different carbon-water interaction strengths ε_{co} . (c) suspended insulating sheet. 101

Abstract

The adhesion at solid/liquid interface plays a fundamental role in diverse fields and helps explain the structure and physical properties of interfaces, at the atomic scale, for example in catalysis, crystal growth, lubrication, electrochemistry, colloidal system, and in many biological reactions. Unraveling the atomic structure at the solid/liquid interface is, therefore, one of the major challenges facing the surface science today to understand the physical processes in the phenomena such as surface coating, self-cleaning, and oil recovery applications. In this thesis, a variety of theory/computational methods in statistical physics and statistical mechanics are used to improve understanding of water adhesion at solid/liquid interfaces. In here, we addressed two separated, but interconnected problems:

First, we consider water adhesion on fiber/surface, responsible for the emergence of droplet residue upon droplet detachment. In this project, we study the mechanism of water droplet detachment and retention of residual water on smooth hydrophilic fibers and surfaces using nonequilibrium molecular dynamics simulations. We investigate how the applied force affects the breakup of a droplet and how the minimal detaching force per unit mass decreases with droplet size. We extract scaling relations that allow extrapolation of our findings to larger length scales that are not directly accessible by molecular models. We find that the volume of the residue on a fiber varies nonmonotonically with the detaching force, reaching the maximal size at an intermediate force and associated detachment time. The strength of this force decreases with the size of the drop, while the maximal residue increases with the droplet volume, V , sub-linearly, in proportion to the $V^{2/3}$.

Second, we address the adhesion on conducting graphene. We improved the graphene model by incorporating the conductivity of graphene sheet using the fluctuating charge technique of Constant Potential Molecular Dynamics (CPMD). We evaluated the wettability by measuring the contact angle of cylindrical water drops on a conducting graphene sheet. We found that the CA of a water droplet on a graphene sheet supported by water is lower than in the absence of water under graphene. Our calculations reveal effective attractions between partial charges of equal sign across the conducting graphene sheet. Attractive correlations are attributed to the formation of the highly localized image charges on carbon atoms between the partially charged sites of water molecules on both sides of graphene. By performing additional computations with nonpolar diiodomethane, we confirm that graphene transmits both polar and dispersive interactions. These findings are important in applications including sensors, fuel cell membranes, water filtration, and graphene-based electrode material to enhance the supercapacitor performance. A challenge for future work concerns dynamic polarization response of wetted graphene at alternating (AC) field condition.

Chapter 1: Introduction

Understanding how interfacial interactions control systems such as nanofluids, and polymer nanocomposites, is of considerable interest both scientifically and for technological applications. Deep understanding of solid–liquid interactions at a molecular level is important for technological applications such as surface coating, self-cleaning, oil recovery applications.¹

The interaction of a liquid with a solid is characterized by the word ‘wetting’. Wetting can involve spreading of a liquid over a solid surface, the penetration of a liquid into porous materials, or the displacement of one liquid by another (Figure 1).² While there is always some attraction between any liquid/solid pair, the spontaneity of wetting depends on the combined effect of the change of solid/liquid, solid/gas, and liquid/gas areas in the process.³

The solid/liquid interface plays a fundamental role in diverse fields and helps with an understanding of the physical phenomena and structural knowledge of the interface, at the atomic scale, for example in catalysis, crystal growth, lubrication, electrochemistry, colloidal system, and in many biological reactions. Unraveling the atomic structure at the solid/liquid interface is, therefore, one of the major challenges facing the surface science today to understand the physical processes in model systems. Driving force of spontaneous interface formation and the reason that they remain stable is Adhesion.

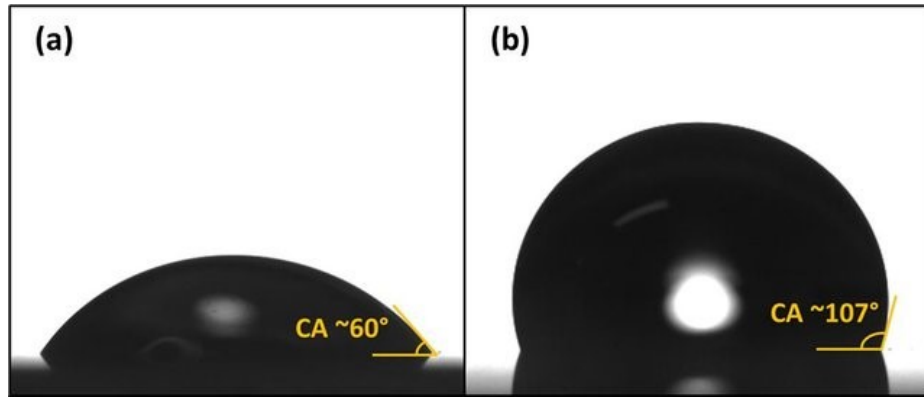


Figure 1: Image of water droplets supported on (a) hydrophilic, and (b) hydrophobic surfaces.

1.1 Basic surface thermodynamics

The contact angle measurement is the best experimental approach to obtaining the strength of interaction between liquid and solid. The contact angle is the angle, conventionally measured through the liquid, where a liquid/vapor interface meets a solid surface³ (Figure 2).³ The contact angle quantifies the wettability of a solid surface by a liquid via the Young equation⁴

$$\cos\theta = \frac{\gamma_{SV} - \gamma_{SL}}{\gamma_{LV}} \quad (1)$$

where γ_{SL} , γ_{LV} , and γ_{SV} are the surface free energies or interfacial tensions of the solid-liquid, the liquid-vapor, and the solid-vapor interfaces. A contact angle less than 90° usually indicates that wetting of the surface is favorable, and the fluid will spread over a large area of the surface. Contact angles above 90° , generally mean that wetting of the

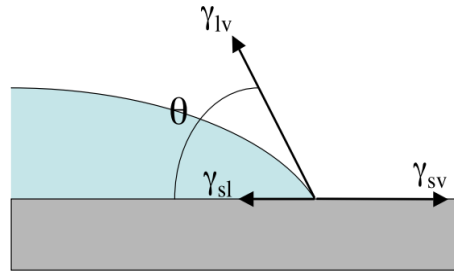


Figure 2: Schematic of a liquid drop showing the quantities in the Young equation.

surface is unfavorable, so the fluid will minimize contact with the surface in favor of a more compact liquid droplet.

The wetting ability of a liquid is a function of the surface energy of the solid-gas interface, the liquid-gas interface, and the solid-liquid interface. The surface energy across an interface or the surface tension at the interface is a measure of the energy required to form the unit area of a new surface at the interface. The intermolecular bonds or cohesive forces between the molecules of a liquid cause surface tension. When the liquid encounters another substance, there is usually an attraction between the two materials. The adhesive forces between the liquid and the second substance will compete against the cohesive forces of the liquid. Liquids with weak cohesive bonds and a strong attraction to another material (or the desire to create adhesive bonds) will tend to spread over the material. Liquids with strong cohesive bonds and weaker adhesive forces will tend to bead-up or form a droplet when in contact with another material.

Depending on the thermodynamic state or the hydrodynamic status of the liquid drop in which the contact angle is measured, two types of contact angles can be defined. If the

contact angle is measured when either the liquid drop continues to spread or when its thermodynamic state conditions continue to change, the measured contact angle is termed the dynamic contact angle. However, if the contact angle is measured under conditions in which the liquid drop is stationary and the surrounding conditions are in the steady state, the measured contact angle is known as the static/equilibrium contact angle. The dynamic contact angle can also reflect the hydrodynamic conditions, whereas the equilibrium contact angle depends only on the surface properties of the solid-liquid-vapor system under the given thermodynamic conditions.

As we mentioned before, if the three tensions are known, the wetting state of the fluid follows directly. If $\gamma_{SV} < \gamma_{SL} + \gamma_{LV}$, a droplet with a finite contact angle minimizes the free energy of the system; we speak of partial wetting. On the other hand, if $\gamma_{SV} = \gamma_{SL} + \gamma_{LV}$, the contact angle is zero. The system will consequently be in equilibrium when a macroscopic uniform liquid layer covers the whole solid surface, and we speak of complete wetting. The distinction between the different wetting states is usually made by considering the equilibrium spreading coefficient $S_{eq} \leq 0$, which represents the surface free energy γ_{SV} relative to its value for complete wetting³:

$$S_{eq} \equiv \gamma_{sv} - (\gamma_{SL} + \gamma_{LV}) = \gamma(\cos\theta - 1) \quad (2)$$

Figure 3 shows the three wetting states that may exist in any three-phase system. For a solid-liquid-vapor system, complete drying would correspond to the intrusion of a macroscopic vapor layer between the solid and the liquid. “Drying” does not imply evaporation; see below. From a thermodynamic point of view, the wetting

and drying states are very similar, the only difference being that liquid and vapor reinterchanged. In practice, drying is rather rare with mercury on, for instance, glass as a notable exception since van der Waals forces tend to thin vapor layers. Partial wetting corresponds to drops, surrounded by a microscopically thin film adsorbed at the surface, and complete wetting to a macroscopically thick layer. In a partial wetting state the surface apart from the droplet is usually not completely dry. In

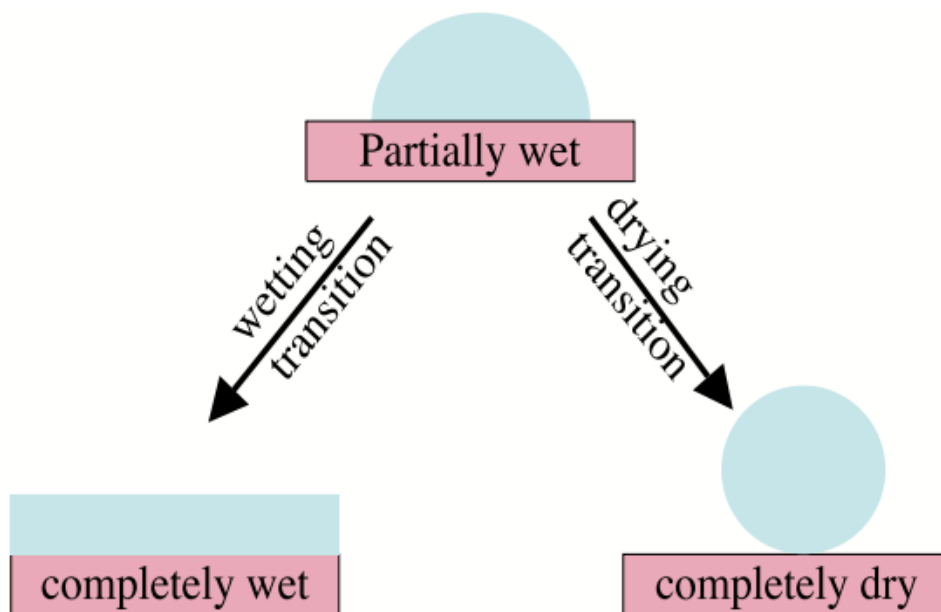


Figure 3: The three different possible wetting states according to Young's equation

thermodynamic equilibrium there will be at least some molecules adsorbed onto the substrate. It is for this reason that we speak of a microscopic film; in experiments the average thickness of this film varies between a fraction of a molecule to several molecules, depending on the affinity of the molecules for the substrate, and the distance to the bulk critical point.

Note that for complete wetting the equilibrium spreading coefficient is zero or positive.

The solid-vapor interface then consists of a macroscopically thick wetting layer, so that its tension is equal to the sum of the solid-liquid and liquid-vapor surface tensions.

The Young equation can also be derived thermodynamically for the ideal planar solid surface of Figure 2, provided that the system is treated as one in thermal and mechanical equilibrium and the quantities γ_{SL} , γ_{LV} , γ_{SV} are defined as follows⁵:

$$\begin{aligned}\gamma_{SL} &= \left(\frac{\partial F}{\partial A_{SL}} \right)_{T, \mu_i} \\ \gamma_{SV} &= \left(\frac{\partial F}{\partial A_{SV}} \right)_{T, \mu_i} \\ \gamma_{LV} &= \left(\frac{\partial F}{\partial A_{LV}} \right)_{T, \mu_i}\end{aligned}\tag{3}$$

where F is the Helmholtz free energy (or the work function) of the system, A_{SV} is the area of the solid-vapor interface, etc., T is the temperature, and μ_i is the chemical potential of each component in the phases present. Implicit in this treatment, and also in Young's derivation, is the assumption that the contact angle is independent of the volume of the drop and depends only on the temperature and the nature of the liquid, solid, and vapor phases in contact.

In most applications, it is the contact angle that determines the behavior of the wetting system rather than the surface tension of the solid, but when complete wetting happens,

contact angle stops being a precise measure of wetting adhesion strength. In this case, we can use the work of adhesion Φ_{adh} as an alternative way to characterize interfacial tension⁵.

$$-\Phi_{adh} = \gamma_{LV} + \gamma_{SV} - \gamma_{SL} \quad (4)$$

This equation is simply the thermodynamic expression of the fact that the reversible work of separating the liquid and solid phases must be equal to the change in the free energy of the system. The three terms on the right of Equation (4) are the free energies per unit surface area of the liquid-vapor, solid-vapor, and solid-liquid interfaces, respectively. Instead of using individual interfacial tensions, Equation (4) can be rewritten as⁶

$$-\Phi_{adh} = \gamma(1 + \cos\theta) \quad (5)$$

Equation (5) expresses the reversible work of adhesion of the liquid to the solid in terms of the liquid surface tension and the contact angle for the given solid and liquid.

1.2 Droplet detachment from a fiber

The adherence to, and removal of droplets from cylindrical fibers underlie applications from fog harvesting,⁷⁻⁹ oil–water and oil–air separation, and water transport in fuel cells.¹⁰⁻¹³ In all these applications, the performance of the system depends on the conditions for the liquid release from, and the extent of retention by the fibers,¹⁴ and quantitative information about droplet–fiber interaction is of great value in designing a new product. The equilibrium shape of a droplet on fiber has been examined in reasonable depth in the literature.¹⁵⁻¹⁹ For droplets and fibers in the micrometer range, it is known that when the gravity effect is negligible, two topologically distinct droplet shapes occur: asymmetric clamshell and axially symmetric barrel conformations, depending on the droplet volume, the contact angle, and the fiber radius (see Figure 4).^{18, 20} Fiber roughness and fiber orientation can also have a significant effect on the equilibrium shape of droplet and wettability.²¹⁻²³

Motivated by various applications in the field of automotive engineering, e.g., removal of airborne oil droplets from the engine exhaust via the so-called coalescence filters, experimental studies have been conducted to measure the force required to detach a droplet from a fiber and to use that information to estimate an allowable velocity for the flow of smoke through a filter.²⁴⁻²⁷

Using continuum simulations, the equilibrium shape of an isolated droplet deposited on a fiber under the influence of an enhanced external body force has been determined recently

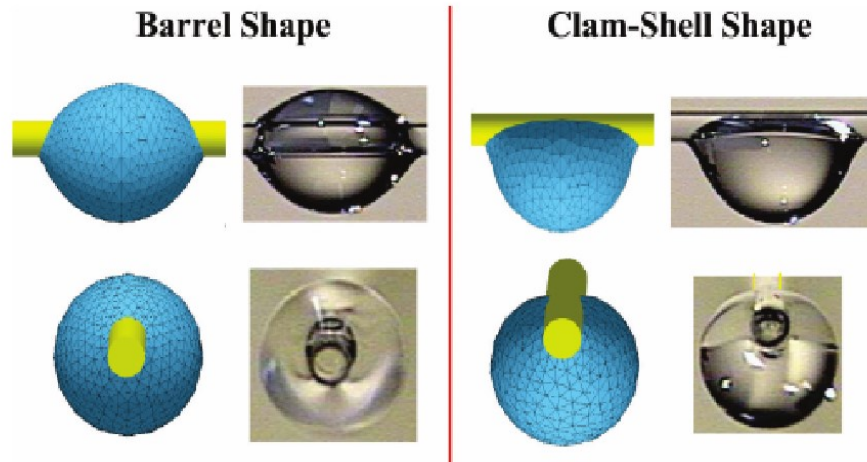


Figure 4: Schematic and macroscopic drops from experiment representing barrel and clamshell shapes of a water droplet on a fiber.

by Amrei et al.²⁸ These authors incrementally raised the magnitude of the external body force applied to a droplet until no equilibrium shape/position could be obtained for the droplet on the fiber. They referred to the maximal force the droplet could sustain in an equilibrated state as the force of detachment and studied its dependence on fiber diameter, fiber roughness, fiber wettability, and droplet volume.^{21, 29-33} The continuum simulations,²⁸ however, could not resolve the time-dependent dynamics of droplet detachment, and more importantly, the volume of the droplet residue on the fiber. The latter is especially important from an industrial viewpoint as it affects the repeatability of the droplet separation processes. For instance, to increase the efficiency of fiber filters, the volume of the residue should be suppressed to prevent the clogging of the fiber network,^{23, 34, 35} while in water harvesting increasing the residue volume on the fiber arrays improves the net's

efficiency.⁸ The residual volume depends on the droplet volume, the contact angle, fiber radius, and the surface microstructure on the natural fiber.^{23, 36} Despite the importance of knowing the amount of the residue on the fiber in engineering processes, only a few studies report on the volume of the residue on the fibers. For instance, Weyer *et al.*³⁷ investigated the droplet motion on the crossed fibers and demonstrated that, depending on the fiber diameter and volume of the droplet, a controllable liquid residue remained at the fiber nodes. Kim *et al.*³⁴ also studied the droplet impact on a thin fiber and suggested the mechanical model that predicted the residual water mass on the fiber with respect to the fiber radius and impact speed. None of the previously reported studies, either experimental or computational, have discussed the detachment of a droplet from a fiber when the external force was stronger than the detachment force. Likewise, no study has yet reported the volume of the residue left on a fiber when the droplet was detached with a force stronger than the detachment force (e.g., the volume of the residue on a fiber when the velocity of the flow through a filter exceeded an allowable velocity).

1.3 Adhesion on conducting surface

Recently, the interest in metallic electrodes in electrochemistry lead to the development of a methodology suitable for extremely polarizable and conducting substrate to model electrodes.³⁸ Sprik and Siepmann³⁹, who studied the adsorption of water molecules at metallic surfaces, developed a model of electrode polarization. This model modified by Madden and coworkers⁴⁰ is based on fluctuation charge on the electrode surface. More information about this model can be found in section 3.2.

We use the model to study the adhesion at the conducting solid and liquid interfaces in graphene. We model conductor atoms (carbon atoms in graphene) using the fluctuating-charge technique of the Constant Potential Molecular Dynamics(CPMD),^{40, 41} which alleviates geometric restrictions of the more efficient image-charge approach.

1.3.1 Water adhesion on conducting graphene

An atomically thin layer of graphene, a single-atom-thick sheet of sp^2 -hybridized carbon atoms arranged in a hexagonal honeycomb lattice, exhibits unique mechanical, optical, and electronical properties⁴²⁻⁴⁹. As a result, graphene has become a subject of intense basic and applied research⁵⁰⁻⁵⁶. For example, because of its extraordinary surface to volume ratio^{57, 58}, experimentalists have suggested graphene-based electrodes can enhance the performance of supercapacitors^{41, 58} and batteries^{59, 60}. Extremely thin and electrically conductive, graphene is widely used in biosensors^{61, 62}, lab-on-a-chip, fabrication of membranes for water filtration⁶³ and desalination, manufacture of fuel cells, and microfluidics platforms where graphene is in contact with water, vapor, and analytes.^{64, 65} Many of the above applications critically depend on the graphene wettability in water. Wetting properties of graphene have been a subject of several theoretical and experimental investigations over the last decade⁶⁶⁻⁶⁹, however, fundamental characterization and molecular level understanding of wetting phenomena on graphene remain incomplete. Moreover, an accurate measurement of the contact angle (CA)⁷⁰⁻⁷² on graphene is often difficult to accomplish because of defects, airborne contaminants, and oxide formation on the surface.

Contact angle measurements have also revealed a significant dependence of graphene wettability on the supporting substrate, a phenomenon often interpreted as a consequence of graphene transparency to water-substrate interactions^{67, 73-76}. For instance, the water static contact angle on neat graphene supported by copper is 44°, while it is 60° for the pyrolytic graphite⁶⁶. The experimental estimate for suspended graphene, on the other hand, has been reported⁷⁶ at 85±5°, close to theoretical predictions^{69, 77,78} of 87°, 90°, and 79°, respectively. The effect is not limited to solid substrates. Comparisons between contact angles on suspended graphene with those measured on graphene fragments supported by water have generally shown increased wettability when graphene was surrounded by water from both sides. Early MD simulations indicated the contact angle of a water droplet on a graphene sheet is about 7° lower when the system is submerged in water⁶. Experiments performed by Checco and his group⁷⁶ using graphene on a pillared substrate revealed an even bigger effect. Replacing air between the pillars by water resulted in estimated CA reduction between 19 and 24° (Figure 5).

A qualitatively similar effect has been observed with ice or hydrogel support replacing the underlying water⁷⁹. The clear distinction between graphene wettabilities in the presence and absence of supporting substance has important repercussions for the predictions of graphene properties in dispersions. Theoretical predictions of the effect have mostly focused on direct interactions between water molecules and solid or liquid support on the opposite side of the sheet. Based on the Young-Dupre equation, the contact angle of a graphene-coated substrate should correspond to the adhesion strength associated with combined attraction exerted on the water by graphene and the supporting substrate^{4, 73-76},

or underlying liquid^{6, 76}. Using a simple mean-field method for pair-wise additive dipolar and dispersive interactions, Driskill *et al.*⁶ estimated the contact angle difference $\Delta\theta$ between graphene platelets supported by water and air to be near -10° .

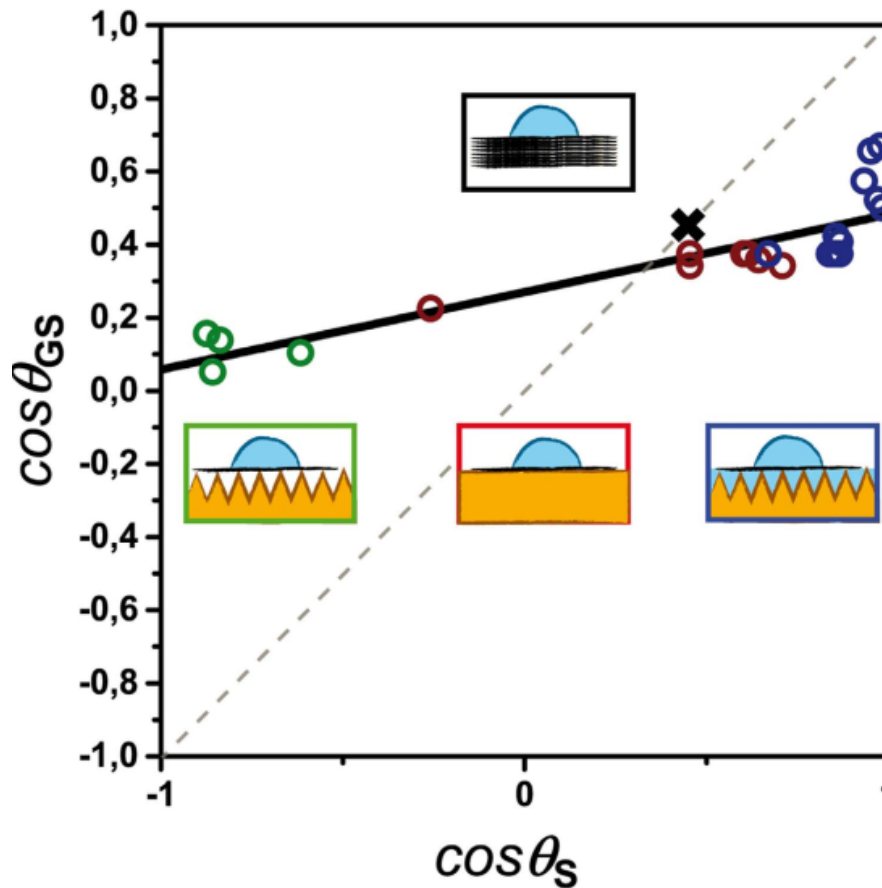


Figure 5: Experimental measurement of the water contact angle on a single graphene sheet almost completely suspended on air or supported by water, by varying the fraction of solid area of the support.

A somewhat smaller CA reduction, nearly independent of the hydrophilicity of the model graphene, was found in parallel Molecular Dynamics simulations for the same model system (Figure 6). While the presumed interaction additivity provided a plausible rationale

for early experimental observations, it also resulted in considerable quantitative differences between predicted and measured CA in numerous cases. Following comparisons with

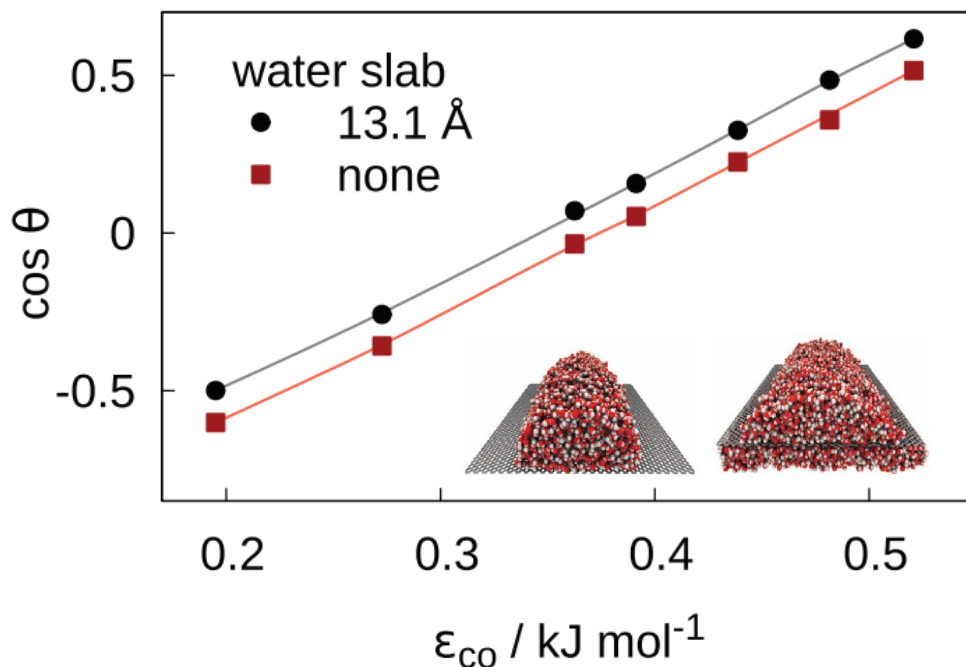


Figure 6: MD simulation of water contact angle on a single graphene sheet almost completely suspended on and supported by water

experiments, *ab initio* modeling, and classical accounts of multi-body interactions, a number of groups have also discussed substrate-induced changes of the electronic structure of graphene, which in turn affect graphene-water forces and propensity for wetting^{58, 66, 80-82}. Distinct but interrelated effects predicted in first principles studies^{66, 81-83} include local (atomic) and large-scale polarization events, the shift in graphene Fermi level, and charge transfer between substrates and graphene, all of which can potentially tune graphene's apparent polarity^{84, 85}. When graphene is supported by a polar liquid like water, polarization effects are expected to play a notable role, however, prohibitive system sizes and slow

statistical convergence have so far precluded direct estimates of these effects on wetting properties in *ab initio* simulations. Atomic polarizability of graphene has been considered in classical MD calculations with polarizable force fields based on charge-on-spring (Drude oscillator), or OPLS-AA models^{58, 80,86}. While these studies offer first valuable insights into the role of molecular polarizabilities, the underlying models underestimate the large-scale polarization associated with the lateral mobility of π electrons in the conducting graphene sheet and cannot capture the very pronounced anisotropy^{87, 88} of its polarizability tensor, a weakness shared with discontinuous-dielectric model alternatives⁸⁹⁻⁹¹.

Chapter 2: Water adhesion on hydrophilic surfaces

2.1 Droplet detachment from a fiber

In the present work, we study the mechanisms of droplet detachment and retention of liquid droplets through the atomistic molecular dynamic (MD) simulations. While valid insights could in principle follow from continuum simulations, our approach relies directly on input atomic and molecular forces rather than on experimental data for presumably invariant and uniform macroscopic properties such as the interfacial tensions, viscosity, drop's perimeter friction,⁹² and possibly line tension effects. We address the fundamental questions about the droplet size-dependence of the minimal force capable of detaching a droplet from the fiber, and the effects of droplet size and applied force on the amount of liquid residue left on the fiber after the detachment. Our modelling studies of the droplet breakup uncover a strongly nonmonotonic influence of external force, with the amount of residual water maximized under the intermediate force strengths whereas a complete or near-complete detachment of the droplet can be achieved in both extremes, with the applied force only slightly, or considerably exceeding the minimal force of detachment. We perform multiple MD simulations for water droplets on a smooth hydrophilic fiber at varied system sizes and extract scaling relations that enable extrapolation of our findings to larger length scales that are not directly accessible by molecular models. Because of its fundamental appeal and importance for applications, we hope the work will inspire experimental investigations and theoretical analyses of liquid retention and its control through varied stimuli for droplet detachment from the fibers.

2.2 Methodology

2.2.1 Force fields

The model fiber was built with Visual Molecular Dynamic (VMD) package.⁹³ It consists of a rigid carbon nanotube with radius $r_f = 6.4 \text{ \AA}$ or 12.8 \AA comprised of 4336 or 22503, Lennard Jones (LJ) carbon atoms.^{6, 94} The radius of the fiber is held fixed during the simulation. To avoid possible finite size effects, the fiber is periodically replicated along the x-direction. We use the rigid extended simple point charge (SPC/E) potential to model the atomistic water droplet.^{95, 96} The model has been used repeatedly in studies of capillary phenomena involving water because it offers satisfactory estimates for water surface tension and wettability for a variety of materials. The use of this force field is motivated by our recent dynamic studies of bulk and confined water.^{62, 92, 94, 97-104} This potential consists of a smoothly truncated Coulomb potential acting between partial point charges on oxygen ($-0.8476e_0$) and hydrogen ($0.4238e_0$) atoms and an O–H distance 1 \AA and the

H–O–H angle at 109.471 (Figure 7). Further, oxygen atoms also interact via Lennard Jones potential (LJ).

In all our atomistic simulations the water–fiber interaction is based on Lennard-Jones potential between the SPC/E water molecules and the fiber (Figure 8). The LJ strength was characterized by $\epsilon_{co} = 0.6639 \text{ kJ mol}^{-1}$ with cutoff radius 11 Å.

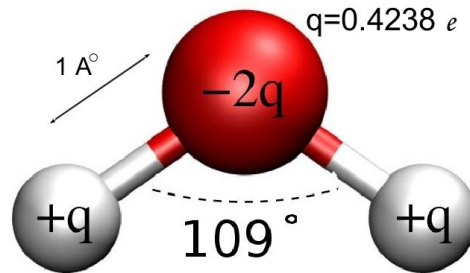


Figure 7: SPC/E water model

When simulating a larger fiber, which requires bigger droplets to cover the same range of reduced volumes $V_r = V/r_f^3$, we use the coarse-grained, monatomic water (mW)^{105, 106}

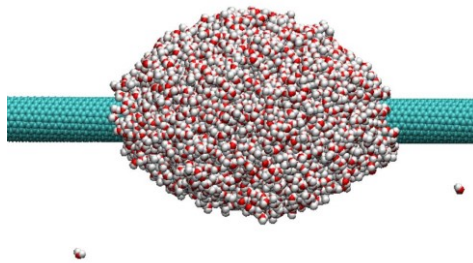


Figure 8: Equilibrium barrel shape of a 2000 molecules atomistic droplet on a fiber with $r_f = 6.4 \text{ \AA}$.

model to reduce the computational cost. We selected this model because of its similar properties¹⁰⁵ with the atomistic model (SPC/E) at room temperature¹⁰⁷ such as contact angle, surface tension, and work of adhesion. The model does not feature electrostatic interactions associated with explicit hydrogen and oxygen atoms. Each mW water molecule behaves as a single site particle, which is interacting with its neighbors through a short-ranged potential designed to form a tetrahedral structure. The intermolecular potential is comprised of a sum of pairwise two-body term, (Φ_2), and three-body interactions, (Φ_3), that have the form of the Stillinger–Weber potential (SW).¹⁰⁶ In the coarse-grained water model, the interaction between the water molecules and the fiber is modeled with the two-body SW potential with the contact distance water–carbon $\sigma = 3.2$ Å.

$$E = \sum_i \sum_{j>1} \Phi_2(r_{ij}) + \sum_i \sum_{j\neq 1} \sum_{k>j} \Phi_3(r_{ij}, r_{ik}, \theta_{ijk}) \quad (6)$$

$$\begin{aligned} \Phi_2(r_{ij}) &= A\varepsilon \left[B \left(\frac{\sigma}{r} \right)^p - \left(\frac{\sigma}{r} \right)^q \right] \exp\left(\frac{\sigma}{r - a\sigma} \right) \\ \Phi_3(r, s, \theta) &= \lambda\varepsilon [\cos\theta - \cos\theta_0]^2 \exp\left(\frac{\gamma\sigma}{r - a\sigma} \right) \exp\left(\frac{\gamma\sigma}{s - a\sigma} \right) \end{aligned} \quad (7)$$

with $A = 7.049556277$, $B = 0.6022245584$, $\gamma = 1.2$, $a = 1.8$, $\theta_0 = 109.47^\circ$, the diameter $\sigma_{mW} = 2.3925$ Å, and energy scale $\varepsilon = 6.189 \text{ kcal mol}^{-1}$. These are the most satisfactory parameter choice for SW potentials.¹⁰⁸ The parameter $\lambda = 23.15$ is a measure

of the tetrahedrality of the potential. The higher the value of λ , the more tetrahedral the model is.

To start from barrel shape droplet (Figure 9), we considered $e_{c-mW} = 0.8158 \text{ kJ mol}^{-1}$ for carbon–mW interaction. All intermolecular forces in the mW model vanish at a distance a , where $a = 1.8$.¹⁰⁹



Figure 9: Equilibrium barrel shape of atomistic droplet on a fiber with $r_f = 12.8 \text{ \AA}$

2.2.2 Simulation details

The simulations start by placing a water droplet on a cubic lattice above the fiber positioned along the z axis of a cubic simulation box of size 300 \AA . During the equilibration, the droplet on the fiber reaches the symmetric equilibrium barrel shape. We considered seven sizes of water droplets composed of 2×10^3 , 4×10^3 , 6×10^3 , 8×10^3 , 10×10^3 , 13×10^3 , and 17×10^3 water molecules which were represented by the atomistic water model, SPC/E,⁹⁶ on top of a rigid fiber with radius $r_f = 6.4 \text{ \AA}$. Based on volumes of the droplets, (V), and fiber

radius r_f , the reduced volume of the system, V_r , varied from 250, 500, 750, 1000, 1250, 1500, and 2000. Depending on the size of the droplet, the total length of the simulation run varied from 2.5 to 5 ns.

For the simulations with a fiber with a radius of $r_f = 12.8 \text{ \AA}$, we used the coarse-grained monatomic water (mW).^{105, 106} By considering the same reduced volumes as with the atomistic droplets, the droplets comprised $1.7 \times 10^4, 3.4 \times 10^4, 5.2 \times 10^4, 6.9 \times 10^4, 8.7 \times 10^4, 10.4 \times 10^4, \text{ or } 13.9 \times 10^4$, mW water molecules.

Depending on the size of the droplet, the total length of the run varied from 5 to 10 ns.

All MD simulations are carried out by using the LAMMPS package¹¹⁰ in NVT ensemble. The temperature is kept constant at 300 K using the Nose–Hoover thermostat¹¹¹ with a relaxation time of 0.2 ps. Verlet integration is used with time step 1 fs for atomistic water and 5 fs for coarse-grained water. Periodic boundary conditions are applied and long range coulombic-PPPM Ewald summation with 10^{-5} accuracy is used in SPC/E simulations.

The detachment of a droplet from the fiber was studied by using Non-Equilibrium Molecular Dynamics (NEMD). In numerical simulations, we used two approaches to apply the external force to the droplet. In the first approach, an external force was exerted on every molecule of a droplet, and its strength was increased gradually until the droplet detached from the fiber (Figure 10). In the second approach, after reaching the equilibrium state, a constant force was applied to every molecule in the droplet in a direction perpendicular to the fiber and remained constant during the simulation (Figure 10b).

Using sufficiently slow rate of force increase, the two methods yield consistent estimates of the minimum detachment force of the droplet. However, applying the constant force eliminates any concern about the appropriate rate of force escalation. We therefore mostly considered the second method using the constant force on the droplet. Depending on the force strength, the time necessary to observe the detachment varied from 50 ps to 2 ns for the strong and weak forces, respectively.

To accommodate large drops, we also increase the size of the box in the direction of the force applied to the droplet (Figure 11).

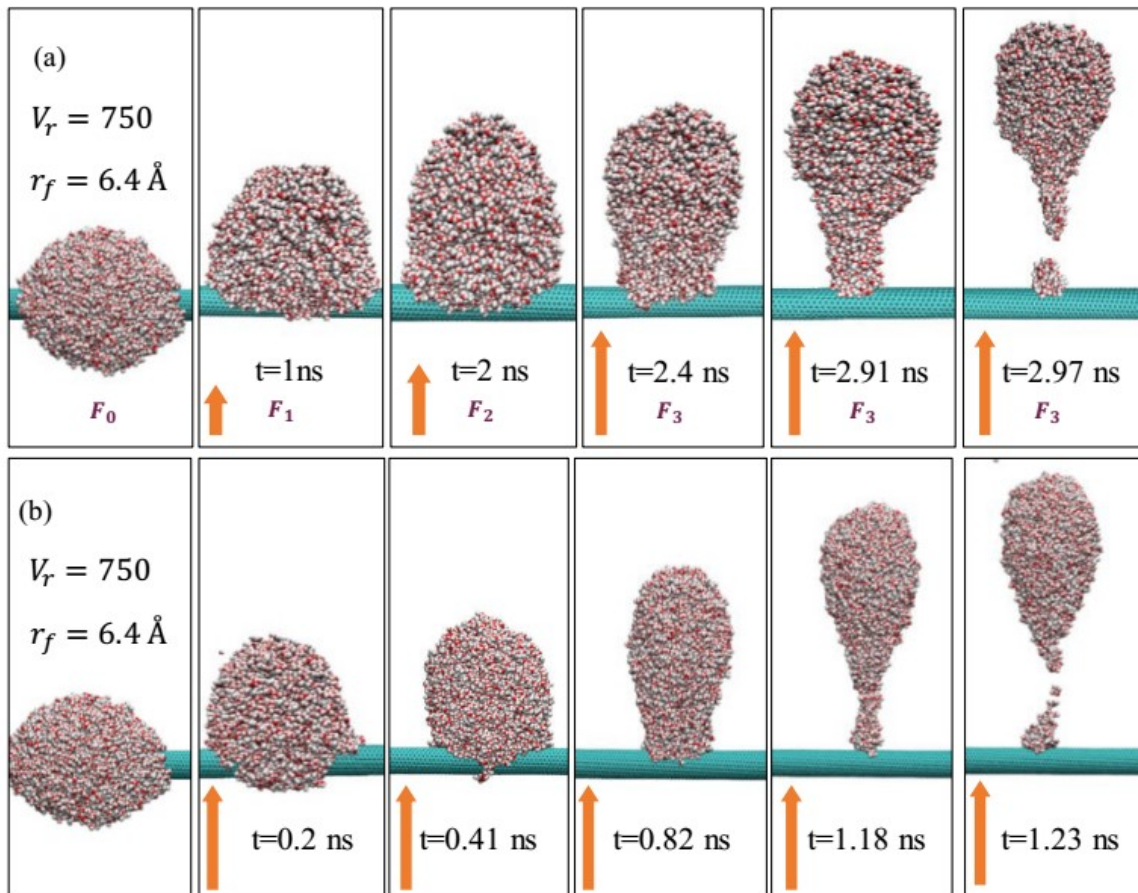


Figure 10: Snapshots from a MD trajectory during the droplet detachment from a fiber for the atomistic model with $V_r = 500$ and fiber radius $r_f = 6.4 \text{ \AA}$. (1-a): snapshots at different times t and corresponding external forces $F_0 = 0$, $F_1 = 0.0041$, $F_2 = 0.0046$, $F_3 = 0.005 \text{ kJ mol}^{-1} \text{ \AA}^{-1}$. The force is increased gradually until the drop is about to detach from the fiber. (1-b): snapshots showing the evolution of droplet shape at constant force, $F = 0.0058 \text{ kJ mol}^{-1} \text{ \AA}^{-1}$, exerted on the droplet during the simulation.

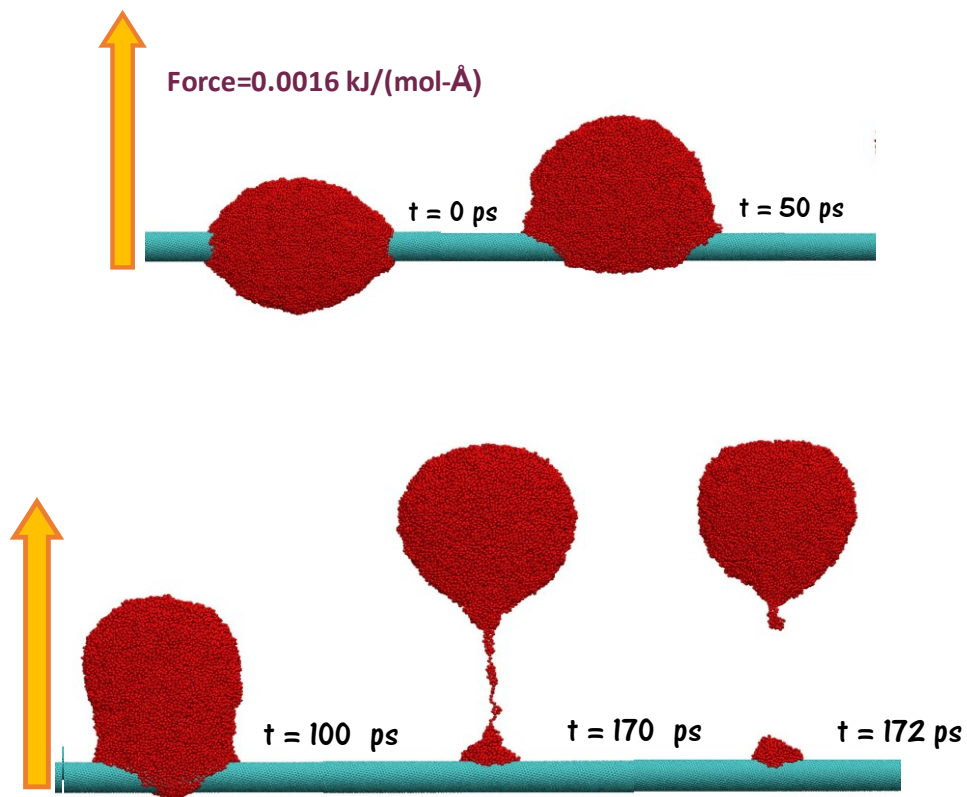


Figure 11: Snapshots from a MD trajectory during the droplet detachment from a fiber for the coarse-grained model with $V_r = 500$ and fiber radius $r_f = 12.8 \text{ \AA}$.

2.3 Results and discussions

2.3.1 Droplet equilibrium shape on a fiber

In Figure 12, we plot a morphology diagram for atomistic water droplets on a fiber with radius $r_f = 6.4 \text{ \AA}$ as a function of the reduced volume and the strength of water–fiber interaction. The squares and triangles represent the conditions where the equilibrated droplets are of clamshell or barrel shape, respectively. We have found that weak water–fiber interactions and small droplet volume favor the clamshell shape, while for strong water–fiber interactions and large droplet volume only the barrel shape is stable. With nanosized droplets on a smooth fiber, we do not observe a bistability of the two morphologies that has been reported with macroscopic droplets for a wide range of parameters.¹¹¹ Comparatively low barriers between the two configurations of the droplets on the nano-sized fiber rationalize the absence of the bistable regime in nanoscale systems.

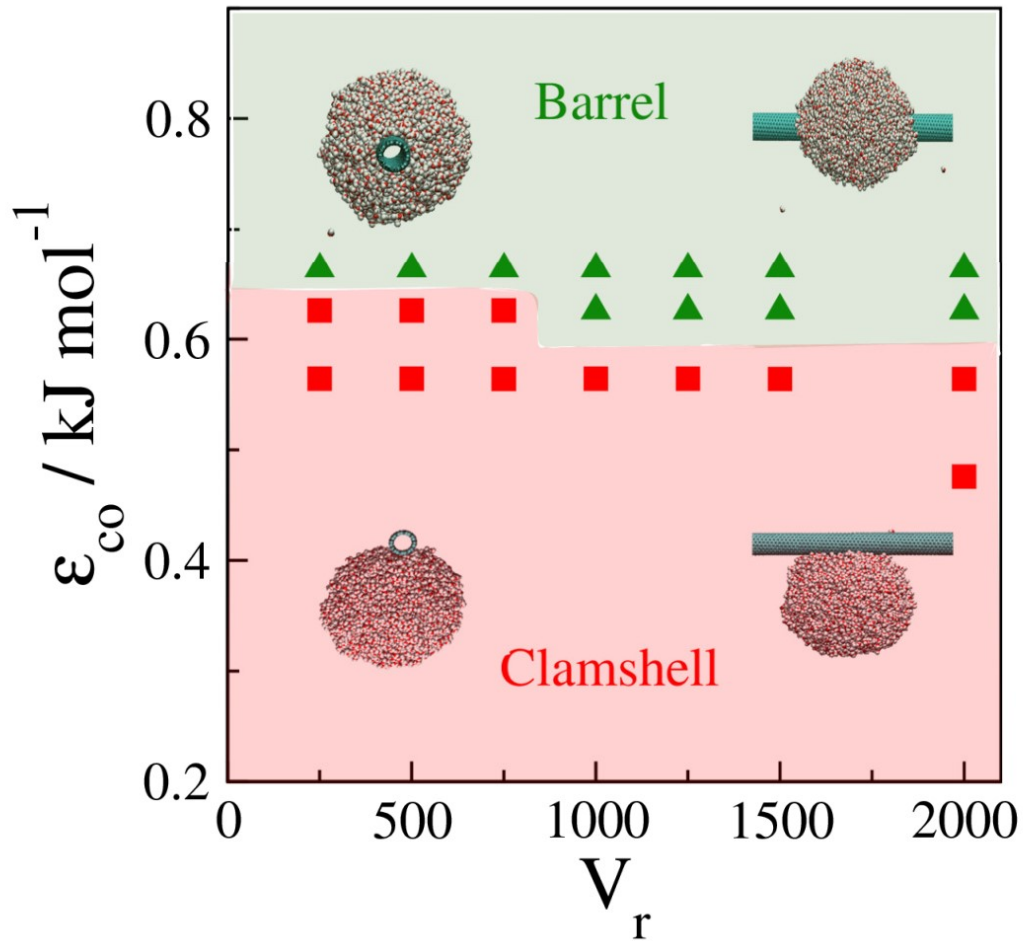


Figure 12: Morphology diagram of atomistic droplets deposited on a smooth fiber with fiber radius, $r_f = 6.4 \text{ \AA}$, at varied reduced volumes and water-fiber interactions. Green triangles denote the states where simulated droplets were consistently of stable barrel shape. Red squares show when the clamshell shape was stable. The number of water molecules corresponding to the given range of V varies from 2000-17000. The threshold value of carbon-water interaction strength $\epsilon_{co} = 0.6 \text{ kJmol}^{-1}$ corresponds to water-substrate contact angle 33° , which can result in bistability in macroscopic systems.

2.3.2 Droplet behavior in the presence of an external force

Figure 13 shows consecutive snapshots from MD trajectories of the atomistic droplet in the presence of external forces. The force is applied in the direction perpendicular to the fiber. It can be seen (Figure 13a) that for the weak force, the droplet shape transforms from symmetric barrel shape to asymmetric clamshell conformation. When the force per molecule becomes strong enough, the droplet eventually detaches from the fiber, but a certain percentage of droplet mass can remain on the fiber (Figure 13b).

When applying a strong force on the droplet, the droplet shape doesn't fully transition to the clamshell (Figure 13c), and it can detach as a whole. Figure 13e shows another possible outcome of applying a strong force to the droplet. It can be seen from a front view that the droplet detaches before reaching the clamshell shape. The snapshots of the coarse-grained system with fiber radius $r_f = 12.8 \text{ \AA}$ are also added to Figure 13d for comparison. As can be seen in Figure 13d, the bigger drops considered by the CG model detach faster from the fiber compared to the smaller ones represented by the AT model. The higher rates might be related to the differences in water diffusivity in the two models, with a diffusion coefficient of mW model 2.3 times bigger than the one of SPC/E model⁹⁶.

To understand the breakup mechanism and determine the amount of residue of a nanoscale liquid droplet on the fiber, we perform multiple independent simulation runs. As illustrated in Figure 14 (a-b) by applying the same force to the droplet, the amount of remaining water on the fiber varies alters from one simulation run to another. The variation of the residue size takes place because when a droplet stretches, it creates a narrow neck whose breakup

position is subject to large fluctuations.¹¹²⁻¹¹⁴ In Figure 14 (c-e), we also illustrate the formation of a small satellite droplet emerging upon the breakup of the drop.¹¹²⁻¹¹⁴ In this case, the satellite droplet separated from the droplet after it detached from the fiber. The visualization of the breakup trajectory revealed that the process of detachment from the fiber resembles the droplet breakup in the nano jet.^{112, 113} In these studies, thermal fluctuations at the nanoscale were identified as the major cause of the irregular detachment.¹¹⁵

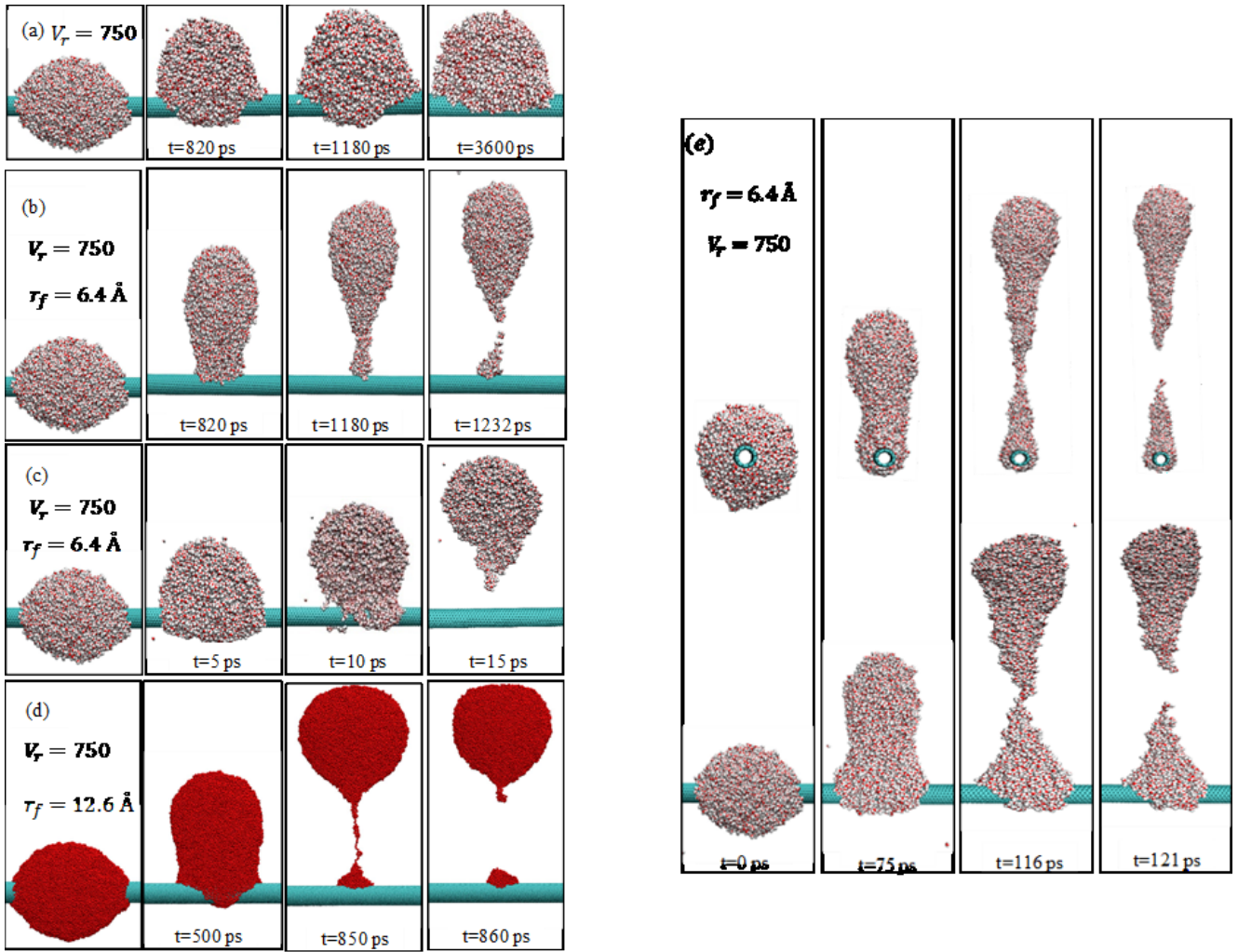


Figure 13: Snapshots from MD trajectories of the droplet detachment from fiber for the atomistic model and $V_r = 750$ (6×10^3 water molecules). Figures a-c illustrate the droplet evolution at different external forces,

$F = 0.0041, 0.0058, \text{ or } 0.41 \text{ kJ mol}^{-1} \text{ \AA}^{-1}$ applied to the droplet in the direction perpendicular to the fiber. The atomistic droplet consists of 6000 SPC/E water molecules on the fiber with a radius $r_f = 6.4 \text{ \AA}$. Figure d presents snapshots from an MD trajectory of the droplet detachment from a fiber for a coarse-grained model at $V_r = 750$.

The force exerted on the droplet was $F = 0.0016 \text{ kJ mol}^{-1} \text{ \AA}^{-1}$. The droplet consists of 52428 mW water molecules and the fiber radius is 12.8 \AA . Figure e, side view (bottom) and front view (top) snapshots from MD trajectories of the droplet detachment from fiber for the atomistic model with $V_r = 750$ and $F = 0.016 \text{ kJ mol}^{-1} \text{ \AA}^{-1}$ a the force strength that maximizes the average residue on the fiber at given V_r .

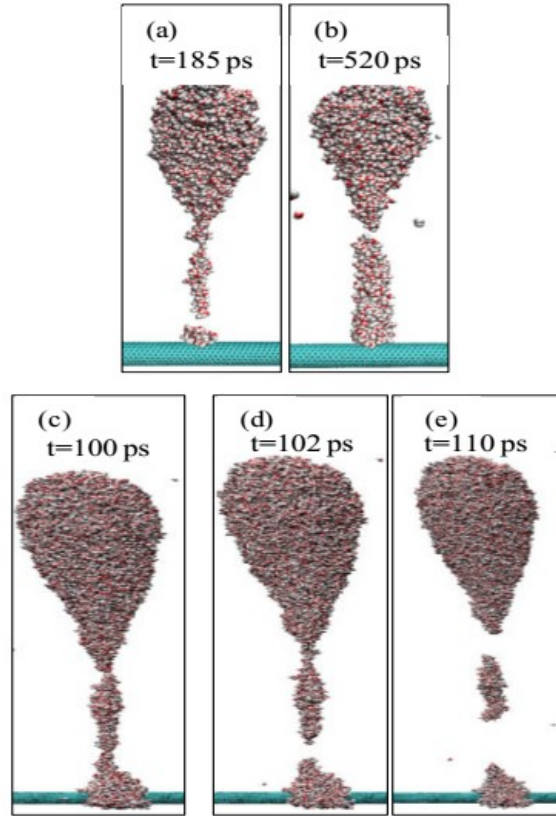


Figure 14: Snapshots from MD trajectories of the droplet detachment from a fiber for the atomistic model. Figures a-b show that the breakup happens at different distances from the fiber and different times for two different atomistic simulations with $V_r = 500$. The droplet consists of 4000 SPC/E water molecules and the fiber radius is 6.4 \AA . The force is $F=0.0125 \text{ kJ mol}^{-1} \text{ \AA}^{-1}$. Figures c-e show the formation of a satellite droplet following the detachment of the drop from the fiber under the force $F=0.0292 \text{ kJ mol}^{-1} \text{ \AA}^{-1}$ for the atomistic water model and $V_r = 2000$. The droplet contains 17000 SPC/E water molecules and the fiber radius $r_f = 6.4 \text{ \AA}$.

2.3.3 Effect of droplet volume on the minimum detachment force

Figure 15a shows the minimum force (per molecule) required to detach a droplet from a fiber ($r_f = 6.4 \text{ \AA}$) as a function of the reduced volume V_r . The minimum force per molecule of the liquid increases as the droplet volume decreases, in good agreement with the experiments and continuum simulations²⁸ for macroscopic drops conducted using the Surface Evolver code.²⁸ We also notice that the detachment happens after the nanodrop's shape transforms from the symmetric barrel shape to the asymmetric clamshell and the apparent contact angle of the droplet on the fiber approaches $\sim 90^\circ$. At this stage, the circumference of the drop C shows only a weak dependence on the distance from the fiber. Upon further increase of the applied force, the droplet elongates, reaching the neck stage. As the neck narrows, the detachment process can proceed spontaneously even under a weaker force. By using this picture and by balancing the maximal capillary force $f_c \propto C\gamma$ ¹¹⁶ and the weight force acting on the droplet $\rho gV \sim FR^3$,¹¹⁷ where V , ρ , γ are the droplet volume, liquid density, surface tension of the liquid droplet, and R is the characteristic dimension of the drop $R \propto V^{1/3}$, and by assuming C is roughly proportional to R , we can predict the variation of the force needed to detach the droplet with droplet size, $FR^3 \approx \gamma R \rightarrow F \propto 1/R^2 \propto V^{-2/3}$. Based on our estimate, increasing the volume of a droplet V from V_1 to V_2 decreases the minimum detachment force of the droplet by the factor of $\left(\frac{V_1}{V_2}\right)^{2/3}$. In other words, the detachment force obtained for a specific reduced volume can be used to predict the force required to detach droplets of other sizes from the fiber. In Figure 15a, the red curve represents the data produced by scaling the results for $V_r = 250$

in proportion to $V_r^{-2/3}$ for an atomistic system. This scaling prediction is in reasonable agreement with the simulation results.

2.3.4 Minimum detachment force for different fiber radii

We have previously shown that for a constant reduced volume V_r , increasing the fiber radius from the radius r_1 to radius r_2 , decreases the detachment force by a factor of $\left(\frac{r_1}{r_2}\right)^2$.

This prediction also follows directly from our earlier observation that the minimum detachment force (per unit mass) varies as $V^{-2/3}$. If V_r is held constant, $V \sim r_f^3$, and $F \sim r_f^{-2}$.

In Figure 15b, we validate this relation by comparing our simulation results for $r_f = 6.4 \text{ \AA}$ with additional results at the same reduced volume but larger fiber radius $r_f = 12.8 \text{ \AA}$. We rescale the results obtained with the bigger fiber radius by multiplying the force by a factor of $\left(\frac{r_1}{r_2}\right)^2 = \frac{1}{4}$. Figure 15b shows that the scaled results from fiber $r_f = 12.8 \text{ \AA}$ are in excellent agreement with simulation results of the fiber with radius $r_f = 6.4 \text{ \AA}$.

By applying the same concept, we rescaled the macroscopic data from the previous work,²⁸ which is in μm range, to predict the detachment force at length scales of our atomistic model. Figure 15b compares the detachment force obtained from MD simulations of the atomistic system with radius $r_f = 6.4 \text{ \AA}$ with those obtained by scaling the results for larger systems studied by MD coarse-grained simulations and Finite Element simulations,²⁸ with radii $r_f = 12.8 \text{ \AA}$, or $r_f = 107.5 \mu m$, respectively. Figure 15b shows that the proposed relation for the r_f dependence of the detachment force works well over the entire volume

range. This observation gives strong support to the notion that the scaling behavior observed with nano sized models is equally applicable to their macroscopic counterparts.

2.3.5 Effect of adhesion strength on the minimum detachment force

To check how the adhesion strength might affect the detachment force, we considered two different water-fiber interactions $\varepsilon_{co} = 0.625 \text{ kJ mol}^{-1}$ and $\varepsilon_{co} = 0.564 \text{ kJ mol}^{-1}$ corresponding to contact angles on flat surfaces and with insignificant line tension effects, 30° and 50° . Figure 15c shows the detachment force from MD simulations of atomistic systems with radius $r_f = 6.4 \text{ \AA}$, compared to that obtained by scaling the results for larger systems, experiment (detachment of aqueous ferrofluid droplets on the fishing line under magnetic field) and Finite Element simulations²⁸, with fiber radius $r_f = 107.5 \text{ \mu m}$ and contact angles $\theta = 30^\circ$ and 50° . As the fiber is made more hydrophobic, detaching a droplet from the fiber becomes slightly easier, especially for small size droplet. The effect of adhesion strength (contact angle) diminishes with increasing V_r and becomes statistically insignificant for $V_r > 1.25 \times 10^3$.

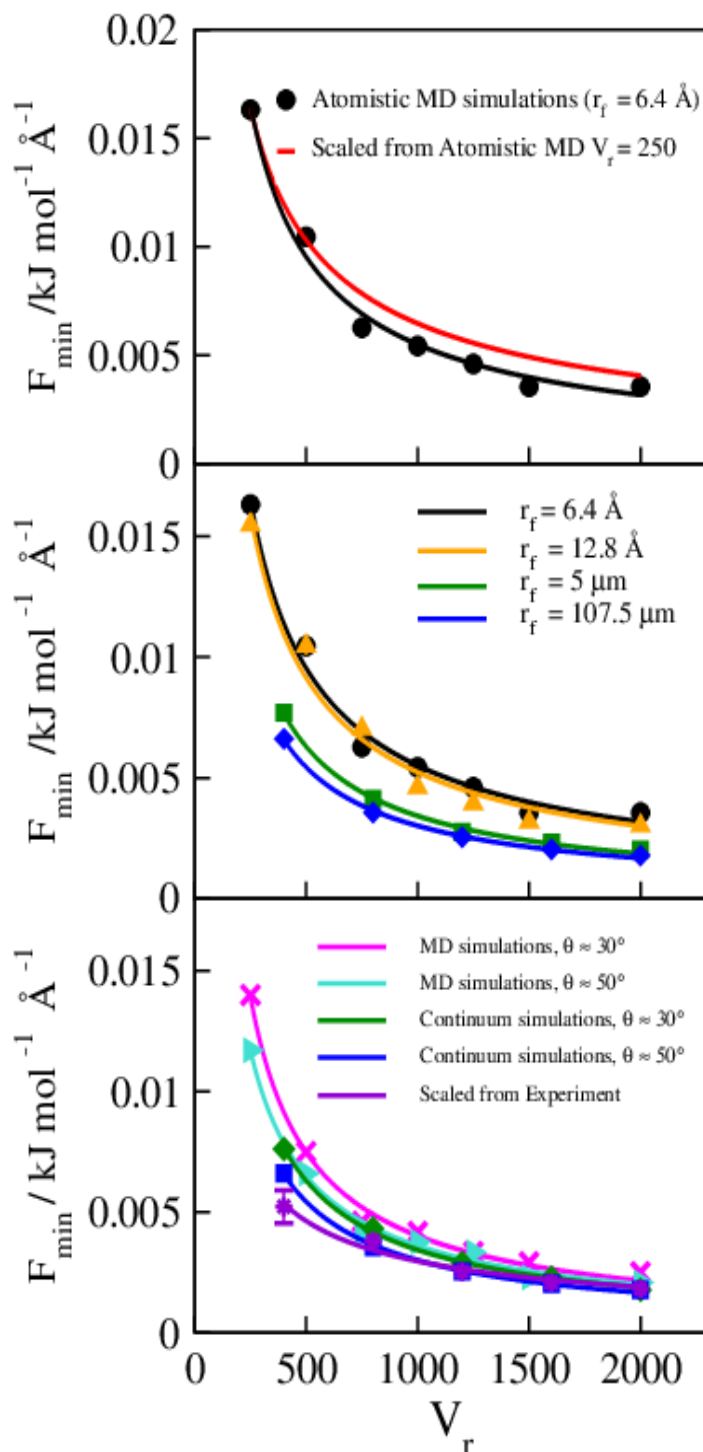


Figure 15: The minimum force required to detach the droplet from a fiber at different reduced volumes. Top: the black curve describes simulation results of the atomistic model with the fiber radius 6.4 Å. The red curve was produced by scaling the result for $V_r = 250$ in proportion to $V_r^{-2/3}$. Middle, black circles: atomistic simulations with the fiber radius $r_f = 6.4 \text{ \AA}$; orange triangles: CG system and fiber radius 12.8 Å, rescaled to $r_f = 6.4 \text{ \AA}$; blue diamonds and green squares: data from the Finite Element simulations with two different fiber radii 5 μm and 107.5 μm¹⁶ rescaled to $r_f = 6.4 \text{ \AA}$. The latter two curves correspond to a bigger contact angle of water on the fiber $\theta \sim 50^\circ$.¹⁶ Bottom: results for fiber-water interaction strengths $\epsilon_{co} = 0.62 \text{ kJmol}^{-1}$ and $\epsilon_{co} = 0.56 \text{ kJmol}^{-1}$. Contact angles of atomistic water on flat surface with the same interactions are $\approx 30^\circ$ and 50° , respectively. The pink “x” and cyan triangles represent the force required to detach a droplet from a fiber with radius 6.4 Å, for an atomistic model system with different water-fiber interactions. The remaining three sets of data (violet, green, and blue) correspond to macroscopic systems with $r_f = 107.5 \text{ \AA}$ μm, rescaled to $r_f = 6.4 \text{ \AA}$. The violet stars describe experimental points¹⁶ and the blue square and green diamonds are from Finite Element simulations with contact angles 30°, 50°, respectively.¹⁶ Error bars are of the same size as the symbols.

2.4 Residual of the droplet on a fiber

In Figure 16, we plot the morphology diagram obtained from the atomistic simulations of water droplet deposited on the fiber with radius $r_f = 6.4 \text{ \AA}$, in terms of the control parameters such as the force and the reduced volume. The red color indicates the minimum force of detachment, and the green color represents the threshold force, beyond which no residue of the droplet remains on the fiber.

According to Figure 16, we can observe three different outcomes in response to the applied force. This diagram is showing the boundaries between the three regimes corresponding to no detachment, partial detachment, or complete detachment of the drop from the fiber. In the first regime, the force is too weak to compete with cohesive forces in the drop or the adhesion between the fiber and the droplet. Thus, the droplet does not detach from the fiber. When the external force is sufficient to overcome the surface tension, the droplet starts to elongate and eventually detaches. At an intermediate stage, the drop stretches slightly and creates a neck. As the neck elongates and narrows, the breakup can happen at varying distances from the fiber. Depending on the strength of the external force and the breakup position of the neck, a small fraction of the droplet can remain on the fiber. If the external force is very strong, it can prevail over the adhesion forces and the droplet detaches as a whole. Figure 16 also shows that the threshold force required for *complete* detachment increases with increasing droplet volume. Therefore, it is harder to detach the bigger droplet entirely from the fiber.

The inset in Figure 16 shows the probability of observing a residue after detachment in our simulations when applying the minimum detachment force. Here, the residue is considered to exist for any nonzero number of water molecules N_r remaining on the fiber. For the small fiber radius $r_f = 6.4 \text{ \AA}$, the probability of seeing the residue increases by increasing the reduced volume and reaches 100% for droplet sizes V_r exceeding $\sim 10^3$.

For a wide range of intermediate force strengths, the average outcome is a partial detachment. Depending on the strength of the external force, a small portion of the droplet can remain on the fiber. When the force is close to the minimum detachment force, the droplet shape transforms from symmetric barrel shape to asymmetric clam-shell conformation before detaching from the fiber. For strong forces, the droplet does not have enough time to transform into the clam-shell configuration completely. This means that the shape relaxation time (τ), of the droplet on the fiber in the presence of external forces exceeds the detachment time of the droplet. In order to find the relaxation time of the droplet, we determined the time correlation functions for the height of the center of mass, $R(t)$:

$$R(t) = \frac{\langle h(t) - h(\infty) \rangle}{\langle h(0) - h(\infty) \rangle}$$

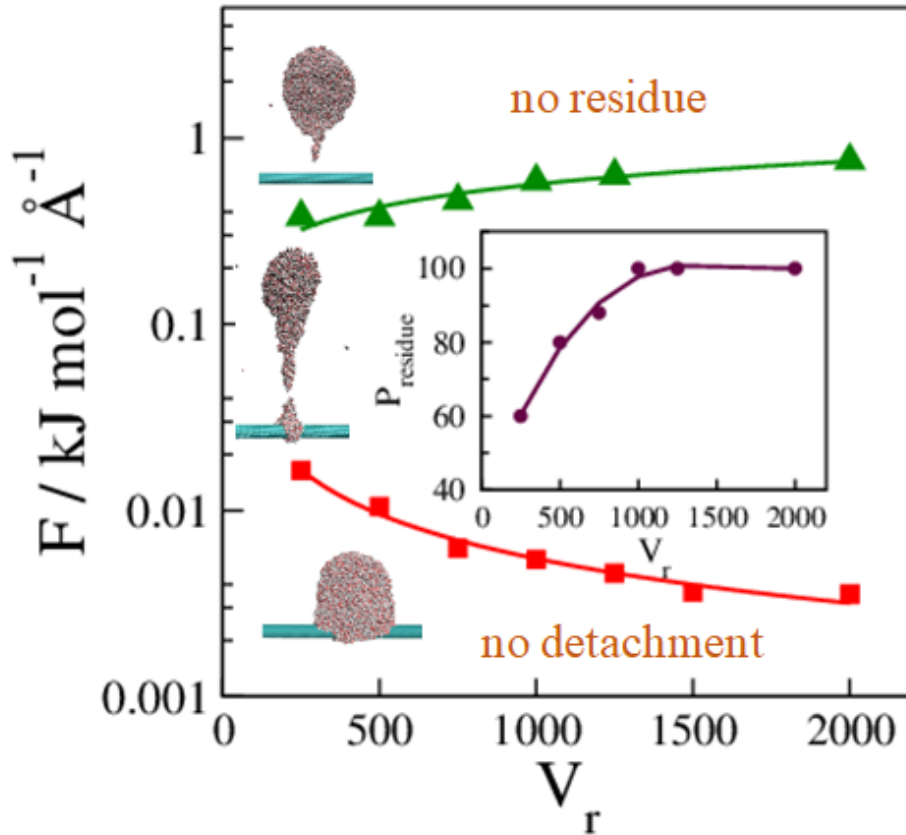


Figure 16: Morphology diagram of nano-sized droplets on a fiber with radius , $r_f = 6.4 \text{ \AA}$ and $\varepsilon_{co} = 0.6639 \text{ kJ mol}^{-1}$, as a function of applied force F and reduced volume of the drop, V_r . The red color indicates the minimum force of detachment and green color indicates the threshold force above which no residue of the droplet remains on the fiber. The number of water molecules varies from 2000 to 17000. The inset shows the probability P_{residue} of observing a residue on the fiber vs reduced volumes when applying the minimum detachment force.

following a change of the applied force acting on the drop. Above, $h(t)$ is the height of the center of mass of the droplet as a function of time. $h(0)$ is the initial height of the center of mass corresponding to the equilibrium shape of the droplet on the fiber under initial force $F=0.0016 \text{ kJ mol}^{-1} \text{ \AA}^{-1}$, and $h(\infty)$ the equilibrium height of the center of mass of

the droplet, under the increased force $F=0.0025 \text{ kJ mol}^{-1}\text{\AA}^{-1}$. Figure 17 illustrates the relaxation of an atomistic droplet on the fiber of radius $r_f = 6.4 \text{ \AA}$ and the reduced volume $V_r = 2000$. Assuming approximately exponential decay, the relaxation time $\tau \approx (0.36 - 0.4) \text{ ns}$, while the detachment time, (t_d), at maximal residue is $t_d \approx (0.135 - 0.185) \text{ ns}$. The inset in Figure 17 shows the detachment time of the droplet as a function of the applied force. At forces significantly exceeding the minimal detachment force, the detachment takes place before the transition to the clam shell shape could be completed and the process results in a bigger residue on the fiber.

MD results for detachment times at applied forces well above the minimal detaching force F_{min} (collected in Figure 18) suggest an empirical scaling of the detachment time with the relative excess in the external force above the minimal detachment value, $t_d \propto \left[\frac{F-F_{min}}{F_{min}} \right]^{\frac{2}{3}}$.

At forces significantly stronger than the minimal detachment force, the detachment takes place before the transition to the clamshell shape could be completed and the process results in a larger residue on the fiber.

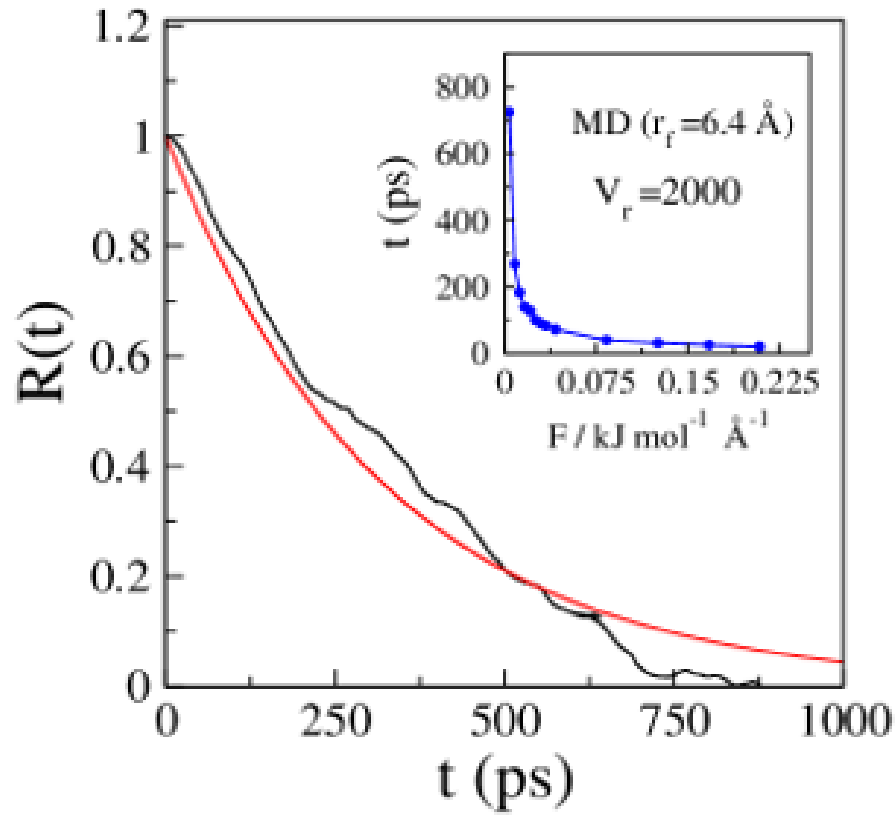


Figure 17: Time correlation function, $R(t)$, of the height of the center of mass of droplet on fiber for an atomistic system with reduced volume $V_r = 2000$ and fiber radius, $r_f = 6.4 \text{ \AA}$. At time close to 1ns, $R(t)$ crosses to the negative value due to inertia. The inset figure shows the detachment time of the droplet as a function of applied force.

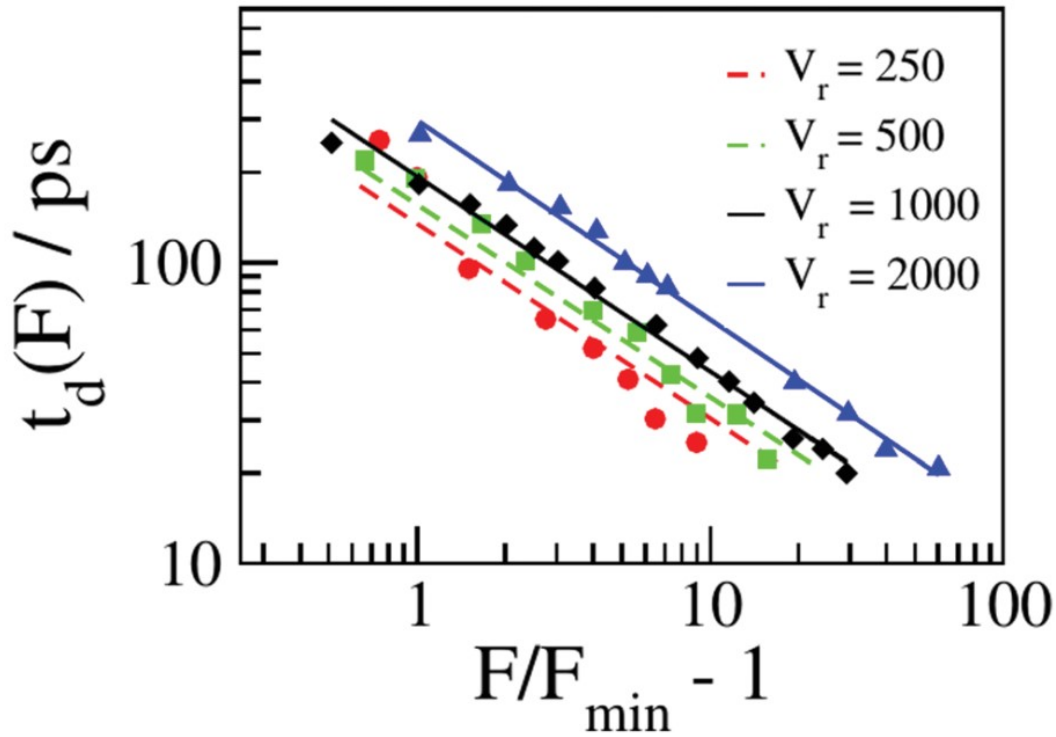


Figure 18: Symbols: MD detachment times of water droplets from the fiber of radius 6.4 Å as functions of the relative excess of applied forces of strengths well above the minimal detachment force F_{\min} (Figure 15a) for the atomistic model of water. Scaling of the form $t_d \propto (F / F_{\min} - 1)^{(2/3)}$ is indicated for all droplet volumes above the smallest size ($V_r \sim 250$) where only approximate compliance is observed. Lines are fitted to the MD data using the fixed slope $-2/3$.

To get a better insight into the water retention after the droplet detachment from the fiber, we compute the average amount of residue on the fiber from atomistic MD simulations under the minimum force of detachment for a range of droplet sizes from 2000 to 17000 water molecules on the fiber with radius $r_f = 6.4 \text{ \AA}$ or 12.8 \AA . We find out that the ratio of the number of retained water molecules, (N_r), to the total number of water droplet, (N_{tot}), never exceeds 10% when the minimum detachment force is applied (Figure 19).

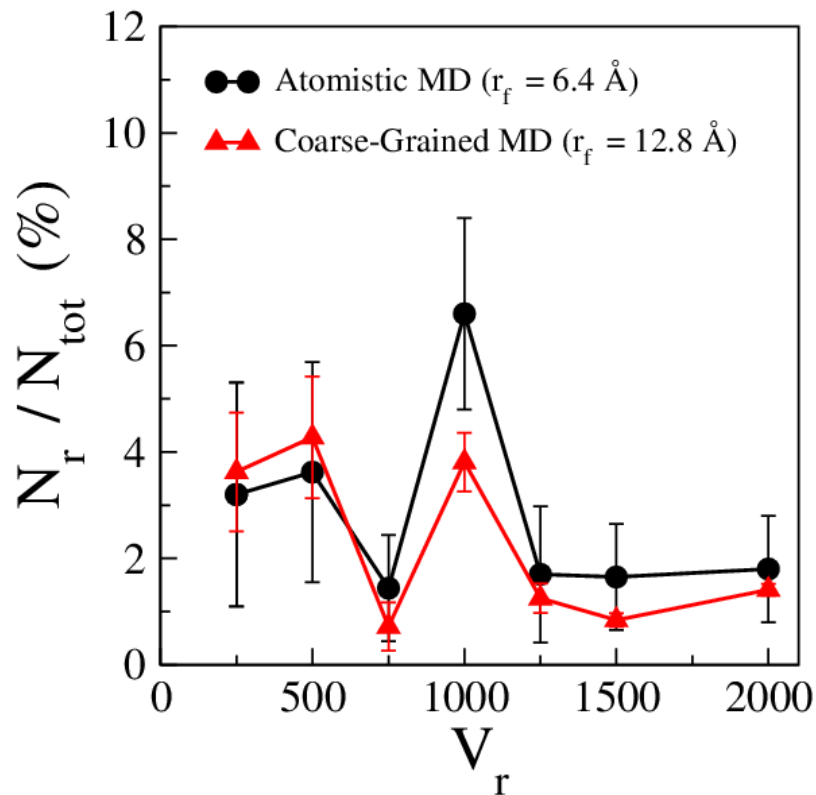


Figure 19: Percentage of the residue of a droplet remaining on the fiber, $r_f = 6.4 \text{ \AA}$ or 12.8 \AA , obtained by applying a minimum detachment force.

We proceed by extending these calculations to stronger forces and determine the average residue size as a function of the applied force and the associated detaching time for a set of

reduced volumes V_r . Our simulations provide the first quantitative insight into the residue dependence on droplet volume and applied force strength.

Figure 20a shows the percentage of the multi-run average residue of a droplet on the fiber for different detachment forces obtained with the atomistic water model. At all droplet sizes, the average residue on the fiber initially increases with the force until it reaches the maximum and then it decreases and eventually vanishes at very strong forces. The maximum amount of residue is never reached by applying the minimum detachment force. As we mentioned earlier, the initial increase of the residue size with the force is due to the fact that, at stronger forces, the droplet does not have enough time to transform entirely from the barrel shape to the clamshell shape (Figure 13e). Therefore, the detachment occurs when the fiber is still wetted over a bigger area than in the clam-shell conformation. It should also be noted that as the droplet size increases, the maximum residue occurs at weaker forces. We also monitored the detachment time for the different reduced volume. As can be seen in Figure 20b, the volume of the residue on the fiber is small or negligible if the detachment is very slow or vary rapid, with the maximal average size obtained at an intermediate detachment time. To the best of our knowledge, this interesting behavior has not been previously reported.

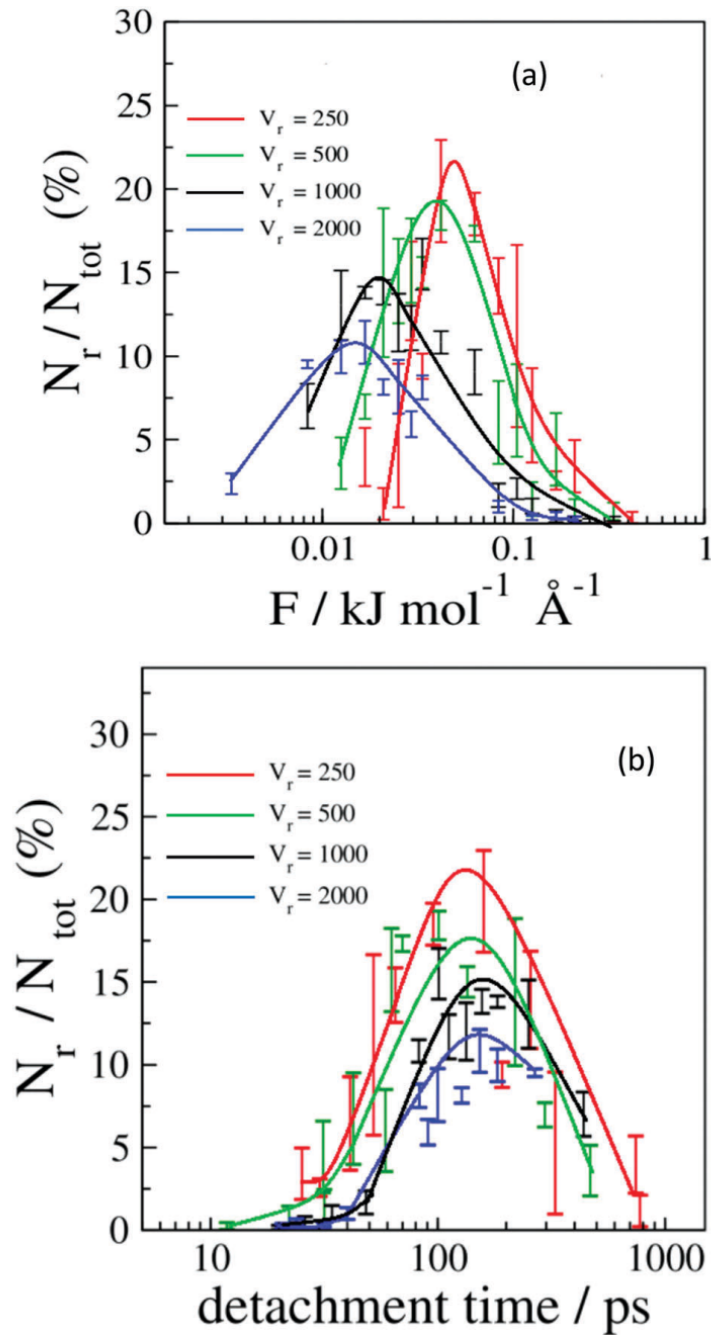


Figure 20: (a) Percentage of the residue of a droplet remaining on the fiber, $r_f = 6.4 \text{Å}$, obtained by applying a range of forces. The curves start at the minimum force of detachment. Error bars are estimated from multiple simulations for respective forces with each system statistically independent from others. (b) Percentage of the residue of the droplet on the fiber versus the detachment time.

To illustrate the dependence of the amount of the remaining water on the detachment force and the size of the droplet, in Figure 21 we plot the number of water molecules N_r in the maximal residue on the fiber versus a total number of water molecules on the droplet (N_{tot}) for different detachment forces. The maximal residue (at system-dependent force strengths F_{max} corresponding to the maxima in Figure 20a increases with the droplet size. The increase of N_r with N_{tot} is, however, sublinear; while the absolute residue increases with the droplet size, the fraction of residual water decreases with N_{tot} .

Figure 22 shows typical breakup configurations of the droplet under detaching forces yielding the maximal residue. The breakup profiles of the droplet at these conditions resemble two cones joined at their apexes (called the double cone profile)¹¹⁸ and lead to approximately symmetric pinch-off. The above shape emerges when the relaxation time of the droplet is longer than the detachment time. The detachment therefore occurs before reaching the clamshell shape. Since the residue approximately corresponds to the volume of the lower cone, $V_{LC} \sim base\ area \times height \sim (R \times r_f) \times R$ (R is the characteristic dimensions of the droplet $\sim V^{1/3}$), we find $V_{LC} \sim R^2 \sim V_{tot}^{2/3}$.

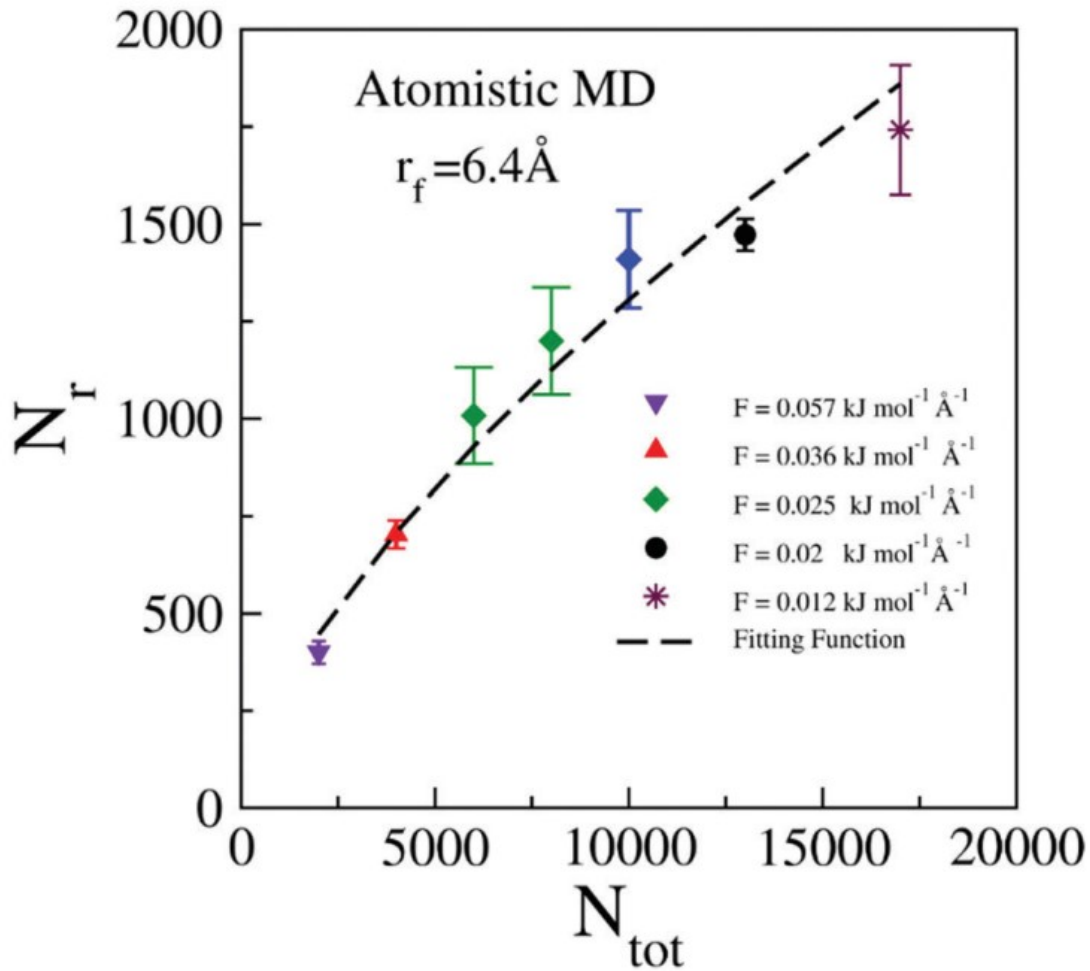


Figure 21: The average number of water molecules remaining on the fiber versus the total number of water molecules at detachment forces producing the maximal residue. The symbols denote the maximum residue on the fiber with radius 6.4 Å at the time of detachment obtained from atomistic MD simulations. The dashed line indicates the fitting function $N_r \propto N_{tot}^{2/3}$ that is predicted by observing that the maximum residue corresponds to the double-cone pinch-off form of the detaching droplet.

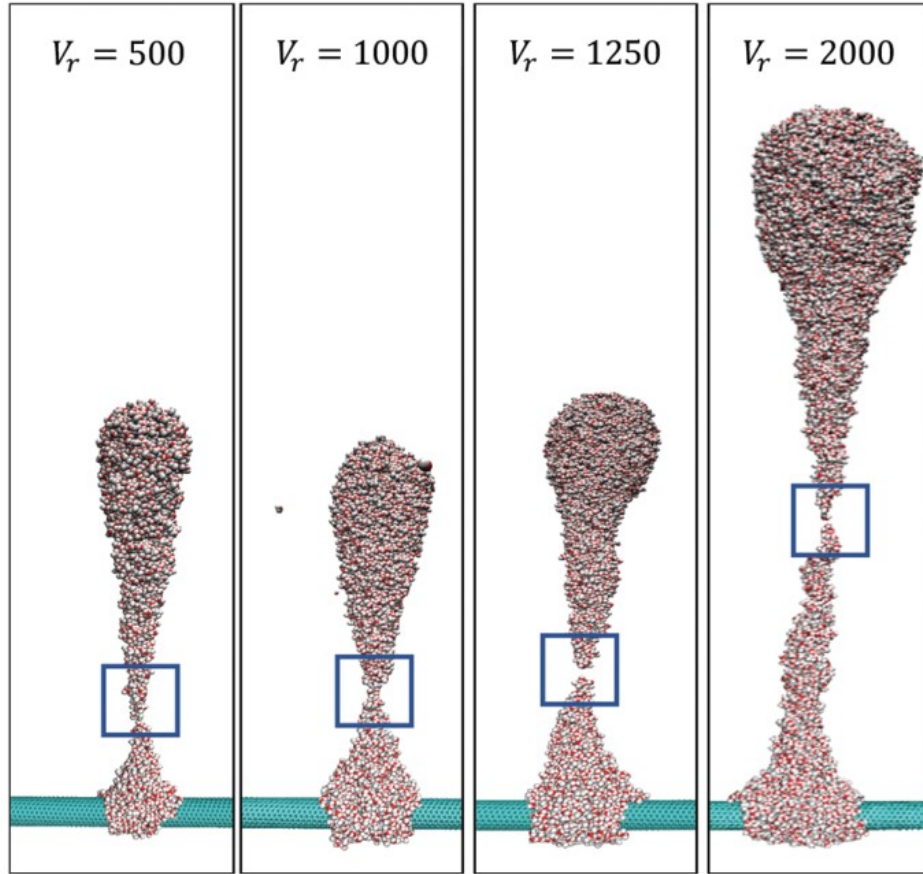


Figure 22: Snapshots of MD trajectories of the droplet at the time of detachment from the fiber for the atomistic model with fiber radius, $r_f = 6.4 \text{ \AA}$, when the residue is maximized. The droplet sizes vary from 4000, 8000, 10000, 17000 SPC/E water molecules.

Figure 21 confirms that our simulation results for the maximum residue of water after detachment from fiber follow the above prediction. Using the relationship $V_{res} \sim V_{tot}^{2/3}$ can help us to predict the volume of the residue on a fiber for different droplet volumes. Figure

23 shows the force that produces the maximal residue F_{max} on the fiber ($r_f = 6.4 \text{ \AA}$) versus reduced volume, V_r . F_{max} increases with decreasing the reduced volume V_r . The dashed line indicates the fitting function of the F_{max} versus V_r with the form $F_{max} = const \times V^{2/3}$. Our simulation results indicate that the force of the maximum residue varies according to the relation $F_{max} \sim V^{2/3}$, in analogy to the minimum detachment force discussed in Section 2.3.2. While our analysis concerns detachment events induced by gravity-like body forces, other types of perturbation, notably shear forces, can be of comparable practical importance and will be considered in planned future studies.

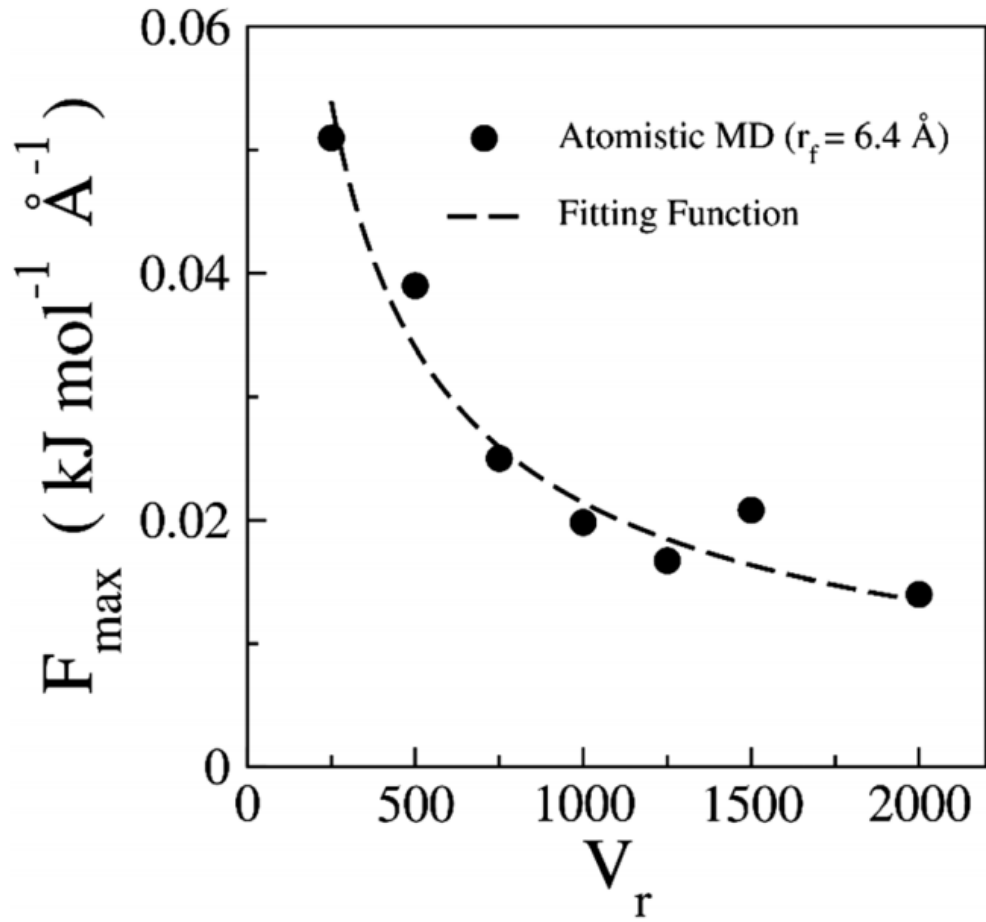


Figure 23: The force producing the biggest average residue, F_{\max} on the fiber as a function of the reduced volume. The dashed curve indicates the fitting function $V_r^{-2/3}$. The droplet sizes in atomistic simulations vary from 2000 to 17 000 SPC/E water molecules.

2.5 Conclusion

We have presented a comprehensive study aimed at predicting the external force required to detach the droplet from a smooth fiber through a combination of atomistic and coarse-grained Molecular Dynamics (MD) simulations. We have identified three regimes corresponding to no detachment, partial detachment, or complete detachment upon applying the external force perpendicular to the fiber. The outcome critically depends on the strength of the applied force, as demonstrated in the morphology diagram in Figure 16. Our results show that the minimum force (per molecule) capable of detaching a droplet from the fiber decreases with increasing volume of the droplet, in good agreement with experiments and continuum simulations for macroscopic droplets. The results for the detachment force obtained for a system with droplet volume V_1 can be used to predict the detachment force for other droplet sizes V_2 according to the scaling relation $F_2 \cong F_1 \left(\frac{V_1}{V_2}\right)^{2/3}$.

We also computed the amount of the residue on the fiber after detachment for different droplet sizes and external forces. We observed that as the droplet size increases, a larger residue remains on the fiber, however, the fraction of the residual liquid expressed relative to the size of the droplet decreases with its size. The magnitude of the residue shows a nonmonotonic dependence on the applied force and concomitant detachment rate. While the entire droplet can be detached at sufficiently strong forces, and an almost complete detachment takes place at forces slightly above the minimal detaching force, we observe maximal residues at an intermediate force a few times stronger than the minimal detaching

force. Within a broad range of system sizes we considered, the ratio of the two forces remains essentially invariant with respect to the volume of the drop. Another useful insight of this study is the possible prediction of the maximal residue size from the prevalent geometry in the pinch-off state. By considering the breakup profile of the splitting droplet upon detachment, we predicted the maximum residue on the fiber to increase with the droplet volume V sub-linearly, in proportion to the $V^{2/3}$ and we confirm this dependence in explicit calculations. Our molecular simulations⁶² offer direct guidance for the control of liquid retention through external force and can provide the necessary input toward the development of methodologies for time dependent continuum-level simulations at macroscopic scales relevant to industrial problems.

2.6 Pathway of droplet removal from a hydrophilic surface

The study of liquid droplet adhering to flat solid surfaces has received considerable attention due to its importance in many different engineering applications, such as filtration, spray coating, and oil recovery, liquid water removal in PEM (proton exchange membrane or polymer electrolyte membrane) fuel cells, and Resuspension of an aerosol from solid surfaces.^{13, 119-126}

From the microscopic point of view, the detachment can occur as a consequence of the competing effects between the external force and the adhesion between the liquid and the solid surface. When the external force, applied in the normal direction, is barely sufficient to remove the drop from the surface, the removal force is essentially equal to the strength of adhesion. Because of the roughness and nonuniformity of solid surfaces, some areas of the droplet base may have better contact and hence stronger adhesion to the surface than others. Therefore, not all of the drops detach at an identical external force. The range of the observed detachment forces is narrower for smoother surfaces. If the substrate surface is smooth enough, experiments indicate the adhesive forces are essentially proportional to the diameter of the droplet.

Tremendous effort, both experimental and theoretical, has been spent on studying the fundamental mechanisms of the droplet detachment from the smooth surface.^{13, 119-123}

According to these studies, a portion of the droplet may sometimes detach even when the external force is too weak to detach the entire droplet.

In the present work, we focus on understanding how the adhesion of the droplet on a hydrophilic surface affects the detachment behavior and how the applied force can change the residue of droplet on the flat surface. We analyze the process using atomistic molecular dynamic (MD) simulations. While valid insights could in principle follow from experiment and continuum simulations, our approach relies directly on input atomic and molecular forces rather than on experimental data for presumably invariant and uniform macroscopic properties such as the interfacial tensions, viscosity, drop's perimeter friction, and possibly line tension effects. We address the fundamental questions about the droplet size-dependence of the minimal force capable of detaching a droplet from the surface, and the effects of droplet size and applied force on the amount of the liquid residue left on the surface after the detachment. We perform multiple MD simulations for water droplets on a smooth hydrophilic surface at varied system sizes and applied forces. Our modelling studies of the droplet breakup show the amount of residual water to be maximal near the minimum detachment force strengths whereas a complete or near-complete detachment of the droplet can be achieved with very strong force. Because of its fundamental appeal and importance for applications, we hope the work will inspire experimental investigations and theoretical analyses of liquid retention and its control through varied stimuli for droplet detachment from the surface.

2.6.1 Methodology

2.6.1.1 Force Fields

The surface was built with Visual Molecular Dynamic (VMD) package. It consists of a rigid hexagonal graphene surface comprised of 5600 Lennard Jones (LJ) carbon atoms.⁶
⁹⁴ To reduce finite size effects, the surface is periodically replicated along the XY-direction. We use the rigid extended simple point charge (SPC/E) potential^{95,96} to model the atomistic water droplet. The use of this force field is motivated by our recent dynamic studies of bulk and confined water.¹⁰¹ As detailed in Section 2.2.1, this potential consists of a Coulomb potential acting between partial point charges on oxygen ($-0.8476e_0$) and hydrogen ($0.4238e_0$) atoms and an O–H distance 1 Å and the H–O–H angle at 109.471. Further, oxygen atoms also interact via Lennard Jones potential (LJ). In all our atomistic simulations the water–surface interaction is based on the Lennard-Jones potential between the SPC/E water molecules and the surface. The LJ strength was characterized by $\epsilon_{co} = 0.57 \text{ kJ mol}^{-1}$ with cutoff radius 12 Å.

2.6.2 Simulation details

The simulations start by placing a water droplet on a cubic lattice above the surface positioned along the z axis of a cubic simulation box of size 300 Å. During the equilibration, the droplet on the surface reaches the symmetric equilibrium shape. We considered five sizes of water droplets composed of 4×10^3 , 6×10^3 , 8×10^3 , 10×10^3 , 13×10^3 water molecules on top of a rigid graphene surface.

Depending on the size of the droplet, the total length of the simulation run varied from 2.5 to 5 ns (Figure 24).

All MD simulations are carried out by using the LAMMPS package¹¹⁰ in the NVT ensemble. The temperature is kept constant at 300 K using the Nose–Hoover thermostat¹¹¹ with a relaxation time of 0.2 ps. Verlet integration is used with time step 1 fs for atomistic water. Long range Coulombic forces are treated using PPPM Ewald summation with 10^{-5} accuracy and periodic boundary conditions are used in all dimensions.

The forcible detachment of the droplet from the hydrophilic surface was studied by using Non-Equilibrium Molecular Dynamics (NEMD). After reaching the equilibrium state, a constant force was applied to every molecule in the droplet in a direction perpendicular to the surface and remained constant during the simulation. Depending on the force strength, the time necessary to observe the detachment varied from 50 ps to 2 ns for the strong and weak forces, respectively.

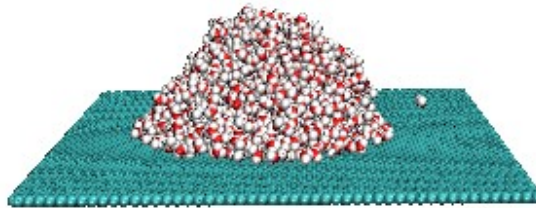


Figure 24: Snapshot of an equilibrium shape of aqueous droplet atop a model graphene surface.

2.6.3 Results and discussion

2.6.3.1 Droplet behavior in the presence of an external force

Figure 25 shows consecutive snapshots from MD trajectories of the atomistic droplet in the presence of external force. The force is applied in the direction perpendicular to the surface. As illustrated in Figure 25 top, when the force per molecule becomes strong enough, the droplet eventually detaches from the surface, but a certain percentage of droplet mass can remain on the surface.

When applying a strong force on the droplet, the droplet can detach as a whole (Figure 25 bottom).

To understand the breakup mechanism and determine the amount of residue of a nanoscale liquid droplet on the surface, we perform multiple independent simulation runs. We observed that by applying the same force to the droplet, the amount of remaining water on the surface alters from one simulation run to another. The variation of the residue size takes place because when a droplet stretches, it creates a narrow neck whose breakup position is subject to large fluctuations. We also observed the formation of a small satellite droplet emerging upon the breakup of the drop. In this case, the satellite droplet separated from the droplet after it detached from the surface.

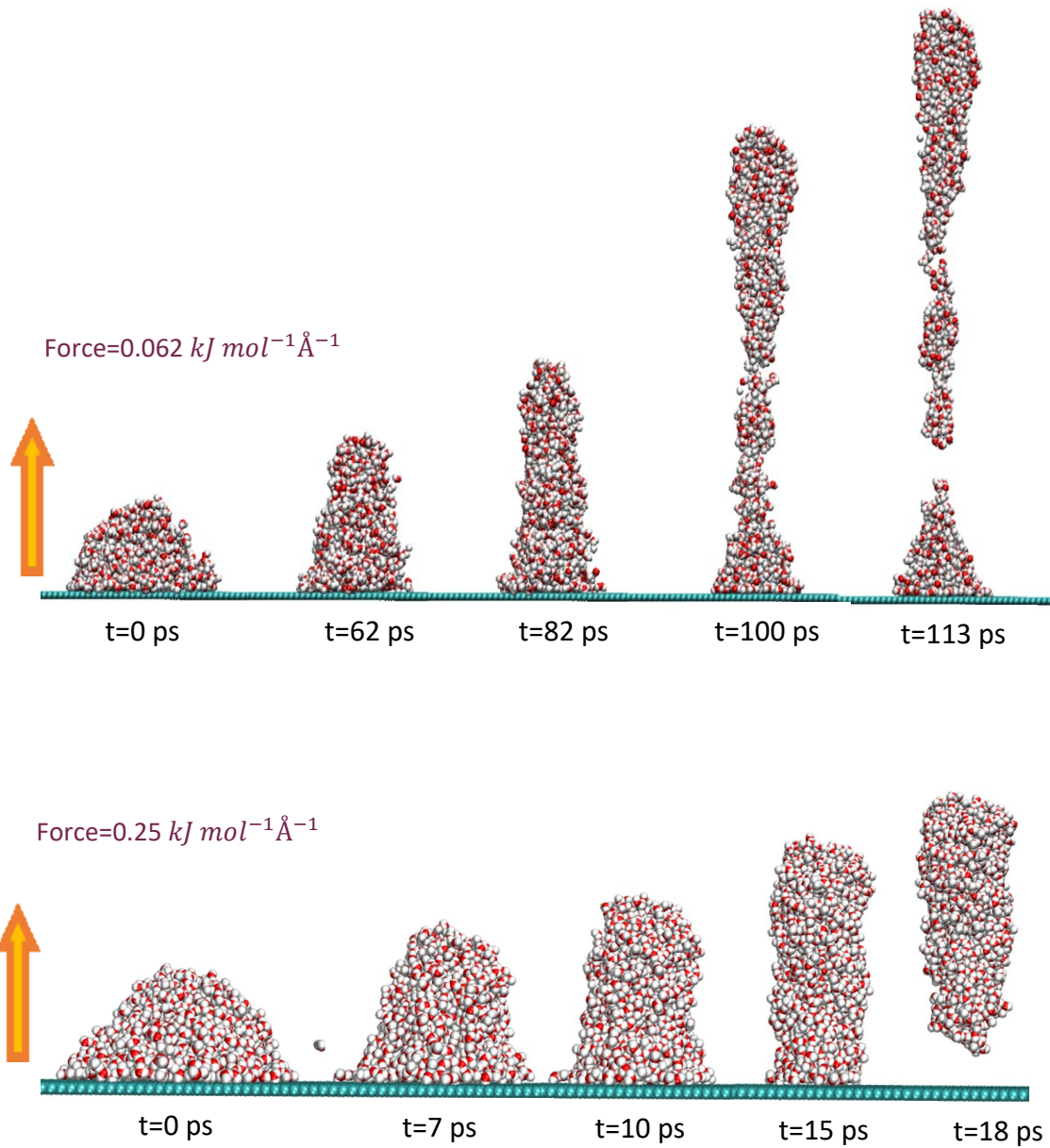


Figure 25: Snapshots from MD trajectories of the droplet detachment from surface for the atomistic model at external forces $F = 0.062$ or $0.25 \text{ kJ mol}^{-1} \text{ \AA}^{-1}$ for a drop comprised of 4000 SPC/E water molecules on graphene surface.

2.6.3.2 Effect of droplet volume on the minimum detachment force

Figure 26 shows the minimum force (per molecule) required to detach a droplet from a surface as a function of droplet sizes. As can be seen in here, the minimum force per molecule of the liquid increases as the droplet volume decreases. We also notice that the detachment happens after the apparent contact angle of the droplet on the surface approaches $\sim 90^\circ$. At this stage, the circumference of the drop C shows only a weak dependence on the distance from the surface. Upon further increase of the applied force, the droplet elongates, reaching the neck stage. The data in Figure 26 confirm the minimal detaching force dependence on the droplet size $F_{\min} \propto N^{-2/3}$. The rationale for this

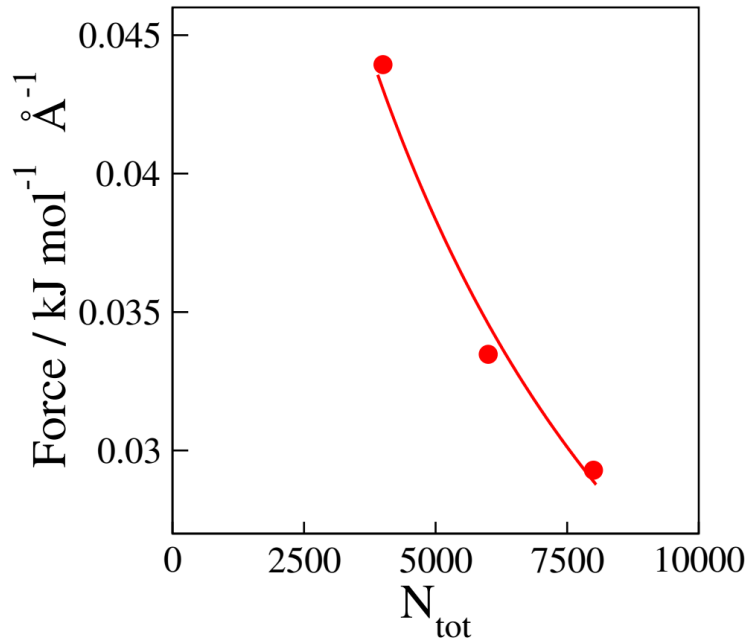


Figure 26: Minimum force required to detach the droplet from a surface for different droplet sizes.

dependence is identical as discussed with the droplet detachment from the fiber. When the

surface tension force passes through its maximum value, proportional to the droplet circumference, it has to be at least balanced by the detaching force, which is proportional to the droplet mass, *i.e.* $\gamma R \propto F_{min} R^3$ or $F_{min} \propto R^{-2} \propto N^{-2/3}$. Once the neck begins to narrow, the detachment process can proceed spontaneously even under a weaker force.

2.6.3.3 Effect of adhesion strength on minimum detachment force

In order to understand how the adhesion strength might affect the detachment force, we considered four different water-surface interactions from $\epsilon_{co} = 0.2 \text{ kJ mol}^{-1}$ to $\epsilon_{co} = 0.6 \text{ kJ mol}^{-1}$. Figure 27 shows the detachment force from MD simulations of 4000 water molecules for different water-surface interactions as the surface is made more hydrophobic, detaching a droplet from the surface becomes slightly easier. In Figure 28, we also plot the minimum detachment force as a function of contact angle. The linear dependence of the force on the adhesion strength (Figure 28) is in good agreement with experimental observations.^{116, 127}

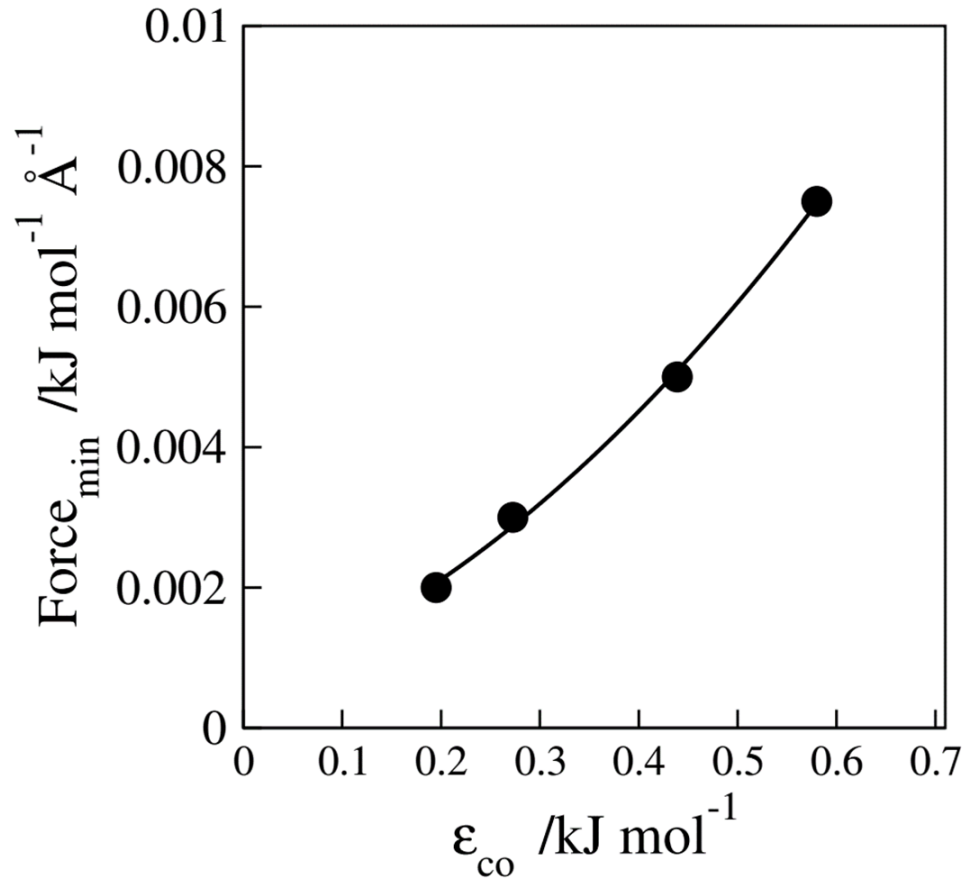


Figure 27: Minimum force required to detach the droplet with 4000 water molecules from a surface for different water-carbon, ϵ_{co} , interactions.

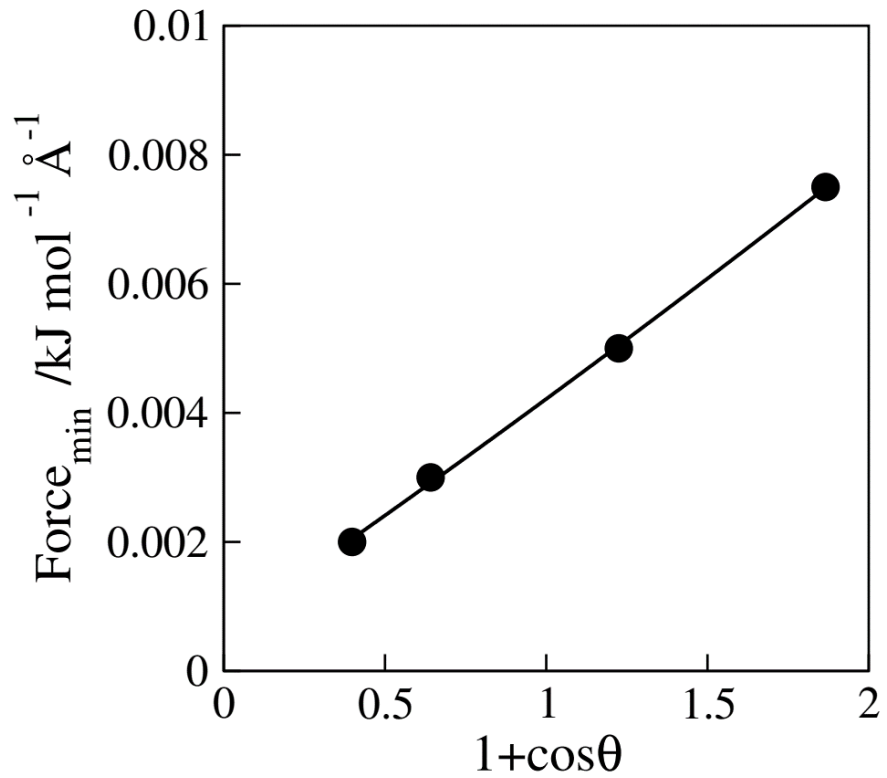


Figure 28: Minimum force required to detach the droplet with 4000 water molecules from a surface for different contact angles reveal a linear increase with the liquid/solid adhesion strength $\propto 1 + \cos\theta$

2.6.3.4 Residual of droplet on the surface

Figure 29 shows the percentage of the residue of a droplet on the surface for different detachment forces obtained with the atomistic water model. Unlike the drop detachment from a fiber, where the residue showed a pronounced maximum at intermediate force strengths, the residue on the planar surface shows a simpler, monotonic or nearly monotonic dependence on the detaching force. The highly scattered data for the average residue size indicate only a weak initial dependence on the force with the biggest residue observed either at the minimal detaching force or only slightly thereafter. The existence of at most a weak maximum remains unclear in view of the limited amount of strongly fluctuating data. A monotonic decrease of the residue size is universally observed beyond the detaching force strengths in excess of $\sim 20\%$ of the minimal detachment value. If not identical, the maximal residue is always close to the value obtained by applying the minimum detachment force. As the droplet size increases, the maximum residue therefore occurs at weaker forces.

We also monitored the detachment *time* for different reduced volumes. The volume of the residue on the surface is small or negligible if the detachment is very rapid, with the maximal average size obtained at the longest detachment times. To the best of our knowledge, this interesting behavior has not been previously reported. Figure 30 also shows the detachment time of the droplet as a function of the applied force.

Figure 31 shows contact area of the droplet with the surface exactly before the detachment for different detaching forces. As can be seen here, the contact area of droplet with the surface is a circle with nearly invariant X and Y dimensions over nearly the entire range of detaching forces. By monitoring the structure of the hydration layer at the drop's base at the time of the detachment, for a very strong applied force, we observe an empty spot at the middle of the base. This behavior is attributed to stronger cohesion forces causing faster detachment of the molecules in the region near the center of the droplet compared to weaker-coordinated molecules at the droplet boundaries.

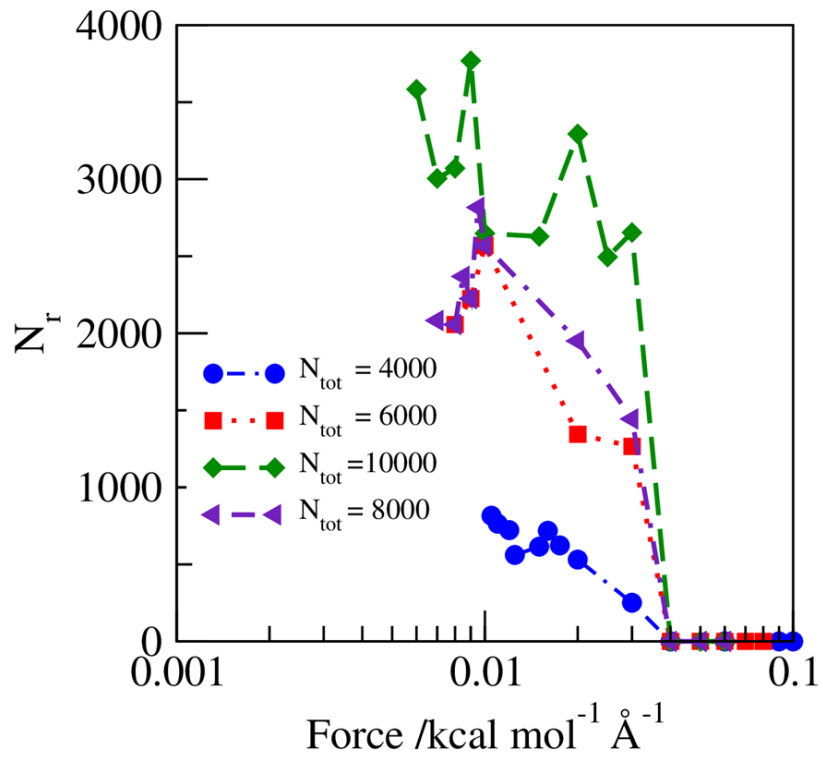


Figure 29: Average residue of a droplet remaining on the surface, (the number of retained water molecules, (N_r), to the total number of molecules in the droplet, (N_{tot}), obtained by applying a range of forces. The lines start at the minimum force of detachment.

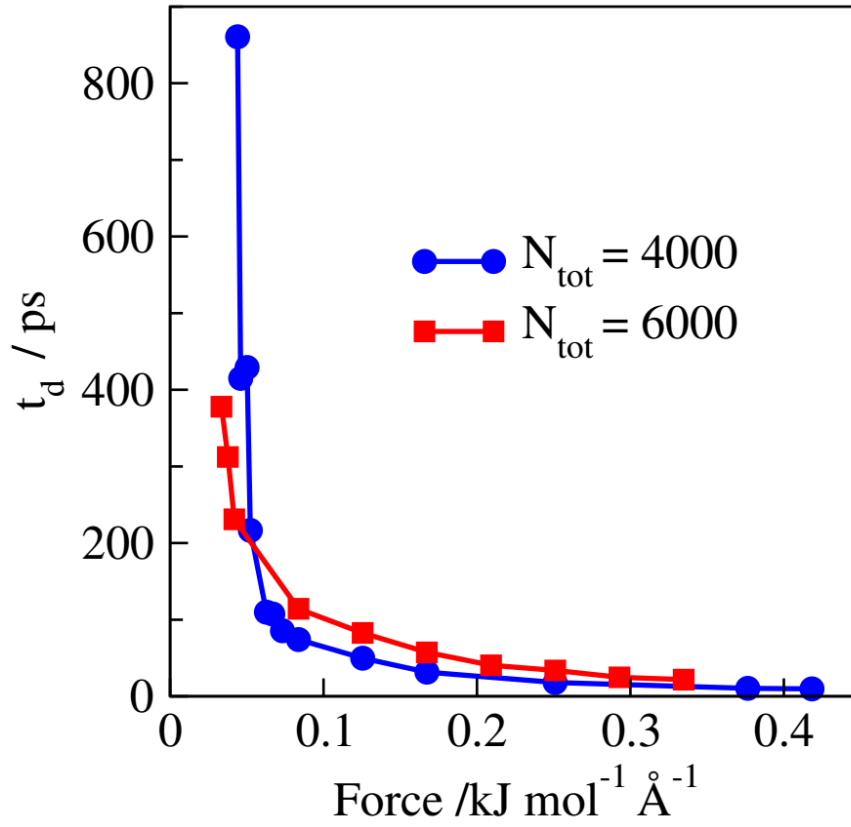


Figure 30: Detachment time of the droplet as a function of applied force. The red and blue lines are guide lines to the simulated data.

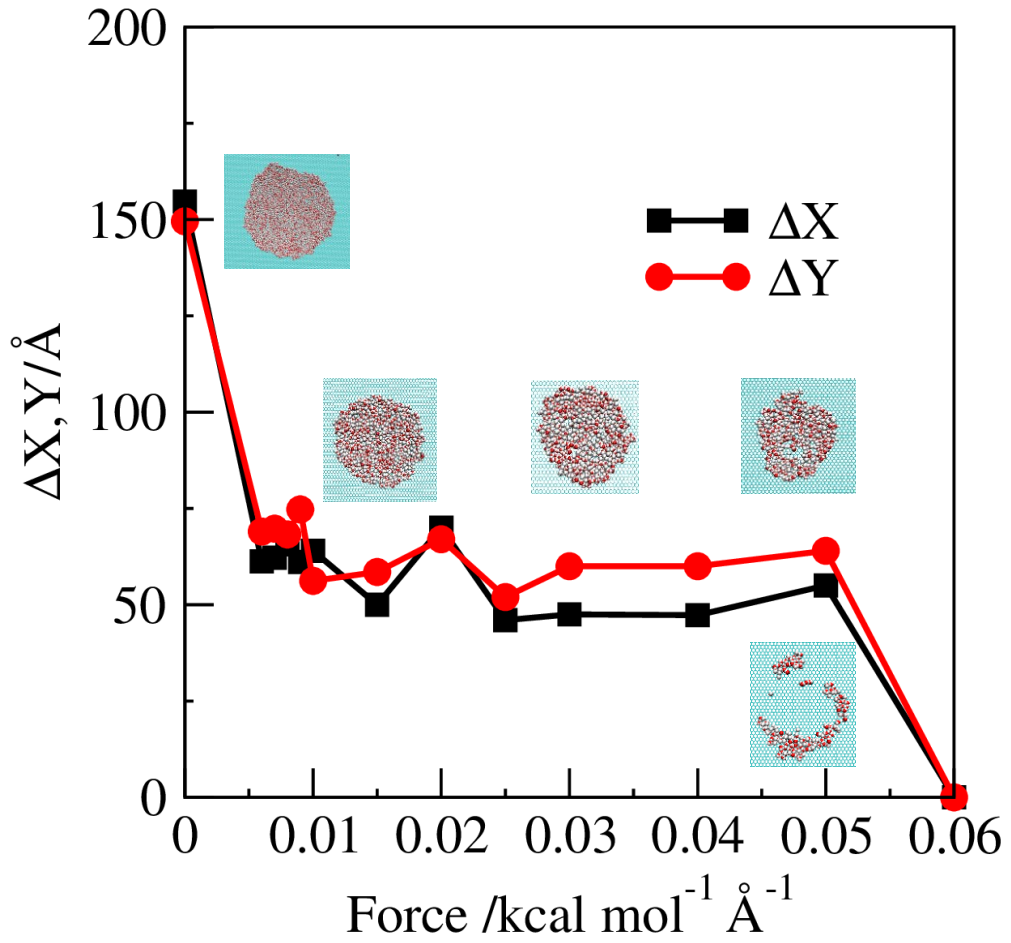


Figure 31: Contact area of droplet on the surface the moment before the detachment vs different forces

2.6.4 Conclusion

We have presented a comprehensive study aimed at predicting the external force required to detach the droplet from a graphene surface by Molecular Dynamics (MD) simulations. We have identified three regimes corresponding to no detachment, partial detachment, or complete detachment upon applying the external force perpendicular to the surface. The outcome critically depends on the strength of the applied force. Our results show that the minimum force (per molecule) capable of detaching a droplet from the surface decreases with increasing volume of the droplet V and weakening the water-surface interactions (increasing contact angle θ) according to the approximate relation $F_{min} \propto V^{-\frac{2}{3}}(1 + \cos\theta)$.

We also computed the amount of residue on the surface after detachment for different forces and different water-carbon interactions. We observed that as the droplet size increases, a bigger residue remains on the surface. We found out that the maximum amount of residue can be observed by applying the minimum force of detachment. This behavior is distinct from our findings for droplet detachment from the curved surface observed in experiments and Molecular Dynamics simulations conducted on water droplet on a fiber.

Our molecular simulations offer direct guidance for the control of liquid retention through external force and can provide the necessary input toward the development of methodologies for time dependent continuum-level simulations at macroscopic scales relevant to industrial problems.

Chapter 3: Water adhesion on conducting graphene

So far, contact angle simulations of water on graphene have been performed by ignoring the material's conductivity. In this project, we improved the graphene force field by adding the conductor properties using the fluctuating-charge technique of Constant Potential Molecular Dynamics (CPMD)^{39, 40}. The fluctuating carbon atom charges of the CPMD model shield the in-plane components of the electric field associated with the structural fluctuations^{128, 129} in adjacent water. As a result of graphene polarization, we observe a qualitative change in correlations among water molecules located at the opposite sides of graphene sheet and enhanced propensity to wetting. We evaluated the wettability by measuring the contact angle of cylindrical water drops on a conducting graphene sheet. We found that the contact angle of a water droplet on a graphene sheet submerged in water is lower than in the absence of water under graphene. In other words, water-graphene adhesion is stronger when graphene is wetted from both sides. The effect is enhanced when we incorporate graphene conductivity. The greater reduction in the contact angle on a submerged sheet is associated with the indirect, graphene-mediated attraction between the water partial charges of equal sign bridged by the induced (image) charges on the electrically polarized graphene. The mechanism is important for the basic understanding of hydration of thin conducting materials.

Parallel calculations for a nonpolar liquid (diiodomethane) confirm that dispersion forces alone result in a moderate “wetting transparency”⁸⁴, however, only two-side wetting by polar solvents proves sensitive to the inclusion of material's conductivity. The effect is of

potential importance for *in silico* predictions of graphene wettability by water to optimize applications from sensors to porous electrodes, fuel cell membranes, and water filtration. The conductor properties can also play a role in hydrophobic interactions among dispersed graphitic nanoparticles¹³⁰, which are often used as showcase systems in modeling¹³¹⁻¹³⁴ nanoparticle interactions in water.

3.1.1 Models and methods

3.1.1.1 Force fields

The nonconducting model surface consists of a single layer of 5600 charge-free carbon atoms on graphene lattice, interacting with water via the Lennard-Jones (LJ) potential^{6, 94}. The conductor behavior of graphene is captured by the addition of fluctuating Gaussian charges on carbon atoms as outlined in the Discussion section. Graphene atom positions are held fixed through the entire simulation. We mitigate finite size effects by periodically replicating the surface in the lateral (xy) directions. The same graphene surface is used in simulations of aqueous and diiodomethane droplets. Following the preceding work⁶, we described water interactions by the extended simple point charge potential (SPC/E)^{95, 96} which has been known to capture the essential interfacial and dielectric properties of liquid water. The use of this force field is motivated by our recent dynamic studies of bulk and confined water^{62, 92, 94, 97-101}. The potential consists of a Coulomb potential acting between partial point charges on oxygen ($-0.8476 e_0$) and hydrogen ($0.4238 e_0$) atoms with O-H distance 1 \AA and H-O-H angle at 109.47° . The oxygen atoms also interact *via* LJ potential with $\epsilon_{\text{OO}}=0.651 \text{ kJ mol}^{-1}$ and $\sigma_{\text{OO}}=3.166 \text{ \AA}$. The LJ interaction between the SPC/E water

molecules and carbon atoms on graphene is characterized by ε_{co} values from 0.19 to 0.51 $kJ mol^{-1}$ and we use a smooth LJ cutoff at 12Å. The carbon atom LJ diameter $\sigma_{cc} = 3.214 \text{ \AA}$ leads to the water-carbon contact distance $\sigma_{co} = 3.19 \text{ \AA}$.

The non-polar droplet is comprised of 600 diiodomethane, CH_2I_2 , molecules with the CH_2 group modeled using the united atom representation. The united atom CH_2 group carries a charge $0.022e_0$ and each of the explicit I atoms has a point charge $-0.011e_0$. The I- CH_2 bond length is 2.21 Å and the I- CH_2 -I bond angle is 116.6°. We use the LJ potentials corresponding to $\varepsilon_{CH_2} = 0.4105 kJ mol^{-1}$, $\varepsilon_I = 3.5 kJ mol^{-1}$, $\sigma_{CH_2} = 4.07 \text{ \AA}$, $\sigma_I = 3.849 \text{ \AA}$ ^{135, 136} with the Lorentz-Berthelot mixing rules and the LJ cutoff distance of 12 Å.

3.1.1.2 Molecular dynamics

In the absence of material's conductivity, the simulations were performed using the large-scale atomic molecular massively parallel simulator package (LAMMPS)¹¹⁰. The temperature was held constant at 300K using the Nose-Hoover thermostat¹¹¹ with a relaxation time of 0.2ps. Verlet integration was used with time step 2fs. The total length of a typical run was 3ns. Long-range electrostatic interactions were computed using the particle-particle-particle-mesh (PPPM) solver, with 10^{-5} accuracy. The slab correction of Yeh and Berkowitz¹³⁷ was added to the Ewald summation to account for the two-dimensional periodicity of our system. The computations for conducting graphene were performed using an adaptation⁹² of the Constant Potential MD (CPMD)⁴⁰ code designed for simulations of two-electrode systems with a preset interelectrode potential difference.

The lateral periodicity was enforced by rigorous two-dimensional Ewald summation⁴⁰. To enable the use of the original CPMD code designed to control the difference between separate conducting objects, we treated the model graphene plate as a pair of distinct ‘electrodes’ at identical potential by assigning a vanishing V_j^0 to all carbon atoms j (denoted by different colors in Fig. 1d).

3.1.1.3 Simulation details

The simulations start by placing a water droplet on a rectangular lattice containing $\sim 6.4 \times 10^3$ water molecules on the graphene surface. The surface of size $123\text{\AA} \times 119\text{\AA}$ coincides with the (x,y) plane. The initial drop has a quadratic cross-section in (x,z) plane and extends along the entire surface width along the x direction. During the equilibration, the droplet acquires a cylindrical shape illustrated in Figure 32. Our choice to employ cylindrical rather than hemispherical drop has been motivated by two reasons. The cylindrical droplet avoids the curvature of the three-phase contact line, which leads to considerable line tension effects with hemispherical nanodroplets¹³⁸. An additional advantage of the semi-infinite cylindrical geometry is the optimization of parallelized computation. The improved computational efficiency permits simulation of bigger cylindrical drops compared to calculations in the hemispherical drop geometry, improving the statistics of contact angle calculation.

All MD simulations were initialized by using the LAMMPS package¹¹⁰. Since LAMMPS is orders of magnitude faster than CPMD code^{40,92}, it enabled an efficient pre-equilibration before running the CPMD simulations. Despite limitations, these well parallelized

packages and advanced computational methods make the simulation process much faster than developing our own codes.¹³⁹⁻¹⁴¹ While we performed NVT molecular dynamics simulations, the system maintained a droplet-vapor equilibrium with pressure fluctuating around the vapor pressure of the liquid. The two types of systems we considered comprised a cylindrical drop on the suspended model graphene surface or the surface supported by a uniform liquid of slab thickness around 13.1 Å which contains $\sim 6.9 \times 10^3$ water molecules or 2000 diiodomethanes. The above width has been demonstrated⁶ sufficient to secure the convergence of the droplet properties atop the graphene layer with respect to the dimensions of the supporting liquid slab. In order to keep the slab thickness uniform, below the slab we introduced an implicit wall interacting with the liquid molecules through a harmonic repulsion. A second wall is also placed at the top boundary of the simulation box to prevent the escape of vapor water molecules along the non-periodic Z direction. The details of auxiliary walls placement and the repulsive potential bear no effect on the calculated wetting behavior on graphene.

3.1.1.4 Contact angle measurement

To establish a direct connection with experiments^{66, 67, 75, 79}, we determine the microscopic analogue of the droplet contact angle. We use a technique¹⁰⁰ similar to that presented by de Ruijter *et al.*¹⁴² that characterizes the dynamics of droplet spreading by calculating the dynamic contact angle for each configuration. We divide the hemicylindrical drop to three slices to remove the possible effect due to long-range triple line fluctuation. The contour of each slice is calculated through a square binning of the local density of water on the yz

plane with a 2Å resolution. The dividing surface corresponds to the isodensity plane with half the density of the droplet core. The contact angle is determined from the circular fit of the drop contour¹⁴³. Because of the known droplet distortion within a few molecular diameters from the solid surface, we fit only the contour above the heights characterized by detectable liquid/solid density profile oscillations^{142, 144}. We adopt the empirical threshold height at half the oscillation period above the second density peak. In view of worsened statistics near the top of the drop, we determine the drop contour from the computed density distributions within ~10 Å thick midsection of the drop, parallel to the X-direction and centered with respect to the drop center of mass¹⁰⁰. The contact angle is determined at the cross-section of the contour and the reference contact plane at an oxygen radius below the first liquid density peak.

3.2 Results and discussions

To assess the importance of graphene conductivity and associated polarization effects on its wetting propensity, we monitor simulated water nanodrops on a suspended (unsupported) graphene sheet and on a sheet supported by liquid water from the opposite side. In each of the two scenarios, we compare the results for water contact angles, and characteristic structures of hydration water, using a conventional graphene model devoid of atom charges or polarizability with those obtained by accounting for the conductor properties of graphene.

The cylindrical droplet shape is used to avoid line tension effects with nanodrop sizes amenable to MD simulations. The model setups are illustrated in Figure 32, and the details

are given in the Methods section. The force field treating graphene as an insulator has been described in earlier work⁶. In the present work, the conductivity is incorporated using the method of fluctuating charges from the Constant Potential Molecular Dynamics (CPMD) developed by Sprik and Siepmann³⁹ and Madden and coworkers⁴⁰. In this approach, every carbon atom of graphene carries a Gaussian charge distribution $\rho_j(r - r_j)$ with an

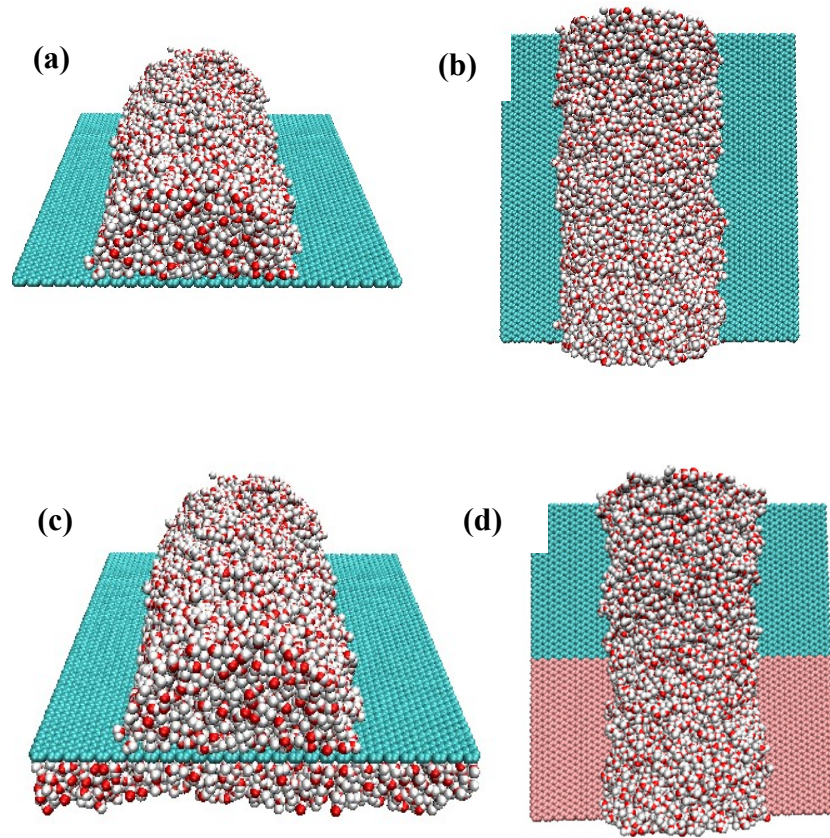


Figure 32: Snapshots of spreading of the semi-infinite hemi-cylindrical water droplet atop insulator without (a-b) or with a layer of water (c) placed below the sheet. The system containing a 6.4×10^3 molecule drop and 5.6×10^3 atom graphene sheet is periodically replicated in lateral directions. (d) A snapshot of a cylindrical water droplet atop graphene sheet in CPMD (See Methods section).

integrated charge of q_j and the fixed Gaussian charge width⁴⁰ η .

$$\rho_j(r) = q_j A \exp(-|r - r_j|^2 \eta^{-2}) \quad (8)$$

where r_j denotes the atom's position, q_j is the instantaneous value of the fluctuating charge on atom j , and $A = \eta^3 \pi^{3/2}$ is the normalization constant. Oxygen and hydrogen atoms of water molecules carry fixed point charges, with the local charge density $\rho(r)$ at the position r due to an atom i located at r_i given by

$$\rho_i(r) = q_i \delta(r - r_i) \quad (9)$$

where $\rho(r)$ and $\delta(r - r_j)$ are total charge density and delta function. The total charge density at r is given as the sum of contributions from all carbon atoms (Eq. 1) and partial charges from the water molecules (Eq. 2). The internal columbic energy of the system U_c is

$$U_c = \frac{1}{2} \iint \frac{\rho(r') \rho(r'')}{|r' - r''|} dr' dr'' \quad (10)$$

To secure a desired electrostatic potential V_j^0 on graphene atoms (typically the imposed electrode potential), carbon charges q_j undergo a perpetual redistribution responding to the changing configuration of water molecules. In a general case, the instantaneous charges q_j are obtained variationally by minimizing the total electrostatic energy.

$$U_e^{\text{tot}} = U_c - \sum_j V_j^0 q_j \quad (11)$$

In the present scenario, V_j^0 are set equal to zero for all carbon atoms j and the minimization is carried out subject to the net neutrality condition, $\sum_j q_j = 0$.

As detailed in the Methods section, we model water molecules using the SPC/E water potential⁹⁶ and graphene atoms as Lennard-Jones (LJ) particles. In view of experimental uncertainties in determining the suspended graphene/water interaction^{76, 78, 145, 146}, we consider three different strengths of carbon interaction with water oxygen atoms, ϵ_{co} Table 1 with the intermediate strength, $\epsilon_{co} \sim 0.39 \text{ kJ mol}^{-1}$ corresponding to recent experimental⁷⁶ and quantum-mechanical simulation⁶⁹ estimate for the CA on neat suspended graphene at $\sim 86 \pm 3^\circ$. Results for weaker ($\epsilon_{co} \sim 0.195 \text{ kJ mol}^{-1}$) and stronger ($\epsilon_{co} \sim 0.52 \text{ kJ mol}^{-1}$) water surface interactions are included to cover the broad range of CA values indicated in independent experiments. Identical LJ interactions are used in conducting and insulator representations. In describing our results, we refer to the conducting (CPMD fluctuating-charge) and nonconducting model systems using the terms ‘graphene’ and ‘insulator’, respectively.

Table 1: Contact angle θ of a cylindrical droplet on the suspended and supported graphene for different values of ε_{co} . θ_c refers to measurements to measurements without a water layer underneath the surface and θ_w correspond to a layer of water placed underneath graphene.

ε_{co} /kJ mol ⁻¹	suspended insulator θ_c	water- supported insulator θ_w	suspended graphene θ_w	water-supported graphene θ_w
0.1951	127°±1°	120°±1°	118°±1°	105°±1°
0.3913	87°±1°	81°±1°	87°±1°	75°±1°
0.5208	59°±1°	52°±1°	54°±1°	45°±1°

3.2.1 Graphene/water density profiles

We begin by describing the structure of hydration layers on both sides of the surface. The oxygen density profiles shown in Figure 33 reveal only a small difference in the distributions of water molecules on the insulator compared to the graphene sheet. The only detectable difference is seen in the slight increase in the heights of the first hydration peaks for both the suspended and supported graphene relative to those observed with the insulator sheet. In Figure 34, we compare the density profiles of water next to strongly hydrophobic and hydrophilic insulator surfaces (Systems 1 and 3 in the 1st column in Table 1) on both sides of the submerged graphene sheet. These results show the 1st peak positions at the hydrophobic surfaces are significantly lower and slightly (~ 1Å) withdrawn from the sheets compared to the hydrophilic cases. Water density profiles are essentially identical on both sides of the graphene sheet, the small reduction of the height of the 1st peak on the drop

side being explained by mild density variation along the radial direction of the droplet's base.

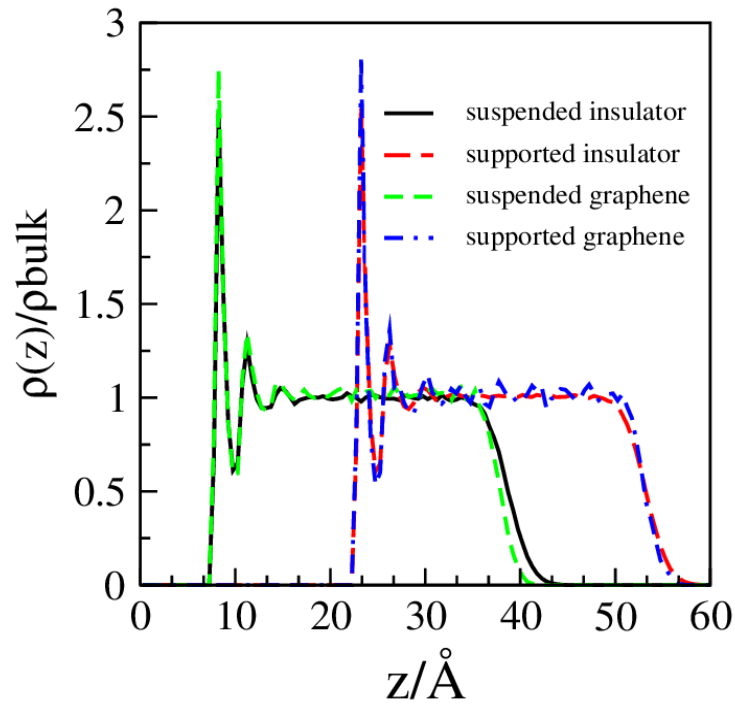


Figure 33: Density profiles of water in the central region of a cylindrical droplet base on the suspended or supported insulator and graphene sheets (modeled by CPMD) with $\epsilon_{co} = 0.3913 \text{ kJ mol}^{-1}$. Black curve: simulation result for the droplet density as function of the height z on the suspended insulator. Red: droplet on the insulator supported by an aqueous layer. Green: droplet on the suspended graphene. Blue: droplet on supported graphene. The densities are normalized by the density inside the bulk portion of the droplet.

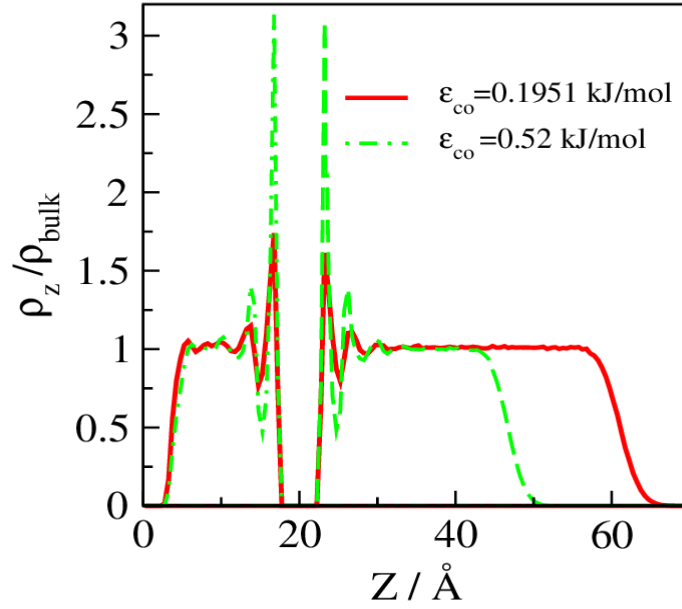


Figure 34: Density profile of water on both side of the insulator surface for $\epsilon_{co} = 0.1951$ or $0.5208 \text{ kJ mol}^{-1}$. The plot shows each profile in relation to the z-dimension of the system box. The insulator sheet is placed at $z = 20 \text{ \AA}$.

3.2.2 Contact angles

Figure 35 illustrates the time dependence of the dynamic contact angles we extract from the instantaneous droplet contours as detailed in the Methods section. Figure 35-left shows the simulated contact angles of a cylindrical droplet on a suspended graphene sheet obtained using the insulator (black) or conducting graphene (green) models. Figure 35-right compares the CA results for (conducting) graphene in two different situations: (a) suspended sheet with empty space underneath, and (b): supported sheet atop a slab of water. As shown in Table 1, the reduction in contact angle on submerged conducting graphene is between 9° - 13° , considerably more than the change of 6° - 7° predicted⁶ with the insulator model. The comparison between the two different surface models shows that the conductivity of the surface has a smaller effect on the contact angle when the droplet is placed on a suspended sheet.

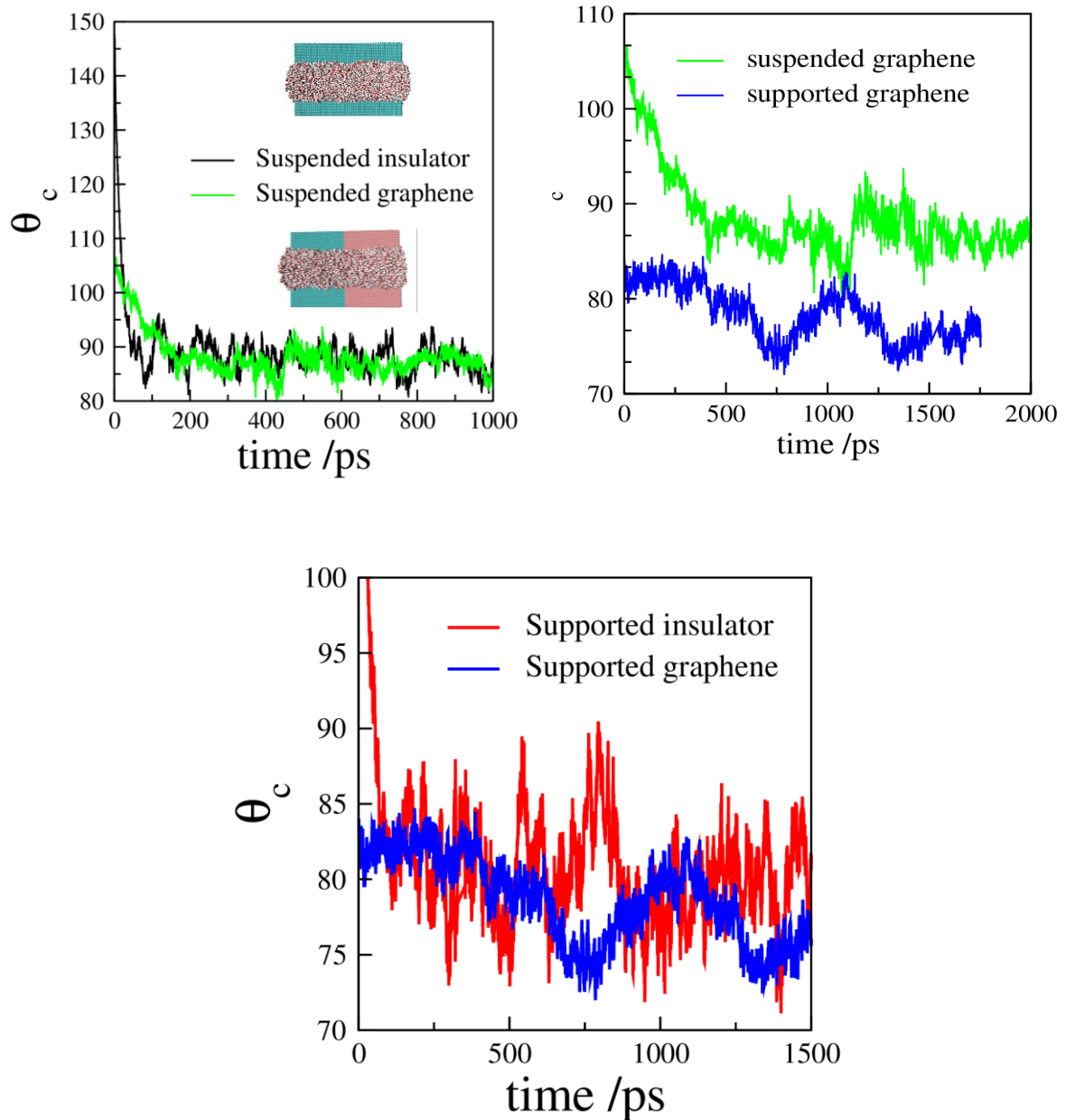


Figure 35: Contact angle vs time for a cylindrical water droplet on the suspended insulator and graphene sheets (left), suspended or water-supported graphene sheets (right), and supported insulator and supported graphene (bottom) for carbon-water interaction strengths $\epsilon_{co} = 0.3913 \text{ kJ mol}^{-1}$.

Table 1 also compares the results of time-averaged contact angles of water on graphene and insulator surfaces for a different set of oxygen-carbon energy parameters ϵ_{co} . These results show that the inclusion of material conductivity is most visible on hydrophobic model surfaces where the related polarization effects present a greater share in the total surface/water attraction. Lastly we note a difference between our results for water on graphene and the original calibration for graphite provided by Werder et al.¹⁴⁷ In addition to replacing graphite by graphene, this differences reflect several methodology improvements, the most significant being the use of Ewald summation to avoid the cutoff (10 Å in Ref.¹⁴⁷) of electrostatic interactions, and the choice of cylindrical drop geometry⁷⁷ to eliminate the finite-size effects associated with line tension.

3.2.3 Dipolar correlations across graphene.

To gain a more detailed picture of the orientational polarization of hydration water, in Figure 36 we show the water dipole angle distributions $p(\cos \varphi)$ for both the suspended and supported insulator and conducting graphene sheets. Here, φ represents the angle between a water dipole and the normal to the graphene surface. We quantify the interfacial polarization in terms of the average dipole of the interfacial molecules $\langle \boldsymbol{\mu}(t) \rangle = \frac{1}{N} \langle \sum_i^N \boldsymbol{\mu}_i(t) \rangle$, where the sum runs over all water dipoles $\boldsymbol{\mu}_i$ in the first hydration layer. We define this layer as the region between the surface and the first minimum in the water/surface density profile. As can be seen in Figure 36, in the system with the insulating surface (black and red curves in Figure 36), the presence of the supporting aqueous slab has a strong influence on the orientational polarization in the droplet base. This effect,

associated with dipole-dipole interaction across the surface, is essentially screened out when we include graphene conductivity (green and blue curves). As will be shown below, it turns out that partial molecular charges of the same sign appear attracted to each other across the conducting graphene in contrast to the conventional picture observed with the insulator model, where attractions apply to charges of opposite signs. In addition to the average dipole moments shown in Figure 36, we also calculate the variances of dipole components, $\langle \delta\mu_\alpha^2 \rangle$, (Table 2) and the dipole-dipole correlation functions, $c_\alpha(r) = \frac{\langle \delta\mu_\alpha^{top}(r)\delta\mu_\alpha^{bottom}(0) \rangle}{\langle \delta\mu_\alpha^2 \rangle} >$ based on molecular orientations in the 1st hydration layers of the cylindrical droplet base on top of the graphene, μ_{top} , and in the aqueous slab below the water-supported sheet, μ_{bottom} . We present results for both the conducting and non-conducting graphene models (Figure 37). The distance r corresponds to the lateral distance between the centers of a pair of dipoles in the opposite hydration layers and the average is taken over all possible pairs. In all cases, the variances $\langle \delta\mu_\alpha^2 \rangle$ are essentially identical on both sides of the sheet. As expected, the correlations across nonconducting graphene sheet at small lateral distances r (Figure 37) are positive for z components (normal to the surface) of the dipole moments of water, and negative for the lateral (x,y) components. Interestingly, the sign of both correlation functions, $c_z(r)$ and $c_{xy}(r)$, at small r is *reversed* when we apply the conducting graphene model. This qualitative change is explained in terms of the polarization of graphene, with image charges inside the conductor layer

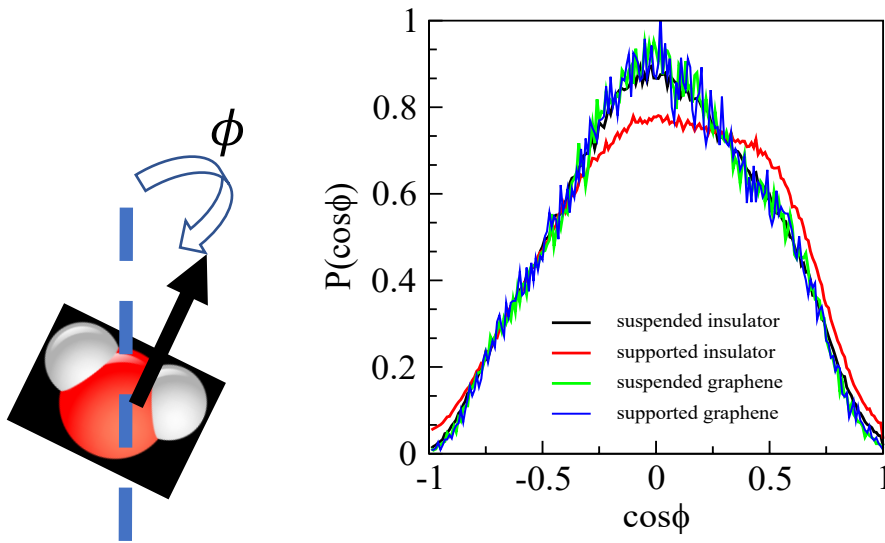


Figure 36: Dipole angle probability distributions $P(\cos \phi)$ for water molecules in the solid/water contact layer of the cylindrical nanodroplet on different surfaces $\varepsilon_{co} = 0.3013 \text{ kJ mol}^{-1}$, $\sigma_{co} = 3.19 \text{ \AA}$. Black line: suspended insulator. Red: water-supported insulator. Green color: suspended graphene, blue color: water-supported graphene.

attracting equally signed partial charges of water molecules on both sides of the sheet. A related sign reversal has been indicated in two⁴¹ and three-dimensional^{148, 149} ionic systems in the presence of temporal or spatial fluctuations of charge-density distributions. The insulator model devoid of polarization effects, on the other hand, features the expected Coulombic attraction between the partial charges of opposite signs. The two distinct behaviors are illustrated in the insets in Figure 38 showing favored configurations for a pair of water molecules interacting across the graphene sheet.

The correlations across the sheet introduce a subtle interaction term, which is superimposed to much stronger molecular interactions, including hydrogen bonding, inside a contiguous

liquid on either side of graphene, and the dispersion attraction to the carbon sheet. These interactions result in a spontaneous near-parallel alignment of the dipoles in the hydration layer along the surface, with only a slight preference for dipole orientation pointing into the liquid phase (See Figure 38 and Table 2). When water is present on *both* sides of the (nonpolarizable) insulator sheet, the lateral alignment of the dipoles with the surface is slightly destabilized (Figure 36) as the chain dipole-dipole configuration enables a stronger dipolar interaction across the sheet than the antiparallel one¹⁵⁰. An analogous perturbation of water-wall orientations does not take place with the conducting graphene, where the direct dipole-dipole

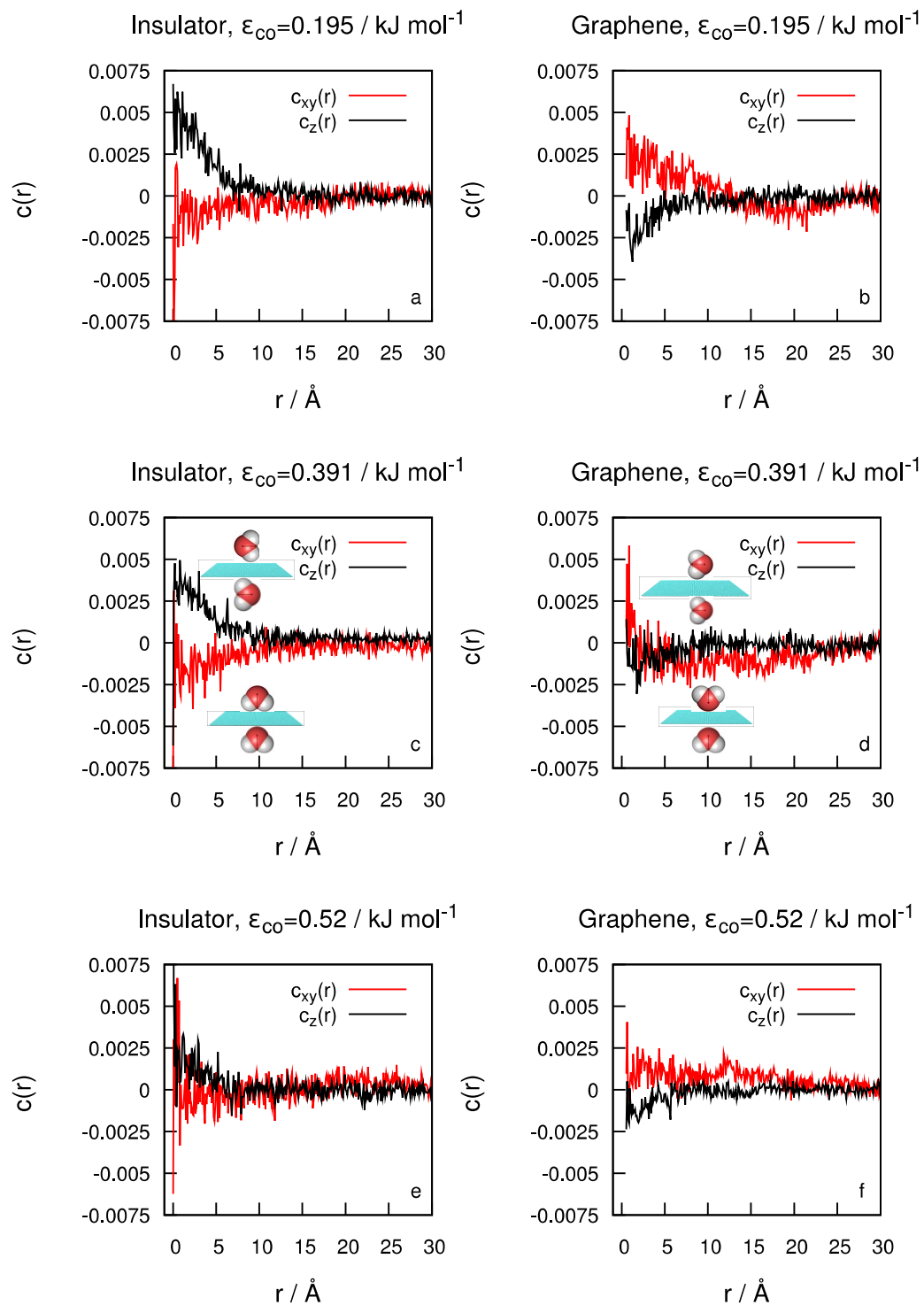


Figure 37: Dipole-dipole correlation functions measuring orientational correlations between water molecules in the hydration layers of a cylindrical droplet atop the insulator sheet (left: a,c,e) or conducting graphene (right: b,d,f), and liquid water below the sheet for different values of ϵ_{co} .

interaction across the sheet is overwhelmed by the interaction with image charges induced by the molecules from *both* sides of the sheet and where the attraction by the image charges is compatible with the (already favored) lateral dipole alignment with the surface.

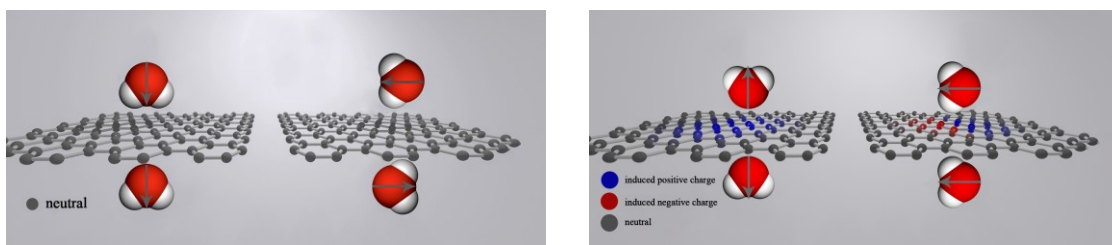


Figure 38: Favored configurations for a pair of water molecules interacting across the graphene sheet. Insulator sheet (left), conducting graphene (right), and liquid water below the sheet for different values of $\varepsilon_{co} = 0.3913 \text{ kJ mol}^{-1}$, $\sigma_{co} = 3.19 \text{ \AA}$.

Although the conducting graphene screens the direct interaction between the dipoles on the opposing sides of graphene, the attraction by image charges induced by the molecules from both sides results in the overall *increase* in the wetting affinity and a reduction of the contact angle relative to that observed with the insulator model. Interestingly, the synergistic effect of graphene polarization due to the molecules from both sides is required to observe a notable contact angle change, while the introduction of material's conductivity has a smaller effect with droplets on suspended graphene, *i.e.* in the absence of aqueous support.

To illustrate the conductivity and hydrophilicity effects on spontaneous orientation and orientational polarizability, in Table 2 we compare the average dipole moment normal to the graphene surface and the variance of the normal and lateral dipole components for both

non-conducting and conducting graphene characterized by different water-carbon interaction strengths from Table 1. The weak polarization of water quantified in terms of finite $\langle \mu_z \rangle$ (with the dipoles pointing slightly away from the interface) slowly increases upon strengthening the water-surface attraction. The change takes place symmetrically on both sides of the sheet. While the addition of water on both sides of the insulating sheet weakens the preference for the dipole alignment with the surface (Figure 36), the positive and negative deviations mostly cancel, leaving only a small enhancement of the polarization $\langle \mu_z \rangle$ upon the introduction of aqueous support under graphene.

The data describing orientation fluctuations of water molecules next to graphene (Table 2) reveal a remarkable difference between the variances of water dipole components in the normal and lateral directions. The difference conforms to the known anisotropies of the orientational polarizability and permittivity tensors of interfacial water. Specifically, the orientational polarizability of water molecules along the surface normal, $\alpha_{zz}^{or} \sim \frac{\langle \delta \mu_z^2 \rangle}{kT}$, is almost twice smaller than the corresponding values in the lateral (x,y) directions. α_{zz}^{or} decreases further with strengthened orientational restrictions when the surface is rendered more hydrophilic. A similar effect is observed in the presence of image charges in graphene when treated as a conductor. Conversely, the increase in hydrophilicity, and the addition of image charge effects, result in a slight *enhancement* of the lateral polarizability components (α_{xx}^{or} and α_{yy}^{or}). Because of the close relation between the dielectric constant and the dipoles' fluctuation $\langle \delta \mu \rangle^2$, our results indicate that the lateral

components of the permittivity tensor substantially exceed the normal component in analogy to the observations in a planar confinement¹⁵¹.

Table 2: Average dipole moments and mean squared fluctuations of dipole components (x, y, or z) of water molecules in the first hydration layers of an insulating (a) and conducting (b) model graphene sheets wetted by an aqueous drop on the top side and supported by an aqueous slab on the bottom, all for three different carbon-water interaction strengths ϵ_{co} . (c) suspended insulating sheet.

(a) graphene-like insulator sheet on water

$\frac{\epsilon_{co}}{kJmol^{-1}}$	$\langle \mu_z \rangle_{top}$ D	$\langle \mu_z \rangle_{bot}$ D	$\langle \delta\mu_{x,y}^2 \rangle$ D^2	$\langle \delta\mu_z^2 \rangle$ D^2
0.1951	0.100	-0.110	2.19	1.14
0.3913	0.124	-0.122	2.21	1.08
0.5208	0.132	-0.128	2.23	1.04

(b) conducting graphene on water

$\frac{\epsilon_{co}}{kJmol^{-1}}$	$\langle \mu_z \rangle_{top}$ D	$\langle \mu_z \rangle_{bot}$ D	$\langle \delta\mu_{x,y}^2 \rangle$ D^2	$\langle \delta\mu_z^2 \rangle$ D^2
0.1951	0.104	-0.104	2.20	1.10
0.3913	0.120	-0.122	2.24	1.04
0.5208	0.126	-0.134	2.26	0.99

(c) suspended sheet:

$\frac{\epsilon_{co}}{kJmol^{-1}}$	$\langle \mu_z \rangle_{insulator}^{top}$	$\langle \mu_z \rangle_{graphene}^{top}$
0.1951	0.089	0.106
0.3625	0.118	-
0.3913	0.122	0.129
0.5208	0.130	0.133

3.2.4 Non-polar liquid

To enable a comparison with systems devoid of long-range electrostatics, we follow the same procedure to compute contact angles of diiodomethane (CH_2I_2) on suspended and CH_2I_2 - supported graphene sheets. The hemicylindrical drop was divided into three slices to remove the possible effect due to long-range triple line fluctuations. The drop contour of each slice was calculated through a square binning of the local number of heavy (C and I) atoms on the yz plane with a 3\AA resolution.

The results for time-averaged contact angles of diiodomethane on suspended and supported graphene are 50.8° and 48.9° , respectively. The contact angle reduction of about 2° affirms a degree of ‘wetting translucency’ when the liquid molecules interact across graphene solely through dispersion forces. Within statistical uncertainty, the magnitude of the effect agrees with the mean field prediction for the van der Waals contribution to the contact angle reduction:

$$\Delta \cos \theta \sim -\frac{2\pi \sum_i \sum_j \rho_i \rho_j \varepsilon_{ij} \sigma_{ij}^6}{6\gamma d_{ij}^2} \quad (12)$$

introduced in our earlier work⁶. Here, the summation runs over all interacting site pairs (i, j) of liquid molecules (I and CH₂ with the united-atom CH₂I₂ model) of site number densities ρ_i and Lennard Jones parameters $\varepsilon_{ij} = (\varepsilon_i \varepsilon_j)^{1/2}$, $\sigma_{ij} = (\sigma_i + \sigma_j)/2$, and $d_{ij} = (\sigma_c + \sigma_{ij})$. γ is the surface tension of the liquid. Using the diiodomethane parameters collected in the Force fields section obtains the contact angle reduction for the submerged graphene in diiodomethane $\Delta \theta \sim -3^\circ$. Since diiodomethane molecules carry only minute atom charges (see Methods section), the electrostatic interactions between the droplet and the solvent slab below graphene, along with any image charge effects, remain too weak to manifest the trends observed with the highly polar water molecules (Fig. 6). The results for the diiodomethane system are hence independent of whether we treat graphene as an insulator or a conductor; the use of the advanced CPMD approach is not warranted in these cases.

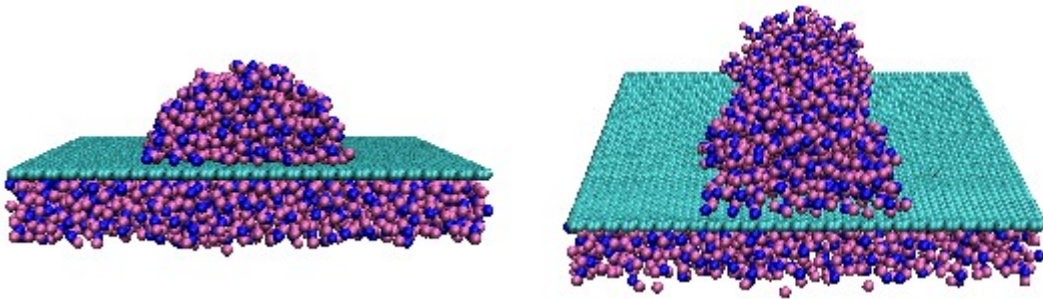


Figure 39: Snapshots of spreading of the semi-infinite hemi-cylindrical CH_2I_2 droplet atop insulator with a layer of diiodomethane of thickness 13.1 Å placed below the sheet.

3.3 Conclusion

Using Constant Potential Molecular Dynamics simulations, we examine the influence of liquid-liquid interactions across a *conducting* graphene sheet on the wetting propensity, which we quantify in terms of the contact angle of a cylindrical nanodroplet spreading over the graphene surface. We present a comparison between the systems with and without the supporting liquid under the sheet, and with systems ignoring graphene's conductivity and associated polarization. Our results show the impact of the supporting liquid is substantially stronger when graphene's conductivity is taken into account notwithstanding the screening of direct electrostatic interactions between polar molecules at the opposite sides of the graphene layer. We explain this counterintuitive behavior in terms of the effective attraction between partial molecular charges of the equal sign, mediated by image charges induced in graphene to eliminate the lateral electric field inside the conductor. The mechanism is confirmed by monitoring the orientational correlations among water molecules at the opposite sides of the graphene sheet. A pair of water molecules facing each other across an insulator sheet tend to favor an antiparallel alignment along lateral (x,y) directions and a parallel one along the surface normal (z) to minimize their dipolar interaction. Addition of water under graphene sheet hence perturbs molecular orientations in the droplet base atop the sheet. When we incorporate graphene conductivity, the polarization of the model graphene sheet shields the direct dipole-dipole interactions across it. The image charges on graphene, positioned between the partial charges on water atoms at the opposite sides of the sheet introduce an indirect attraction between like charges,

reversing the sign of dipolar correlations across the sheet. To balance the electrostatic potential due to like charges of polar water molecules from both sides of the sheet enhances the magnitude of local graphene polarization, resulting in an enhanced propensity for wetting. The reduction of water contact angle on the conducting graphene wetted on both sides is hence considerably greater than predicted using the insulator graphene model. Accounting for this difference is significant for accurate model predictions of wetting properties of graphene and related monolayer materials like boron-nitride. Parallel computations in a nonpolar liquid, diiodomethane, whose properties are dominated by the van der Waals interactions, on the other hand, show no dependence on graphene electrostatics. In this case, a moderate wettability increase upon two-side wetting agrees with the mean field prediction for the contact angle reduction, which relies solely on direct dispersion forces between the liquid molecules on two sides of the sheet, unaffected by the intervening carbon layer.

Chapter 4: Summary and outlook

This thesis is about the adhesion at solid/liquid interfaces. We use molecular dynamics simulations to first study and understand the physics and the pathway of droplet detachment from fiber and surface and predict the percentage of residue that remains on fiber/surface. Second, we address this question: how does the improvement of graphene model by force field accounting for conductivity affect the wetting transparency of graphene?

In the first project, we study the mechanism of water droplet detachment and retention of residual water on smooth hydrophilic fibers using nonequilibrium molecular dynamics simulations. We extract scaling relations that allow extrapolation of our findings to larger length scales that are not directly accessible by molecular models. Our studies of the droplet breakup uncover a strongly nonmonotonic influence of the external force, with the amount of residual water maximized under the intermediate force strengths whereas a complete or near-complete detachment of the droplet can be achieved in both extremes, with the applied force only slightly, or considerably exceeding the minimal force of detachment. The strength of this force decreases with the size of the drop, while the maximal residue increases with the droplet volume, V , sub-linearly, in proportion to the $V^{2/3}$. Next, we compare our finding with the results for droplet detachment from the flat surface by experiments and Molecular Dynamics simulations conducted on water droplet. We find that the maximum amount of residue can be observed by applying the minimum force of detachment in contrast to experimental and MD results for droplet detachment from the curved surfaces where intermediate force was found to maximize the water retention.

In the second project, we found that the contact angle of a water droplet on a graphene sheet submerged in water is lower than in the absence of water under graphene. Our calculations reveal effective attractions between partial charges of equal sign across the conducting graphene sheet. Attractive correlations are attributed to the formation of the highly localized image charges on carbon atoms between the partially charged sites of water molecules on both sides of graphene. By performing additional computations with nonpolar diiodomethane, we confirm that graphene is transparent to dispersive interactions. These findings are important in applications including sensors, fuel cell membranes, and water filtration, and graphene-based electrode material to enhance the supercapacitor performance.

In future studies, we are planning to develop computational methodologies for understanding of biomolecule adsorption on metallic surfaces (conducting nano-corrugated Pt surface). The relative significance of the effect observed with simple biomolecules will guide extensions to more complex ones. The problem of protein adsorption on a rough metallic implant surface has far-reaching medical implications that cannot be successfully addressed by conventional force fields at the classical level.

References

1. Alcantara, L. O.; Martins, M. E. D.; Sousa, J. R.; Cerqueira, M. A.; Silva, A. L. C.; Souza, M. D. M.; Souza, B. W. S., Wettability of Edible Coatings on Nile Tilapia Fillets (*Oreochromis Niloticus*). *J. Food Eng.* **2019**, *247*, 152-159.
2. Boyd, D. A.; Frantz, J. A.; Bayya, S. S.; Busse, L. E.; Kim, W.; Aggarwal, I.; Poutous, M.; Sanghera, J. S., Modification of nanostructured fused silica for use as superhydrophobic, IR-transmissive, anti-reflective surfaces. *Opt. Mater.* **2016**, *54*, 195-199.
3. Bonn, D.; Eggers, J.; Indekeu, J.; Meunier, J.; Rolley, E., Wetting and Spreading. *Rev. Mod. Phys.* **2009**, *81* (2), 739-805.
4. Bormashenko, E., Progress in Understanding Wetting Transitions on Rough Surfaces. *Adv. Colloid Interface Sci.* **2015**, *222*, 92-103.
5. Zisman, W. A., Relation of the Equilibrium Contact Angle to Liquid and Solid Constitution. In: Contact Angle Wettability and Adhesion. *Advances in Chemistry.* **1964**, 1-51.
6. Driskill, J.; Vanzo, D.; Bratko, D.; Luzar, A., Wetting Transparency of Graphene in Water. *J. Chem. Phys.* **2014**, *141*, 18C517.
7. Ju, J.; Bai, H.; Zheng, Y. M.; Zhao, T. Y.; Fang, R. C.; Jiang, L., A Multi-Structural and Multi-Functional Integrated Fog Collection System in Cactus. *Nat. Commun.* **2012**, *3*, 1247.
8. Park, K. C.; Chhatre, S. S.; Srinivasan, S.; Cohen, R. E.; McKinley, G. H., Optimal Design of Permeable Fiber Network Structures for Fog Harvesting. *Langmuir* **2013**, *29* (43), 13269-13277.
9. Shi, W. W.; Anderson, M. J.; Tulkoe, J. B.; Kennedy, B. S.; Boreyko, J. B., Fog Harvesting with Harps. *ACS Appl. Mater. Interfaces* **2018**, *10* (14), 11979-11986.
10. Patel, S. U.; Chase, G. G., Separation of Water Droplets from Water-in-Diesel Dispersion Using Superhydrophobic Polypropylene Fibrous Membranes. *Sep. Purif. Technol.* **2014**, *126*, 62-68.
11. Kampa, D.; Wurster, S.; Buzengeiger, J.; Meyer, J.; Kasper, G., Pressure Drop and Liquid Transport through Coalescence Filter Media Used for Oil Mist Filtration. *Int. J. Multiphase Flow* **2014**, *58*, 313-324.
12. Song, J. L.; Huang, S.; Lu, Y.; Bu, X. W.; Mates, J. E.; Ghosh, A.; Ganguly, R.; Carmalt, C. J.; Parkin, I. P.; Xu, W. J.; Megaridis, C. M., Self-Driven One-Step Oil Removal from Oil Spill on Water Via Selective-

Wettability Steel Mesh. *ACS Appl. Mater. Interfaces* **2014**, *6* (22), 19858-19865.

13. Ramos-Alvarado, B.; Sole, J. D.; Hernandez-Guerrero, A.; Ellis, M. W., Experimental Characterization of the Water Transport Properties of Pem Fuel Cells Diffusion Media. *J. Power Sources* **2012**, *218*, 221-232.

14. Hanumanthu, R.; Stebe, K. J., Equilibrium Shapes and Locations of Axisymmetric, Liquid Drops on Conical, Solid Surfaces. *Colloids Surf. A.* **2006**, *282*, 227-239.

15. McHale, G.; Newton, M. I., Global Geometry and the Equilibrium Shapes of Liquid Drops on Fibers. *Colloids Surf. A.* **2002**, *206* (1-3), 79-86.

16. Eral, H. B.; de Ruiter, J.; de Ruiter, R.; Oh, J. M.; Semprebon, C.; Brinkmann, M.; Mugele, F., Drops on Functional Fibers: From Barrels to Clamshells and Back. *Soft Matter* **2011**, *7* (11), 5138-5143.

17. de Ruiter, R.; de Ruiter, J.; Eral, H. B.; Semprebon, C.; Brinkmann, M.; Mugele, F., Buoyant Droplets on Functional Fibers. *Langmuir* **2012**, *28* (37), 13300-13306.

18. Milchev, A.; Binder, K., Polymer Nanodroplets Adsorbed on Nanocylinders: A Monte Carlo Study. *J. Chem. Phys.* **2002**, *117* (14), 6852-6862.

19. Chou, T. H.; Hong, S. J.; Liang, Y. E.; Tsao, H. K.; Sheng, Y. J., Equilibrium Phase Diagram of Drop-on-Fiber: Coexistent States and Gravity Effect. *Langmuir* **2011**, *27* (7), 3685-3692.

20. Funk, C. S.; Winzer, B.; Peukert, W., Correlation between Shape, Evaporation Mode and Mobility of Small Water Droplets on Nanorough Fibres. *J. Colloid Interface Sci.* **2014**, *417*, 171-179.

21. Amrei, M. M.; Davoudi, M.; Chase, G. G.; Tafreshi, H. V., Effects of Roughness on Droplet Apparent Contact Angles on a Fiber. *Sep. Purif. Technol.* **2017**, *180*, 107-113.

22. Mullins, B. J.; Agranovski, I. E.; Braddock, R. D.; Ho, C. M., Effect of Fiber Orientation on Fiber Wetting Processes. *J. Colloid Interface Sci.* **2004**, *269* (2), 449-458.

23. Bick, A.; Boulogne, F.; Sauret, A.; Stone, H. A., Tunable Transport of Drops on a Vibrating Inclined Fiber. *Appl. Phys. Lett.* **2015**, *107*, 181604.

24. Hotz, C. J.; Mead-Hunter, R.; Becker, T.; King, A. J. C.; Wurster, S.; Kasper, G.; Mullins, B. J., Detachment of Droplets from Cylinders in Flow Using an Experimental Analogue. *J. Fluid Mech.* **2015**, *771*, 327-340.

25. Mullins, B. J.; Pfrang, A.; Braddock, R. D.; Schimmel, T.; Kasper, G., Detachment of Liquid Droplets from Fibres - Experimental and

Theoretical Evaluation of Detachment Force Due to Interfacial Tension Effects. *J. Colloid Interface Sci.* **2007**, *312* (2), 333-340.

26. Sahu, R. P.; Sinha-Ray, S.; Yarin, A. L.; Pourdeyhimi, B., Blowing Drops Off a Filament. *Soft Matter* **2013**, *9* (26), 6053-6071.

27. Davoudi, M.; Fang, J.; Chase, G. G., Barrel Shaped Droplet Movement at Junctions of Perpendicular Fibers with Different Orientations to the Air Flow Direction. *Sep. Purif. Technol.* **2016**, *162*, 1-5.

28. Amrei, M. M.; Venkateshan, D. G.; D'Souza, N.; Atulasimha, J.; Tafreshi, H. V., Novel Approach to Measuring the Droplet Detachment Force from Fibers. *Langmuir* **2016**, *32* (50), 13333-13339.

29. Aziz, H.; Tafreshi, H. V., Competing Forces on a Liquid Bridge between Parallel and Orthogonal Dissimilar Fibers. *Soft Matter* **2019**, *15* (35), 6967-6977.

30. Farhan, N. M.; Tafreshi, H. V., Using Magnetic Field to Measure Detachment Force between a Nonmagnetic Droplet and Fibers. *Langmuir* **2019**, *35* (25), 8490-8499.

31. Jamali, M.; Moghadam, A.; Tafreshi, H. V.; Pourdeyhimi, B., Droplet Adhesion to Hydrophobic Fibrous Surfaces. *Appl. Surf. Sci.* **2018**, *456*, 626-636.

32. Moghadam, A.; Yousefi, S. H.; Tafreshi, H. V.; Pourdeyhimi, B., Characterizing Nonwoven Materials Via Realistic Microstructural Modeling. *Sep. Purif. Technol.* **2019**, *211*, 602-609.

33. Yousefi, S. H.; Venkateshan, D. G.; Tang, C.; Tafreshi, H. V.; Pourdeyhimi, B., Effects of Electrospinning Conditions on Microstructural Properties of Polystyrene Fibrous Materials. *J. Appl. Phys.* **2018**, *124* (23), 235307.

34. Kim, S. G.; Kim, W., Drop Impact on a Fiber. *Phys. Fluids* **2016**, *28* (4), 042001.

35. Dressaire, E.; Sauret, A.; Boulogne, F.; Stone, H. A., Drop Impact on a Flexible Fiber. *Soft Matter* **2016**, *12* (1), 200-208.

36. Hou, Y. P.; Chen, Y.; Xue, Y.; Zheng, Y. M.; Jiang, L., Water Collection Behavior and Hanging Ability of Bioinspired Fiber. *Langmuir* **2012**, *28* (10), 4737-4743.

37. Weyer, F.; Lismont, M.; Dreesen, L.; Vandewalle, N., Compound Droplet Manipulations on Fiber Arrays. *Soft Matter* **2015**, *11* (36), 7086-7091.

38. Petersen, M. K.; Kumar, R.; White, H. S.; Voth, G. A., A Computationally Efficient Treatment of Polarizable Electrochemical Cells Held at a Constant Potential. *J. Phys. Chem. C* **2012**, *116* (7), 4903-4912.

39. Siepmann, J. I.; Sprik, M., Influence of Surface-Topology and Electrostatic Potential on Water Electrode Systems. *J. Chem. Phys.* **1995**, *102* (1), 511-524.
40. Reed, S. K.; Lanning, O. J.; Madden, P. A., Electrochemical Interface between an Ionic Liquid and a Model Metallic Electrode. *J. Chem. Phys.* **2007**, *126* (8), 084704.
41. Mendez-Morales, T.; Burbano, M.; Haefele, M.; Rotenberg, B.; Salanne, M., Ion-Ion Correlations across and between Electrified Graphene Layers. *J. Chem. Phys.* **2018**, *148* (19), 193812.
42. Geim, A. K., Graphene: Status and Prospects. *Science* **2009**, *324* (5934), 1530-1534.
43. Zhong, Y. J.; Zhen, Z.; Zhu, H. W., Graphene: Fundamental Research and Potential Applications. *Flatchem* **2017**, *4*, 20-32.
44. Abergel, D. S. L.; Apalkov, V.; Berashevich, J.; Ziegler, K.; Chakraborty, T., Properties of Graphene: A Theoretical Perspective. *Adv. Phys.* **2010**, *59* (4), 261-482.
45. Sattar, T., Current Review on Synthesis, Composites and Multifunctional Properties of Graphene. *Top. Curr. Chem.* **2019**, *377* (2).
46. Osada, M.; Sasaki, T., Two-Dimensional Dielectric Nanosheets: Novel Nanoelectronics from Nanocrystal Building Blocks. *Adv. Mater.* **2012**, *24* (2), 210-228.
47. Nandee, R.; Chowdhury, M. A.; Ahmed, M. U.; Shuvho, B. A.; Debnath, U. K., Performance and Characterization of Two-Dimensional Material Graphene Conductivity-a Review. *Mater. Performance* **2019**, *8* (1), 183-196.
48. Ferrari, G. A.; de Oliveira, A. B.; Silvestre, L.; Matos, M. J. S.; Batista, R. J. C.; Fernandes, T. F. D.; Meireles, L. M.; Eliel, G. S. N.; Chacham, H.; Neves, B. R. A.; Lacerda, R. G., Apparent Softening of Wet Graphene Membranes on a Microfluidic Platform. *Acs Nano* **2018**, *12* (5), 4312-4320.
49. Liu, F. Y.; Navaraj, W. T.; Yogeswaran, N.; Gregory, D. H.; Dahiya, R., van der Waals Contact Engineering of Graphene Field-Effect Transistors for Large-Area Flexible Electronics. *Acs Nano* **2019**, *13* (3), 3257-3268.
50. Mas-Balleste, R.; Gomez-Navarro, C.; Gomez-Herrero, J.; Zamora, F., 2d Materials: To Graphene and Beyond. *Nanoscale* **2011**, *3* (1), 20-30.
51. Fiori, G.; Bonaccorso, F.; Iannaccone, G.; Palacios, T.; Neumaier, D.; Seabaugh, A.; Banerjee, S. K.; Colombo, L., Electronics Based on Two-Dimensional Materials. *Nat. Nanotechnol* **2014**, *9* (10), 768-779.

52. Yazyev, O. V.; Chen, Y. P., Polycrystalline Graphene and Other Two-Dimensional Materials. *Nat. Nanotechnol* **2014**, *9* (10), 755-767.
53. Zhang, G. Y.; Du, S. X.; Wu, K. H.; Gao, H. J., Two-Dimensional Materials Research. *Science* **2018**, *360* (6389), 15-18.
54. Zhang, H., Ultrathin Two-Dimensional Nanomaterials. *Acs Nano* **2015**, *9* (10), 9451-9469.
55. Pan, J.; Lany, S.; Qi, Y., Computationally Driven Two-Dimensional Materials Design: What Is Next? *Acs Nano* **2017**, *11* (8), 7560-7564.
56. Qiu, L.; Li, D.; Cheng, H. M., Structural Control of Graphene-Based Materials for Unprecedented Performance. *Acs Nano* **2018**, *12* (6), 5085-5092.
57. Abdelmoaty, Y. H.; Tessema, T. D.; Norouzi, N.; El-Kadri, O. M.; Turner, J. B. M.; E-Kaderi, H. M., Effective Approach for Increasing the Heteroatom Doping Levels of Porous Carbons for Superior Co₂ Capture and Separation Performance. *ACS Appl. Mater. Interfaces* **2017**, *9* (41), 35802-35810.
58. Pykal, M.; Langer, M.; Prudilova, B. B.; Banas, P.; Otyepka, M., Ion Interactions across Graphene in Electrolyte Aqueous Solutions. *J. Phys. Chem. C* **2019**, *123* (15), 9799-9806.
59. Lu, Y.; Yang, F.; Wang, G. G. X.; Zhang, T. Y.; Wang, P., Recent Development of Graphene-Based Materials for Cathode Application in Lithium Batteries: A Review and Outlook. *Int. J. Electrochem* **2019**, *14* (7), 5961-5971.
60. Al Hassan, M. R.; Sen, A.; Zaman, T.; Mostari, M. S., Emergence of Graphene as a Promising Anode Material for Rechargeable Batteries: A Review. *Mater. Today Chem.* **2019**, *11*, 225-243.
61. Wang, W. R.; Su, H. J.; Wu, Y. X.; Zhou, T.; Li, T., Review-Biosensing and Biomedical Applications of Graphene: A Review of Current Progress and Future Prospect. *J. Electrochem. Soc.* **2019**, *166* (6), B505-B520.
62. Ojaghlou, N.; Tafreshi, H. V.; Bratko, D.; Luzar, A., Dynamical Insights into the Mechanism of a Droplet Detachment from a Fiber. *Soft Matter* **2018**, *14* (44), 8924.
63. Andrews, J. E.; Sinha, S.; Chung, P. W.; Das, S., Wetting Dynamics of a Water Nanodrop on Graphene. *Phys. Chem. Chem. Phys.* **2016**, *18* (34), 23482-23493.
64. Gim, S.; Lim, H. K.; Kim, H., Multiscale Simulation Method for Quantitative Prediction of Surface Wettability at the Atomistic Level. *J. Phys. Chem. Lett.* **2018**, *9* (7), 1750-1758.

65. Diao, Y. J.; Greenwood, G.; Wang, M. C.; Nam, S.; Espinosa-Marzal, R. M., Slippery and Sticky Graphene in Water. *Acs Nano* **2019**, *13* (2), 2072-2082.
66. Hong, G.; Han, Y.; Schutzius, T. M.; Wang, Y. M.; Pan, Y.; Hu, M.; Jie, J. S.; Sharma, C. S.; Muller, U.; Poulikakos, D., On the Mechanism of Hydrophilicity of Graphene. *Nano Lett.* **2016**, *16* (7), 4447-4453.
67. Feng, J.; Guo, Z. G., Wettability of Graphene: From Influencing Factors and Reversible Conversions to Potential Applications. *Nanoscale Horiz* **2019**, *4* (2), 339-364.
68. Melios, C.; Giusca, C. E.; Panchal, V.; Kazakova, O., Water on Graphene: Review of Recent Progress. *2d Mater.* **2018**, *5* (2), 22001.
69. Li, H.; Zeng, X. C., Wetting and Interfacial Properties of Water Nanodroplets in Contact with Graphene and Monolayer Boron-Nitride Sheets. *Acs Nano* **2012**, *6* (3), 2401-2409.
70. Mishra, A.; Hemeda, A.; Torabi, M.; Palko, J.; Goyal, S.; Li, D.; Ma, Y., A Simple Analytical Model of Complex Wall in Multibody Dissipative Particle Dynamics. *J. Comput. Phys.* **2019**, *396*, 416-426.
71. Hemeda, A. A.; Pal, S.; Mishra, A.; Torabi, M.; Ahmadelouydarab, M.; Li, Z.; Palko, J.; Ma, Y., Effect of Wetting and Dewetting Dynamics on Atomic Force Microscopy Measurements. *Langmuir* **2019**, *35* (41), 13301-13310.
72. Torabi, M.; Hemeda, A. A.; Palko, J. W.; Feng, Y.; Cao, Y.; Ma, Y. B., Modes and Break Periods of Electrowetting Liquid Bridge. *Phys. Rev. E* **2019**, *100* (3), 033102.
73. Rafiee, J.; Mi, X.; Gullapalli, H.; Thomas, A. V.; Yavari, F.; Shi, Y. F.; Ajayan, P. M.; Koratkar, N. A., Wetting Transparency of Graphene. *Nat. Mater* **2012**, *11* (3), 217-222.
74. Shih, C. J.; Wang, Q. H.; Lin, S. C.; Park, K. C.; Jin, Z.; Strano, M. S.; Blankschtein, D., Breakdown in the Wetting Transparency of Graphene. *Phys. Rev. Lett.* **2012**, *109* (17), 049901.
75. Kim, D.; Pugno, N. M.; Buehler, M. J.; Ryu, S., Solving the Controversy on the Wetting Transparency of Graphene. *Sci. Rep.* **2015**, *5*, 15526.
76. Ondarcuhu, T.; Thomas, V.; Nunez, M.; Dujardin, E.; Rahman, A.; Black, C. T.; Checco, A., Wettability of Partially Suspended Graphene. *Sci. Rep.* **2016**, *6*, 24237.
77. Vanzo, D.; Bratko, D.; Luzar, A., Tunable Wetting of Surfaces with Ionic Functionalities. *J. Phys. Chem. C* **2012**, *116* (29), 15467-15473.

78. Li, Z. T.; Wang, Y. J.; Kozbial, A.; Shenoy, G.; Zhou, F.; McGinley, R.; Ireland, P.; Morganstein, B.; Kunkel, A.; Surwade, S. P.; Li, L.; Liu, H. T., Effect of Airborne Contaminants on the Wettability of Supported Graphene and Graphite. *Nat. Mater* **2013**, *12* (10), 925-931.
79. Belyaeva, L. A.; van Deursen, P. M. G.; Barbetsea, K. I.; Schneider, G. F., Hydrophilicity of Graphene in Water through Transparency to Polar and Dispersive Interactions. *Adv. Mater.* **2018**, *30* (6), 1703274.
80. Ho, T. A.; Striolo, A., Polarizability Effects in Molecular Dynamics Simulations of the Graphene-Water Interface. *J. Chem. Phys.* **2013**, *138* (5).
81. Williams, C. D.; Dix, J.; Troisi, A.; Carbone, P., Effective Polarization in Pairwise Potentials at the Graphene-Electrolyte Interface. *J. Phys. Chem. Lett.* **2017**, *8* (3), 703-708.
82. Liu, J.; Lai, C. Y.; Zhang, Y. Y.; Chiesa, M.; Pantelides, S. T., Water Wettability of Graphene: Interplay between the Interfacial Water Structure and the Electronic Structure. *Rsc Advances* **2018**, *8* (30), 16918-16926.
83. Walther, J. H.; Werder, T.; Jaffe, R. L.; Gonnet, P.; Bergdorf, M.; Zimmerli, U.; Koumoutsakos, P., Water-Carbon Interactions Iii: The Influence of Surface and Fluid Impurities. *Phys. Chem. Chem. Phys.* **2004**, *6* (8), 1988-1995.
84. Du, F.; Huang, J. Y.; Duan, H. L.; Xiong, C. Y.; Wang, J. X., Wetting Transparency of Supported Graphene Is Regulated by Polarities of Liquids and Substrates. *Appl. Surf. Sci.* **2018**, *454*, 249-255.
85. Kong, W.; Li, H. S.; Qiao, K.; Kim, Y.; Lee, K.; Nie, Y. F.; Lee, D.; Osadchy, T.; Molnar, R. J.; Gaskill, D. K.; Myers-Ward, R. L.; Daniels, K. M.; Zhang, Y. W.; Sundram, S.; Yu, Y.; Bae, S. H.; Rajan, S.; Shao-Horn, Y.; Cho, K.; Ougazzaden, A.; Grossman, J. C.; Kim, J., Polarity Governs Atomic Interaction through Two-Dimensional Materials. *Nat. Mater* **2018**, *17* (11), 999-1004.
86. Schyman, P.; Jorgensen, W. L., Exploring Adsorption of Water and Ions on Carbon Surfaces Using a Polarizable Force Field. *J. Phys. Chem. Lett.* **2013**, *4* (3), 468-474.
87. Sharma, J. D.; Sharma, M.; Kumar, N.; Ahluwalia, P. K.; Iop, Computational Study of Dielectric Function and Optical Properties of a Graphene Nano Structure Containing Graphene Quantum Dot. *Dielectrics* **2013**, *472*, 012010.
88. Yang, J. Y.; Liu, L. H., Effects of Interlayer Screening and Temperature on Dielectric Functions of Graphene by First-Principles. *J. Appl. Phys.* **2016**, *120* (3), 034305.

89. Barrera, R. G.; Guzman, O.; Balaguer, B., Point-Charge in a 3-Dielectric Medium with Planar Interfaces. *Am. J. Phys.* **1978**, *46* (11), 1172-1179.
90. Bratko, D.; Jonsson, B.; Wennerstrom, H., Electrical Double-Layer Interactions with Image Charges. *Chem. Phys. Lett.* **1986**, *128* (5-6), 449-454.
91. Petersen, B.; Roa, R.; Dzubiella, J.; Kanduc, M., Ionic Structure around Polarizable Metal Nanoparticles in Aqueous Electrolytes. *Soft Matter* **2018**, *14* (20), 4053-4063.
92. Choudhuri, J. R.; Vanzo, D.; Madden, P. A.; Salanne, M.; Bratko, D.; Luzar, A., Dynamic Response in Nanoelectrowetting on a Dielectric. *Acs Nano* **2016**, *10* (9), 8536-8544.
93. Humphrey, W.; Dalke, A.; Schulten, K., Vmd: Visual Molecular Dynamics. *J. Mol. Graphics Model.* **1996**, *14* (1), 33-38.
94. Vanzo, D.; Bratko, D.; Luzar, A., Dynamic Control of Nanopore Wetting in Water and Saline Solutions under an Electric Field. *J. Phys. Chem. B* **2015**, *119*, 8890-8899.
95. Mark, P.; Nilsson, L., Structure and Dynamics of the Tip3p, Spc, and Spc/E Water Models at 298 K. *J. Phys. Chem. A* **2001**, *105* (43), 9954-9960.
96. Berendsen, H. J. C.; Grigera, J. R.; Straatsma, T. P., The Missing Term in Effective Pair Potentials. *J. Phys. Chem.* **1987**, *91* (24), 6269-6271.
97. Shafiei, M.; von Domaros, M.; Bratko, D.; Luzar, A., Anisotropic Structure and Dynamics of Water under Static Electric Fields. *J. Chem. Phys.* **2019**, *150* (7), 074505.
98. von Domaros, M.; Bratko, D.; Kirchner, B.; Hummer, G.; Luzar, A., Multifaceted Water Dynamics in Spherical Nanocages. *J. Phys. Chem. C* **2019**, *123* (10), 5989-5998.
99. Daub, C. D.; Cann, N. M.; Bratko, D.; Luzar, A., Electrokinetic Flow of an Aqueous Electrolyte in Amorphous Silica Nanotubes. *Phys. Chem. Chem. Phys.* **2018**, *20* (44), 27838-27848.
100. Vanzo, D.; Bratko, D.; Luzar, A., Wettability of Pristine and Alkyl-Functionalized Graphane. *J. Chem. Phys.* **2012**, *137* (3), 034707.
101. Shafiei, M.; Ojaghlo, N.; Zamfir, S. G.; Bratko, D.; Luzar, A., Modulation of Structure and Dynamics of Water under Alternating Electric Field and the Role of Hydrogen Bonding. *Mol. Phys.* **2019**, *117* (22), 3282-3296.
102. Sharma, S.; Debenedetti, P. G., Free Energy Barriers to Evaporation of Water in Hydrophobic Confinement. *J. Phys. Chem. B* **2012**, *116* (44), 13282-13289.

103. Giovambattista, N.; Debenedetti, P. G.; Rossky, P. J., Effect of Surface Polarity on Water Contact Angle and Interfacial Hydration Structure. *J. Phys. Chem. B* **2007**, *111* (32), 9581-9587.
104. Moucka, F.; Zamfir, S.; Bratko, D.; Luzar, A., Molecular Polarizability in Open Ensemble Simulations of Aqueous Nanoconfinements under Electric Field. *J. Chem. Phys.* **2019**, *150* (16), 124705.
105. Factorovich, M. H.; Molinero, V.; Scherlis, D. A., Hydrogen-Bond Heterogeneity Boosts Hydrophobicity of Solid Interfaces. *J. Am. Chem. Soc.* **2015**, *137* (33), 10618-10623.
106. Molinero, V.; Moore, E. B., Water Modeled as an Intermediate Element between Carbon and Silicon. *J. Phys. Chem. B* **2009**, *113* (13), 4008-4016.
107. Ardham, V. R.; Leroy, F., Thermodynamics of Atomistic and Coarse-Grained Models of Water on Nonpolar Surfaces. *J. Chem. Phys.* **2017**, *147* (7), 074702.
108. Stillinger, F. H.; Weber, T. A., Computer-Simulation of Local Order in Condensed Phases of Silicon. *Phys. Rev. B* **1985**, *31* (8), 5262-5271.
109. Lupi, L.; Kastelowitz, N.; Molinero, V., Vapor Deposition of Water on Graphitic Surfaces: Formation of Amorphous Ice, Bilayer Ice, Ice I, and Liquid Water. *J. Chem. Phys.* **2014**, *141* (18), 18C508.
110. Plimpton, S., Fast Parallel Algorithms for Short-Range Molecular-Dynamics. *J. Comput. Phys.* **1995**, *117* (1), 1-19.
111. Evans, D. J.; Holian, B. L., The Nose-Hoover Thermostat. *J. Chem. Phys.* **1985**, *83* (8), 4069-4074.
112. Moseler, M.; Landman, U., Formation, Stability, and Breakup of Nanojets. *Science* **2000**, *289* (5482), 1165-1169.
113. Gopan, N.; Sathian, S. P., Rayleigh Instability at Small Length Scales. *Phys. Rev. E* **2014**, *90* (3), 033001
114. Tiwari, A.; Abraham, J., Dissipative Particle Dynamics Simulations of Liquid Nanojet Breakup. *Microfluid. Nanofluid.* **2008**, *4* (3), 227-235.
115. Gopan, N.; Sathian, S. P., A Langevin Dynamics Study of Nanojets. *J. Mol. Liq.* **2014**, *200*, 246-258.
116. Tadmor, R.; Das, R.; Gulec, S.; Liu, J.; N'Guessan, H. E.; Shah, M.; Wasnik, P. S.; Yadav, S. B., Solid-Liquid Work of Adhesion. *Langmuir* **2017**, *33* (15), 3594-3600.
117. Lorenceau, E.; Clanet, C.; Quere, D., Capturing Drops with a Thin Fiber. *J. Colloid Interface Sci.* **2004**, *279* (1), 192-197.

118. Kang, W.; Landman, U., Universality Crossover of the Pinch-Off Shape Profiles of Collapsing Liquid Nanobridges in Vacuum and Gaseous Environments. *Phys. Rev. Lett.* **2007**, *98* (6), 064504.
119. Gauthier, E.; Hellstern, T.; Kevrekidis, I. G.; Benziger, J., Drop Detachment and Motion on Fuel Cell Electrode Materials. *ACS Appl. Mater. Interfaces* **2012**, *4* (2), 761-771.
120. Rahimian, P.; Battrell, L.; Anderson, R.; Zhu, N.; Johnson, E.; Zhang, L. F., Investigation of Time Dependent Water Droplet Dynamics on Porous Fuel Cell Material Via Synchrotron Based X-Ray Imaging Technique. *Exp. Therm Fluid Sci.* **2018**, *97*, 237-245.
121. Fu, S. C.; Leung, W. T.; Chao, C. Y. H., Detachment of Droplets in a Fully Developed Turbulent Channel Flow. *Aerosol Sci. Technol.* **2014**, *48* (9), 916-923.
122. Leung, W. T.; Fu, S. C.; To, G. N. S.; Chao, C. Y. H., Comparison of the Resuspension Behavior between Liquid and Solid Aerosols. *Aerosol Sci. Technol.* **2013**, *47* (11), 1239-1247.
123. Fu, S. C.; Cheung, Y. S.; Lee, H. H.; Kwan, J. K. C.; Chao, C. Y. H., Studies on Detachment Behavior of Micron Sized Droplets: A Comparison between Pure Fluid and Nanofluid. *Aerosol Sci. Technol.* **2018**, *52* (1), 69-77.
124. Yousefi, S. H.; Tang, C.; Tafreshi, H. V.; Pourdeyhimi, B., Empirical model to simulate morphology of electrospun polycaprolactone mats. *J. Appl. Polym. Sci.* **2019**, *136* (46), 48242.
125. Moghadam, A.; Jamali, M.; Venkateshan, D. G.; Tafreshi, H. V.; Pourdeyhimi, B., A new approach to modeling liquid intrusion in hydrophobic fibrous membranes with heterogeneous wettabilities. *Colloids Surf. A.* **2018**, *558*, 154-163.
126. Yousefi, S. H.; Tafreshi, H. V., Modeling electrospun fibrous structures with embedded spacer particles: Application to aerosol filtration. *Sep. Purif. Technol.* **2020**, *235*, 116184.
127. Gulec, S.; Yadav, S.; Das, R.; Tadmor, R., Reply to Comment on "Solid-Liquid Work of Adhesion". *Langmuir* **2017**, *33* (48), 13899-13901.
128. Geissler, P. L.; Dellago, C.; Chandler, D.; Hutter, J.; Parrinello, M., Autoionization in Liquid Water. *Science* **2001**, *291* (5511), 2121-2124.
129. Eaves, J. D.; Tomakoff, A., Electric Field Fluctuations Drive Vibrational Dephasing in Water. *J. Phys. Chem. A* **2005**, *109* (42), 9424-9436.
130. Bernholc, J.; Brenner, D.; Nardelli, M. B.; Meunier, V.; Roland, C., Mechanical and Electrical Properties of Nanotubes. *Annu. Rev. Mater. Res.* **2002**, *32*, 347-375.

131. Choudhury, N.; Pettitt, B. M., On the Mechanism of Hydrophobic Association of Nanoscopic Solutes. *J. Am. Chem. Soc.* **2005**, *127* (10), 3556-3567.
132. Zangi, R., Are Buckyballs Hydrophobic? *J. Phys. Chem. B* **2014**, *118* (42), 12263-12270.
133. Eun, C.; Berkowitz, M. L., Fluctuations in Number of Water Molecules Confined between Nanoparticles. *J. Phys. Chem. B* **2010**, *114* (42), 13410-13414.
134. Li, L. W.; Bedrov, D.; Smith, G. D., Water-Induced Interactions between Carbon Nanoparticles. *J. Phys. Chem. B* **2006**, *110* (21), 10509-10513.
135. Malde, A. K.; Zuo, L.; Breeze, M.; Stroet, M.; Poger, D.; Nair, P. C.; Oostenbrink, C.; Mark, A. E., An Automated Force Field Topology Builder (Atb) and Repository: Version 1.0. *J. Chem. Theory Comput.* **2011**, *7* (12), 4026-4037.
136. Stroet, M.; Caron, B.; Visscher, K. M.; Geerke, D. P.; Malde, A. K.; Mark, A. E., Automated Topology Builder Version 3.0: Prediction of Solvation Free Enthalpies in Water and Hexane. *J. Chem. Theory Comput.* **2018**, *14* (11), 5834-5845.
137. Yeh, I. C.; Berkowitz, M. L., Ewald Summation for Systems with Slab Geometry. *J. Chem. Phys.* **1999**, *111* (7), 3155-3162.
138. Daub, C. D.; Bratko, D.; Luzar, A., Electric Control of Wetting by Salty Nanodrops: Molecular Dynamics Simulations. *J. Phys. Chem. C* **2011**, *115* (45), 22393-22399.
139. Foulaadvand, M. E.; Ojaghloou, N., Structural and Elastic Properties of a Confined Two-Dimensional Colloidal Solid: A Molecular Dynamics Study. *Phys. Rev. E* **2012**, *86* (2), 021405.
140. Foulaadvand, M. E.; Shafiee, M. M., One-Dimensional Brownian Motion in Hard Rods: The Adiabatic Piston Problem. *Epl* **2013**, *104* (3), 30002.
141. Arodz, T.; Saeedi, S., Quantum sparse support vector machines. **2019**, arXiv:1902.01879.
142. de Ruijter, M. J.; Blake, T. D.; De Coninck, J., Dynamic Wetting Studied by Molecular Modeling Simulations of Droplet Spreading. *Langmuir* **1999**, *15* (22), 7836-7847.
143. Taubin, G., Estimation of Planar Curves, Surfaces, and Nonplanar Space-Curves Defined by Implicit Equations with Applications to Edge and

- Range Image Segmentation. *IEEE Trans. Pattern Anal.* **1991**, *13* (11), 1115-1138.
144. Weijjs, J. H.; Marchand, A.; Andreotti, B.; Lohse, D.; Snoeijer, J. H., Origin of Line Tension for a Lennard-Jones Nanodroplet. *Phys. Fluids* **2011**, *23* (2), 022001.
145. Wang, S. R.; Zhang, Y.; Abidi, N.; Cabrales, L., Wettability and Surface Free Energy of Graphene Films. *Langmuir* **2009**, *25* (18), 11078-11081.
146. Zhou, H.; Ganesh, P.; Presser, V.; Wander, M. C. F.; Fenter, P.; Kent, P. R. C.; Jiang, D. E.; Chialvo, A. A.; McDonough, J.; Shuford, K. L.; Gogotsi, Y., Understanding Controls on Interfacial Wetting at Epitaxial Graphene: Experiment and Theory. *Phys. Rev. B* **2012**, *85* (3), 035406.
147. Werder, T.; Walther, J. H.; Jaffe, R. L.; Halicioglu, T.; Koumoutsakos, P., On the Water-Carbon Interaction for Use in Molecular Dynamics Simulations of Graphite and Carbon Nanotubes. *J. Phys. Chem. B* **2003**, *107* (6), 1345-1352.
148. Chakraborty, A. K.; Bratko, D.; Chandler, D., Diffusion of Ionic Penetrants in Charged Disordered Media. *J. Chem. Phys.* **1994**, *100* (2), 1528-1541.
149. Bratko, D.; Chakraborty, A. K., Ion-Ion Correlations in Quenched Disordered Media. *J. Chem. Phys.* **1996**, *104* (19), 7700-7712.
150. Bratko, D.; Striolo, A.; Wu, J. Z.; Blanch, H. W.; Prausnitz, J. M., Orientation-Averaged Pair Potentials between Dipolar Proteins or Colloids. *J. Phys. Chem. B* **2002**, *106* (10), 2714-2720.
151. Ballenegger, V.; Hansen, J. P., Dielectric Permittivity Profiles of Confined Polar Fluids. *J. Chem. Phys.* **2005**, *122* (11), 114711.

Appendices

Appendix 1.

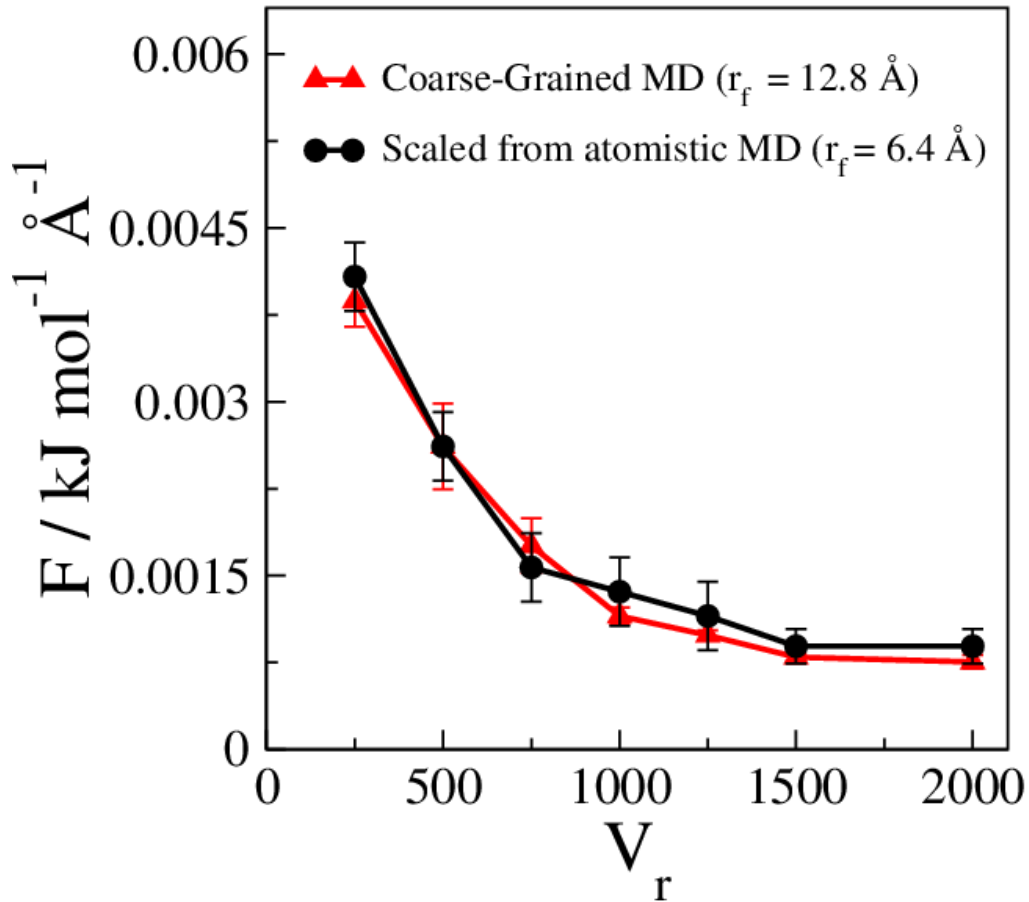


Figure S 1: The minimum force required to detach the droplet from a fiber at different reduced volumes. The red curve describes simulation results of the Course-Grained model with the fiber radius 12.8\AA . The red curve was produced by scaling the result of atomistic model with fiber radius 6.4\AA

Appendix 2.

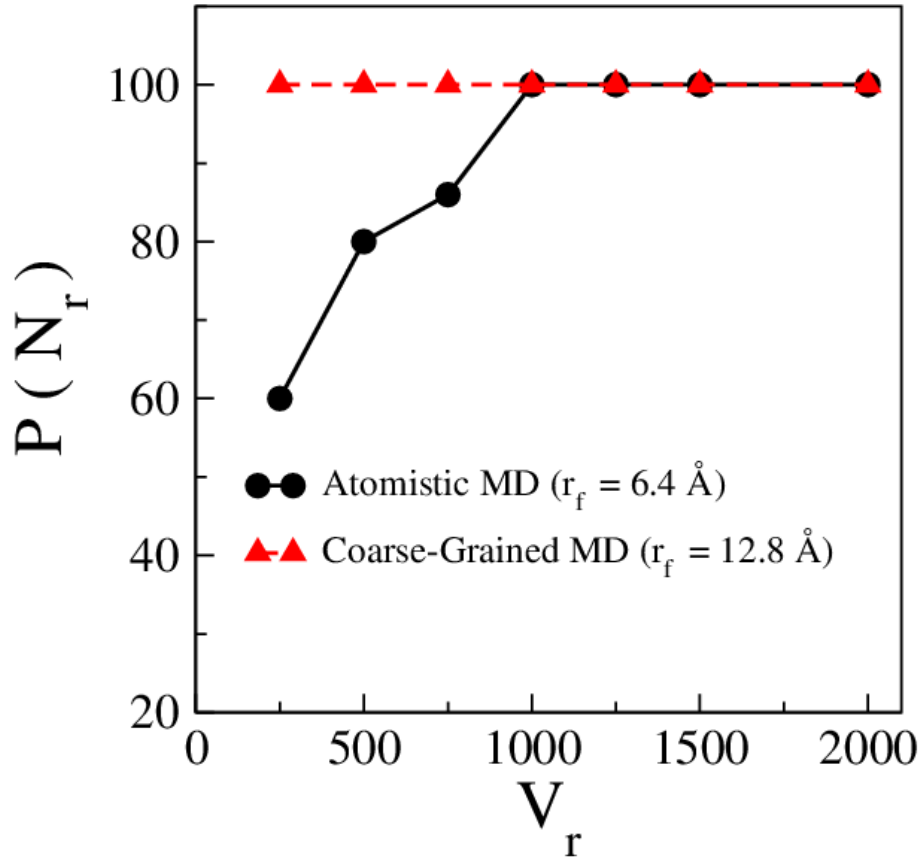


Figure S 2: The probability $P_{residue}$ of observing a residue on the fiber vs reduced volumes when applying the minimum detachment force for both atomistic and coarse-grained models.

Appendix 3.

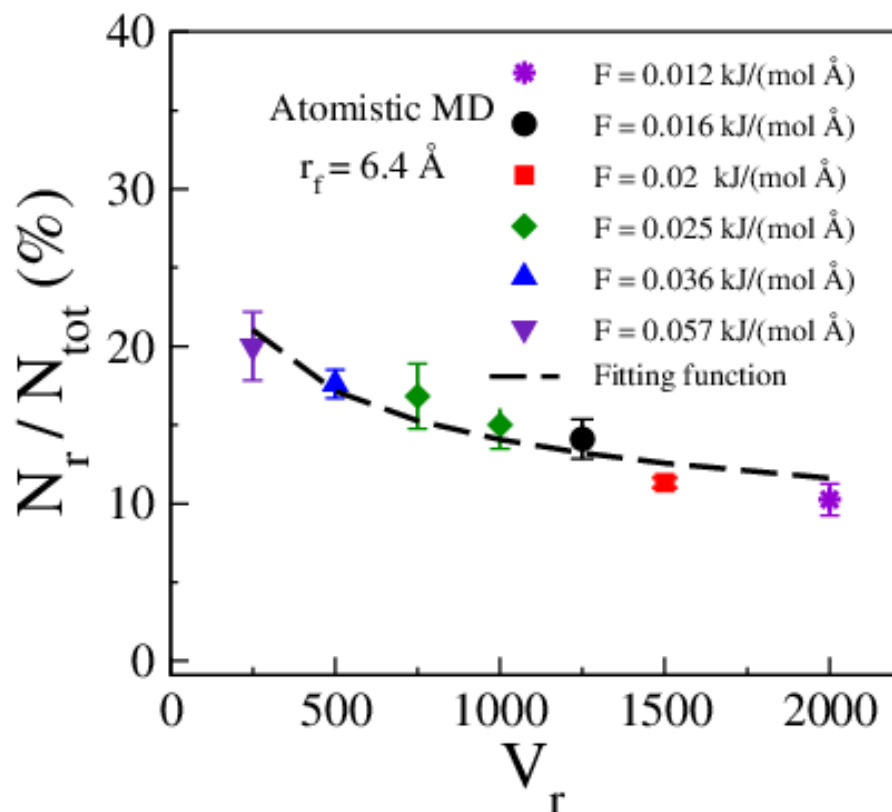


Figure S 3: The percentage of average number of water molecules remaining on the fiber versus the reduced volume for the detachment forces producing the maximal residue. The symbols denote the maximum residue on the fiber with radius 6.4 \AA at the time of detachment obtained from atomistic MD simulations.

Appendix 4.

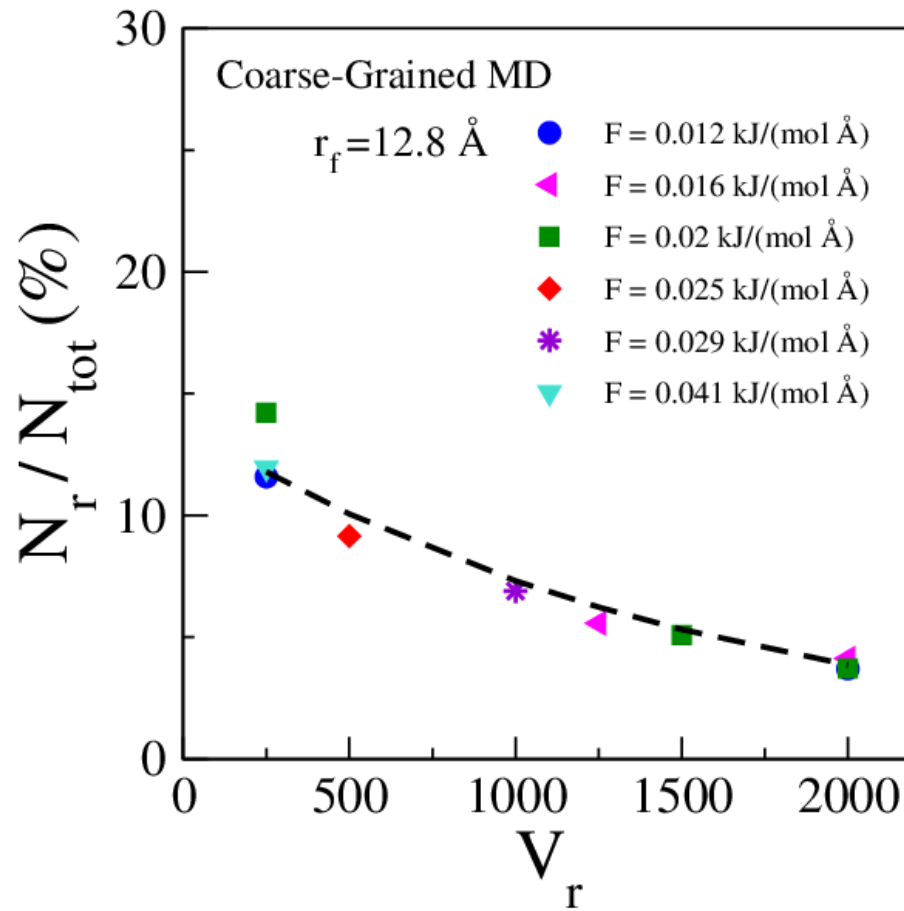


Figure S 4: The percentage of average number of water molecules remaining on the fiber versus the reduced volume for the detachment forces producing the maximal residue. The symbols denote the maximum residue on the fiber with radius 12.8 \AA at the time of detachment obtained from coarse-grained MD simulations.

Vita

Department of Chemistry, Virginia Commonwealth University (VCU)

Richmond, VA, 23220.

E-mail: ojaghloun@vcu.edu

Education

- **2015-2019: Ph.D.** Chemistry, Chemical Physics Program

Department of Chemistry, Virginia Commonwealth University, Richmond, VA, US.

Advisors: Alenka Luzar, Dusan Bratko

Thesis Title: Adhesion at solid/liquid interfaces

- **2009-2013: M.Sc.** Solid State Physics

Department of Physics, Zanjan University, Zanjan, Iran.

Advisor: Ebrahim Fouladvand

Thesis Title: Static and dynamic properties of repulsive soft particle in narrow channel by molecular dynamic simulation

Honors and Awards

- Finalist of VCU/PreX Demo Day for making stress app and winning 5000\$. 2019.
- Third place award in HealthHacks Medical Innovation Competition: Meeting Veteran's Need. We developed a smart system for predicting anxiety attacks using time predictive and machine learning algorithms, winning 500\$. VCU, 2018.
- Lidia M. Vallarino Scholarship for a distinguished Ph.D. candidate, Virginia Commonwealth University, 2018.

Publications

Peer-Reviewed

- Ojaghlou, N.; Bratko, D.; Salanne, M.; Shafiei, M; Luzar A. Solvent-Solvent Correlations Across Graphene: The effect of Image Charges, **ACSNANO 2019 (under review)**
- Shafiei, M; Ojaghlou, N.; Bratko, D.; Luzar A. Modulation of Structure and Dynamics of Water Under Alternating Electric Field and the Role of Hydrogen Bonding, *Molecular physics*, **2019**, 117 (22), 3282-3296.
- Ojaghlou, N.; Tafreshi, H. V.; Bratko, D.; Luzar, A. Dynamical insights into the mechanism of a droplet detachment from a fiber, *Soft Matter*, **2018**, 14 (44), 8924-8934 (**Selected for back cover**)
- Foulaadvand, M. E.; Ojaghlou, N. Structural and elastic properties of a confined two-dimensional colloidal solid: A molecular dynamics study, *Physical Review E*, **2012**, 86, 021405

In Preparation for Submission

- Ojaghlou, N.; Tafreshi, H. V.; Bratko, D.; Luzar A. droplet detachment from the hydrophilic surfaces, **2020**.

Refereeing (review of manuscript)

- Journal of Physics of Fluid
- Journal of Physical Review Letter
- Journal of Physical Review E
- Journal of Chemical Engineering Science

Proceeding (Non-Peer-Reviewed) and Presentations

- Ojaghlou, N.; Bratko, D; Tafreshi, H.V, Luzar, Alenka, The effect of detaching force on water retention on a surface, (**Contributed talk**), APS Division of fluid Dynamics (DFD), (November- 2019)
- Ojaghlou, N.; Bratko, D; Shafiei, M, Luzar, Wetting translucency of conducting graphene in polar and nonpolar liquids, (**Poster**), International symposium on clusters and nanomaterials (ISCAN), (November- 2019)

- Ojaghlou, N.; Bratko, D.; Tafreshi, H.V, Luzar, Alenka, Pathway of droplet removal from the hydrophilic surface, (**Poster**), International symposium on clusters and nanomaterials (ISCAN), (November- 2019)
- Ojaghlou, N.; Tafreshi, H. V.; Bratko, D.; Luzar, A. Water adhesion on hydrophilic fiber, 7th Virginia Soft Matter Workshop (**Contributed talk**), University of Virginia, VA, US (Sept 2019)
- Ojaghlou, N.; Bratko, D; Tafreshi, H.V, Luzar, Alenka, The effect of detaching force on water retention on a surface, Gordon Research seminars on Chemistry and physics of liquid (**Poster**), Holderness School, NH, US (August-2019)
- Ojaghlou, N.; Bratko, D.; Salanne, M; Shafiei, M; Luzar, Solvent-solvent correlation across graphene-the effect of image charges, Gordon Research Conference on Chemistry and physics of liquid (**Poster**), Holderness School, NH, US (August-2019)
- Farhan, N M.; Aziz, H; Holweger, H.; Ojaghlou, N.; Tafreshi, H.V, On the Adhesion Force between a Droplet and a Single Fiber, (**Contributed talk**), American Filtration and Separation (AFS), 2019
- Ojaghlou, N.; Tafreshi, H. V.; Bratko, D.; Luzar, Dynamical insights into the mechanism of a droplet detachment from a fiber, (**Contributed talk**), Virtual Winter school on Computational Chemistry, 2019
- Ojaghlou, N.; Tafreshi, H. V.; Bratko, D.; Luzar, The effect of detaching force on the droplet residue on a fiber, American Physical Society (APS), (**Contributed talk**), Boston, US (2019)
- Ojaghlou, N.; Tafreshi, H. V.; Bratko, D.; Luzar, Physics behind the water droplet detachment from a fiber, Gordon Research seminars on water and aqueous solutions (**Poster**), Holderness School, NH, US (2018)
- Ojaghlou, N.; Tafreshi, H. V.; Bratko, D.; Luzar, Physics behind the water droplet detachment from a fiber, Gordon Research Conference on water and aqueous solutions (**Poster**), Holderness School, NH, US (2018)
- Ojaghlou, N.; Bratko, D.; Luzar, Wetting transparency of conducting graphene, Virginia Academy of science (**Contributed talk**), Longwood University, VA, US (May 2018)
- Ojaghlou, N.; Tafreshi, H. V.; Bratko, D.; Luzar, A. Droplet detachment from a fiber, 5th Virginia Soft Matter Workshop (**Contributed talk**), James Madison University, VA, US (Sept 2017)

- Foulaadvand, M. E.; Ojaghlu, N. Structural and elastic properties of a confined two-dimensional colloidal solid (**Poster**), School and Symposium Unifying Concepts in Material, ICTS, **India** (Dec 2012)
 - Foulaadvand, M. E.; Ojaghlu, N. Elastic properties soft particles in a 2D narrow channel (**Poster**), Proceeding of 17th Gava Zang Meeting on Condensed Matter Physics, Institute for Advanced Studies in Basic Sciences (IASBS), Zanjan, Iran, (2011)
 - Foulaadvand, M. E.; Ojaghlu, N. Elastic properties soft particles in a 2D narrow channel by strain fluctuation method: Molecular dynamic simulation (**Poster**), Proceeding of Iranian Physics Yearly Conference, Urma University, Urma, Iran, (2011)
-

Workshops (Summer schools and Certificates)

- Virtual winter school on computational chemistry, US (Feb 2019)
 - Classical Forcefields for Modeling Materials on Atomic Scales, US (Sep 2017)
 - Curve Fitting in Matlab, Virginia Commonwealth University, VA, US (Oct 2017)
 - 4th Virginia Soft Matter Workshop, Virginia Commonwealth University, VA, US (Oct 2016)
 - 3rd annual software-development summer school, Virginia Tech University, VA, US (June 2015)
 - School and Symposium Unifying Concepts in Material, ICTS, India (Dec 2012)
-

Outreach Activities

- Member of Women in chemistry at Virginia Section, Women in American Chemical society (ACS), VA, US (2018-Present)
- Member of American Chemical society (ACS), 2018
- Member of American physical society (APS), 2018
- Volunteer at Women Chemists committee career, VA, US (2018)
- Instructor at Chemist celebrate Earth week, VA, US (2018)
- Instructor at national chemistry week, VA, US (2017)
- Judge at Virginia Junior Academy of Science, VA, US (2017)